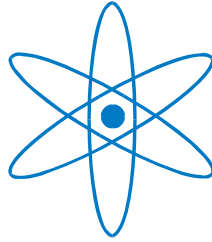# PHYSIK-DEPARTMENT

Advances in Coincident Doppler Broadening
Spectroscopy: Element Selective Studies on Metallic
Nanolayers with Monoenergetic Positrons

Dissertation
von
Philip Pikart

TECHNISCHE UNIVERSITÄT
MÜNCHEN

TECHNISCHE UNIVERSITÄT MÜNCHEN

Physik Department E21

Advances in Coincident Doppler Broadening Spectroscopy: Element Selective Studies on Metallic Nanolayers with Monoenergetic Positrons

Philip Pikart

Vollständiger Abdruck der von der Fakultät für Physik der Technischen Universität München zur Erlangung des akademischen Grades eines

Doktors der Naturwissenschaften (Dr. rer. nat.)

genehmigten Dissertation.

Vorsitzender: Univ.-Prof. Dr. Harald Friedrich
Prüfer der Dissertation:

1. Priv. Doz. Dr. Christoph Pascal Hugenschmidt
2. Univ.-Prof. Dr. Peter Müller-Buschbaum

Die Dissertation wurde am 02.04.2012 bei der Technischen Universität München eingereicht und durch die Fakultät für Physik am 20.06.2012 angenommen.

Summary

Positron annihilation spectroscopy is an established technique for the analysis of lattice defects. The Coincident Doppler Broadening Spectroscopy (CDBS) of the positron annihilation radiation is frequently used to determine the chemical composition at vacancy-like defects. As a topic of current research, not only defects are studied by CDBS but also metallic precipitates which trap positrons. This positron trapping is caused by a potential well, which is formed due to the positron affinity difference between the bulk material and an embedded precipitate or layer.

Within the scope of this work, different metallic combinations were studied systematically through the use of layered metallic samples. Layered samples have several advantages compared to heterogeneous mixtures: Firstly, the size of the metallic layers and therefore the size of a positron trapping structure can be controlled by precise sample preparation. Secondly, the implantation of the positrons can be targeted above, within or below the layer by the use of a monoenergetic positron beam. Thirdly, the metals combined in the layered system can be chosen according to their specific positron affinities.

Hence a systematic scheme to determine the CDBS sensitivity to embedded metallic layers with different thicknesses and material combinations was pursued. It was shown that an extremely high sensitivity for layers with attractive positron affinity can be reached. A layer with a nominal thickness of only $2\,\mathrm{nm}$ of gold embedded under $200\,\mathrm{nm}$ of pure aluminium could be detected with high significance. The quantitative analysis shows that $83\,\%$ of the positrons are trapped in this intermediate layer. This high fraction is in astonishing contrast to the measurement of a layer of only $0.5\,\mathrm{nm}$ of gold, where no positron annihilation at gold clusters was detected. This experimental result confirms the quantum well model, which defines a minimal critical radius of a cluster to form a bound state of the trapped positron according to the positron affinity difference. The structure and size of embedded metallic clusters and layers was complementarily verified by transmission electron microscopy.

CDBS measurements of layered metallic systems proofed to be an efficient method to investigate the positron diffusion and trapping in binary systems. The gathered results provide new fundamental insights: Due to the high difference in sensitivity for agglomerations which are smaller or larger than the calculated critical radius, the growth or dissolution of such precipitates can be detected. Furthermore, the non-destructive CDBS allows in-situ measurements at elevated temperatures. Both features predestine CDBS for analyzing precipitate growth during heat treatment.

For this purpose, multiple enhancements of the CDB spectrometer have been undertaken during this work. A new sample heater was installed which reaches $800\,^\circ\mathrm{C}$. A new detector

setup and a novel data evaluation algorithm were developed and implemented, which reduce the measurement time for one CDBS acquisition from about six hours to only one hour. In addition, the extraction of electron binding energies from the CDB spectra could be demonstrated.

The enhanced spectrometer was also employed successfully for a variety of additional measurements which were in the scope of the author's studies. Moreover, the spectrometer served for experiments of external users, which were chosen by an international scientific committee for fulfillment at the NEPOMUC positron beam facility of the Forschungs-Neutronenquelle Heinz Maier-Leibnitz (FRM II).

Zusammenfassung

Die Positronenannihilations-Spektroskopie hat sich für die Analyse von Gitterdefekten etabliert. Ihre Variante "Coincident Doppler Broadening Spectroscopy (CDBS)" wird häufig angewendet, um an dem Spektrum der Annihilationsstrahlung die chemische Zusammensetzung von Fehlstellen zu erkennen. Zu den aktuellen Forschungsthemen gehört, CDBS nicht nur auf Fehlstellen anzuwenden, sondern auch metallische Ausscheidungen mit CDBS zu untersuchen, wenn sie in der Lage sind Positronen einzufangen. In diesem Fall wird das Positron in einem Potentialtopf lokalisiert, der sich aus dem Unterschied der Positronenaffinitäten zwischen dem Hauptmaterial und den eingelagerten Ausscheidungen oder gleichermaSSen zwischen dem Hauptmaterial und einer eingelagerten Schicht ergibt.

Im Rahmen dieser Arbeit wurden verschiedene Metallkombinationen als Dünnschichtsysteme untersucht. Dünnschichtsysteme haben mehrere Vorteile gegenüber heterogenen Mischsystemen: Die Größe der Metallschichten und damit die Größe der Struktur, die Positronen einfangen kann, kann präzise bei der Probenherstellung definiert werden. Weiterhin kann die Energie eines monoenergetischen Positronenstrahles so eingestellt werden, dass die Implantation der Positronen über, in oder unter der eingebetteten Schicht erfolgt. Letztens kann die gewünschte Kombination von Metallen in einem Dünnschichtsystem gemäß ihrer spezifischen Positronenaffinität erfolgen.

Die Sensitivität von CDBS auf eingebettete metallische Schichten wurde systematisch bestimmt, indem verschieden Metallkombinationen und Schichtdicken untersucht wurden. Für Schichten, die eine attraktive Positronenaffinität besitzen, konnte eine extrem hohe Empfindlichkeit beobachtet werden. Eine Schicht aus Gold mit einer nominalen Dicke von nur 2 nm, welche von 200 nm Aluminium bedeckt ist, wurde mit sehr hoher Signifikanz nachgewiesen. Die quantitative Analyse zeigt, dass 83 % der Positronen in der eingebetteten Schicht eingefangen worden sind. Es zeigt sich ein erstaunlicher Kontrast zu der Messung einer 0,5 nm dicken Goldschicht, bei der keinerlei Positronenannihilation an Goldatomen festgestellt werden konnte. Diese experimentellen Ergebnisse bestätigen das Quantentopfmodel, welches einen minimalen Radius für eine Agglomeration herleitet, die Positronen in einem gebundenem Zustand einfangen kann. Die Struktur und die Größe der eingebetteten metallischen Schicht und der metallischen Ausscheidungen wurden in komplementären Messungen mit Transmissionselektronenmikroskopie (TEM) bestätigt.

CDBS an metallischen Schichten hat sich als effiziente Methode herausgestellt, um die Positronendiffusion und den Positroneneinfang in binären Systemen experimentell zu untersuchen. Die erzielten Ergebnisse ermöglichen neue Grundlagenuntersuchungen, da sich Agglomerationen, die größer oder kleiner als der kritische Radius sind, in ihrem eingebetteten Zustand mit sehr hoher Sensitivität unterscheiden lassen. Dadurch, dass CDBS

eine zerstörungsfreie Methode ist, lässt sich das Wachstum oder das Auflösen von Agglomerationen in-situ beobachten. Somit ist CDBS prädestiniert für die Analyse von frühen Phasen des Ausscheidungswachstums.

Zu diesem Zweck wurden in dieser Arbeit auch vielfältige Erweiterungen an dem CDB Spektrometer durchgeführt. Es wurde ein neuer Probenhalter installiert, der bis zu 800 °C erreicht. Ein neuer Detektoraufbau und eine neuartige Datenanalyse wurden entwickelt und implementiert so dass die Messzeit für eine CDBS Messung von ungefähr sechs Stunden auf eine reduziert werden konnte. Weiterhin konnte der Einfluss von den Elektronenbindungsenergien auf das CDB Spektrum durch die neue Datenanalyse gezeigt werden.

Nicht zuletzt wurde das erweiterte Spektrometer vielfach für zusätzliche Messungen eingesetzt, die sowohl im Aufgabenbereich des Autors lagen, wie auch zu den Projekten von externen Usern gehörten. Diese Projekte sind von einem internationalen wissenschaftlichen Komitee zur Ausführung an dem NEPOMUC Strahl der Forschungs-Neutronenquelle Heinz Maier-Leibnitz (FRM II) ausgewählt worden.

Contents

1. Introduction

The investigation of the structure and lattice defects of materials is of high interest for solid state physics. For this reason, innumerous experimental techniques have been developed with wide spread analyzing abilities.

Microscopy techniques image the surface of a sample. The structure and the topography at the surface are accessible with methods like Atomic Force Microscopy (AFM), Scanning Tunneling Microscopy (STM) and Scanning Electron Microscopy (SEM) with even atomic resolution. In many cases, the chemical composition can be precisely analyzed by combination of these techniques with X-Ray Spectroscopy (XRS).

In some applications, it is necessary to directly analyze the volume of a sample. Sample preparation like Focused Ion Beam (FIB) cutting cannot generally expose inner layers of the specimen without possible alteration of the atomic structure. Furthermore, destructive sample preparation inhibits the in-situ observation of time or temperature dependent changes in the volume. In these cases it is obligatory to probe the material below its surface.

For the analysis of the three-dimensional structure, a wide range of diffractometers is extensively employed. With X-ray or neutron scattering it is possible to reconstruct the periodic structures of the sample volume. In combination with spectroscopy or neutron activation analysis, also smallest concentrations of chemical constituents are detectable.

But also non-periodic properties are of high interest: E.g. the formation or annealing of lattice defects is of great importance for metallurgy or semiconductor physics. Especially low concentrations of vacancies cannot be analyzed by diffraction due to their stochastic distribution. In addition, destructive sample preparation methods incorporate a high risk of inducing vacancies in the preparation process.

For defect characterization, positrons are well suited as nanoprobes. Positrons which are implanted into condensed matter thermalize rapidly, and then they diffuse over many lattice constants before they annihilate with electrons. During the diffusion process, the positron can get trapped in an open volume defect such as a vacancy. When the positron annihilates, it transmits several types of information in its annihilation radiation. If a significant fraction of the implanted positrons is trapped before annihilation, the radiation provides information about the trapping sites with a high emphasis compared to the undisturbed bulk material. The positron lifetime reflects the electron density at the annihilation site, which is related to the vacancy size and type. It was shown that monovacancy

concentrations down to 10^{-7} per atom could be detected [1].

The angular correlation of annihilation radiation [2] and its Doppler broadening [3] carry information about the electron momentum distribution at the annihilation site. By Coincident Doppler Broadening Spectroscopy (CDBS) the analysis of the chemical composition of the annihilation site becomes feasible [4–8]. By this spectroscopy technique, not only vacancies can be detected but also the amount of positrons which annihilates in metallic agglomerations can be identified.

Appropriate metallic agglomerations can also trap the positron and thereby they can be detected with the enormous sensitivity as vacancies [9]. The positron affinity difference to the host lattice and the size of the agglomeration strongly determine its trapping ability according to a three dimensional quantum well model. Thereby, not only very low concentrations of certain elements can be analyzed in the crystal lattice but it can also be measured, whether the elements form precipitates larger than the calculated minimal critical radius [10–13].

Positron annihilation spectroscopy has one more unique feature: The positron beam acts non-destructively. Hence the measurement does not affect time dependent processes in the sample. This predestines CDBS for in-situ measurements of agglomeration growth in the undisturbed volume of the sample. CDBS is expected to detect when the size of precipitates exceeds the radius which leads to effective positron trapping. For quantitative evaluation of the measurement results, it is important to experimentally validate the calculated critical sizes and the measurements sensitivity.

In the following chapter the general properties of positrons, its interaction with condensed matter and the Doppler broadening technique are briefly reviewed. Then the experimental setup is explained in detail together with the improvements in the spectrometer's performance, which will allow to study time dependent processes with CDBS. Afterwards, a set of Doppler broadening measurements is presented. The focus of this work is the investigation of agglomerations in layered metallic systems, while also first temperature dependent measurements are presented. In addition, a novel data evaluation algorithm is introduced. This new software primarily shortens the necessary measurement times and it features a view on electron binding energies in the Doppler broadening spectra. Beside the main studies on embedded metallic layers, as a case study phase transitions of an ionic liquid are studied with depth resolved and temperature dependent Doppler broadening spectroscopy. Finally the experiments are summarized and an outlook is given.

2. Positron physics

2.1. Discovery of the positron

The positron is a prime example of a particle which was first postulated due to theoretical calculations of P.A.M Dirac in the year 1930 [14] and shortly afterwards experimentally discovered by Anderson [15–17] in the year 1932. It was recognized as the antiparticle to the electron with the same mass [18] and spin, but opposite charge and magnetic moment [19]. Up to today the positron is subject of fundamental research of a possible asymmetry between particles and their antiparticles, but so far neither an asymmetry nor an instability concerning the positron [20] could be found.

Beside the fundamental research on antimatter itself, the interaction of positrons with matter got a topic of high interest for condensed matter physics [21]. The discovery of thermalized positrons [22] induced their application as nanoprobes which thermally diffuse through the crystal lattice before they annihilate into photons which can be analyzed by different kinds of spectroscopy.

This Positron Annihilation Spectroscopy (PAS) made an eminent progress, when applicable positron moderators were found [23–25] which enabled the realization of monoenergetic positron beams [26].

2.2. The positron as a nanoprobe

In this section the implantation of the positron, its thermalization and diffusion, and the types of positron sources are explained.

2.2.1. Implantation and thermalization

If a positron of several keV is implanted into a solid, it looses energy by interaction with the material. Before reaching thermal equilibrium, it penetrates the material up to an average depth $\bar{z}$ which is dependent of the initial energy E of the positron. This process is called implantation. With decreasing energy, it participates in several ionization processes, exciton formation and positron phonon interactions until it reaches the equilibrium. The whole process is called thermalization. The investigation of near-surface properties of
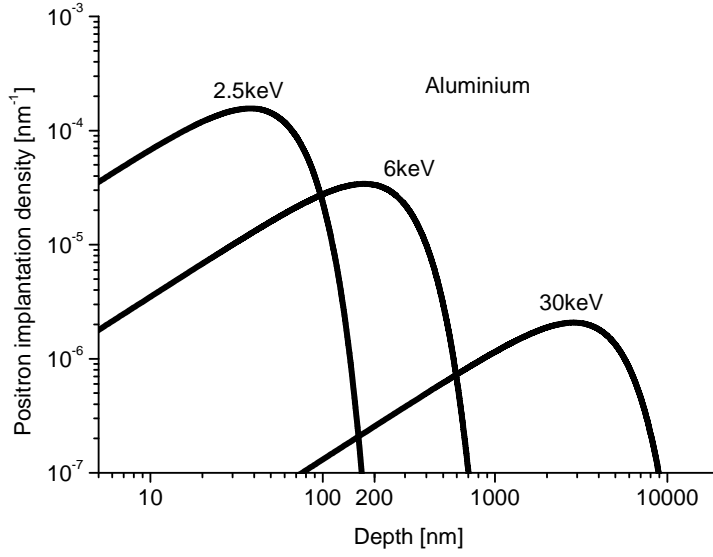
Figure 2.1.: Implantation profiles of positrons in pure Al approximated by Makhovian functions (material parameters from [28]).

samples requires a quantitative description of the implantation profile which is the depth-distribution of the positrons before diffusion.

This positron distribution is well approximated by a Makhovian function [27] with a mean implantation depth $\bar{z}$:

$$\bar{z} = AE^n \tag{2.1}$$

$\bar{z}$ follows a power law of the positron energy E. A, n, and m are material dependent parameters which are tabled in literature [28].

$$P(z) \approx e^{-\left(\frac{z}{z_0}\right)^m} \quad , \quad z_0 = \frac{\bar{z}}{\Gamma[\frac{1}{m} + 1]} \tag{2.2}$$

The derivation of the transmission probability function $P(z)$ equals the implantation profile $P'(z)$:

$$P'(z) = \frac{mz^{m-1}}{z_0^m} \cdot e^{-\left(\frac{z}{z_0}\right)^m} \tag{2.3}$$

Exemplary implantation profiles of different positron energies in aluminium are shown in figure 2.1 for typical energies of positron beams. The implantation curves show that the near surface volume within a depth range up to $10\,\mu$m can be studies depth resolved.

2.2.2. Diffusion and trapping

After full thermalization, the positron diffuses randomly as long as it is in a delocalized Bloch-state, i.e. in a defect free lattice. The average diffusion length L_+ depends on the lifetime τ_{e+} and the diffusion coefficient D_+ [1]. The positron lifetime in annealed aluminium amounts to $\tau_{e+} = 161 \pm 2\,\mathrm{ps}$ [29] and the diffusion length is $L_+ = 160 \pm 15\,\mathrm{nm}$ [30].

$$L_+ = \sqrt{D_+ \cdot \tau_{e+}} \tag{2.4}$$

If the thermalized positron reaches a vacancy or dislocation, it can be trapped or its diffusion can be confined due to an attractive potential caused by the missing positive charge of the atom core. This confinement can be of different dimensionality. Either i.e. a single vacancy can trap the positron into a localized state, or a linear or planar structure of attractive potential can confine the diffusion to one or respectively two dimensions. The trapping causes the extraordinary high sensitivity of positrons to defects. It could be shown that monovacancy concentrations down to 10^{-7} per atom could be detected [1].

Positron affinities

Not only vacancy-like defects form attractive potentials for positrons but also metallic clusters or layers as long as their positron affinity is higher than the surrounding material [9, 12, 13]. The reason for this effect is the potential step formed at the interface of two materials A and B. The according energy difference ΔE is defined by the chemical potentials of the positron and the electron $\mu^{\pm}$ in each material and the interface dipole $D_{AB} = \mu_A^- - \mu_B^-$: $\Delta E = \mu_A^+ - \mu_B^+ + D_{AB}$. This equation can be rewritten using the definition of the positron affinity $A^+ = \mu^+ - \mu^-$ and the relation $\Phi^{\pm} = -\mu^{\pm} \mp D_0$, where $\Phi^{\pm}$ are the work functions of the positron and of the electron, respectively. Since the dipole barriers at the surface D_0 and at the interface D_{AB} are respectively the same for electrons and for positrons but with opposite sign one obtains finally: $\Delta E = A_A^+ - A_B^+ \equiv \Delta A^+$ [27]. Since the more negative values for A^+ correspond to higher positron affinity, in this work $\Delta A^+ < 0$ denotes an attractive potential for positrons.

2.2.3. Moderation

If the positron is implanted near the surface of a defect free material, it can diffuse back to the surface. The potential at the surface is attractive to the positron, which can be either confined to a surface state or form positronium. In case of a negative positron work function, the thermalized positron can be re-emitted into the vacuum. Metals which are well suited for positron moderation have a negative positron work function of a few eV, which is much larger than the energy distribution of the thermalized positron. Hence the emission is approximately perpendicular to the surface with a sharp kinetic energy.

The efficiency of the moderation process depends on the energy of the incoming positrons. The maximal realizable efficiency ranges from below 1% [31] for β^+ sources to $\approx 10\%$ for remoderation devices [32, 33]. An energy filter built using conservative forces, i.e. a $E \times B$ filter, could only reach an efficiency $< 10^{-6}$ for cutting a $100\,\mathrm{meV}$ range out of a β^+ spectrum with an endpoint energy $> 100\,\mathrm{keV}$. The much higher efficiency of a moderator is achieved by non-conservative forces in the thermalization process, i.e. positron energy loss, which bypass Lioville's theorem.

2.2.4. Positron sources

Positrons are the most conveniently available type of antiparticle in the laboratory due to the availability of β^+ emitting radioactive sources which decay according to $^A_Z X \to {}^A_{Z-1}Y + e^+ + \nu_e$. The released energy of e.g. $546\,\mathrm{keV}$ for $^{22}\mathrm{Na}$ is continuously distributed between the electron neutrino and the positron. This process concurs with electron capture (EC) so that for positron generation a high branching ratio of β^+ decays is favorable.

A very common isotope for laboratory positron sources is $^{22}\mathrm{Na}$. It has a high branching ratio of 90% for β^+-decay and is commercially available. Its half life of $2.6\,\mathrm{years}$ is long enough for conveniant handling and short enough for a sufficient ratio of β^+-emission to the volume of the source. The size of the source limits the maximum intensity of β^+ emission which can be achieved due to self-absorption.

$^{22}\mathrm{Na}$-sources are often used if fast positrons of broad energy distribution are to be implanted in a specimen. The $^{22}\mathrm{Na}$ can be directly applied to the specimen, and positrons with the kinetic energy originating from the decay are implanted 0.1 to $1\,\mathrm{mm}$ in the volume of the specimen. For spectroscopy purposes, the available intensities of $^{22}\mathrm{Na}$-sources are widely sufficient in the case that the fast positrons can be directly applied to the sample.

For higher positron intensities than they are achievable with β^+-emitters, pair production $\gamma \to e^- + e^+$ is performed in a converter material of high nuclear charge. The intensity of a pair production source is only limited by the available intensity of high energetic γ radiation and the thermal management of the converter.

Slow positron beams

For the generation of a positron beam, a moderator is necessary to compress the continuous energy spectrum of the β-decay or pair production to a thermal distribution ($\approx 30\,\mathrm{meV}$) [26], which is considered as monoenergetic in comparison to the beam energy of up to $30\,\mathrm{keV}$. Subsequent to moderation, the positrons have to be extracted and guided to form a beam. The necessary instrumental technique is briefly explained in section 3.1.1 and in detail in [34] or [35].

2.3. Observables

2.3.1. Analysis of the annihilation radiation

For positron annihilation spectroscopy the annihilation radiation has to be analyzed for obtaining information about the annihilation site. For thermalized positrons the cross section for annihilation is given by [1]:

$$\sigma = \frac{\pi r_0^2 c}{v} \tag{2.5}$$

Therefore the annihilation probability is:

$$\Gamma = \sigma v n_e = \pi r_0^2 c n_e \tag{2.6}$$

$r_0 = \frac{e^2}{m_0 c^2}$ is the classical electron radius and v the positron velocity. As a consequence the positron lifetime $\tau = \frac{1}{\Gamma}$ is inversely proportional to the electron density n_e at the positron location and independent of the positron velocity. Due to this relation, positron lifetime spectroscopy directly reflects the electron density at the annihilation site. This allows to detect and distinguish monovacancies, vacancy clusters or even dislocations by the deconvolution of positron lifetime spectra [29].

Not only the electron density can be revealed by positron annihilation, also the electron momentum affects the emitted radiation. In the center of mass system of an annihilating electron positron pair, the 2γ decay is accomplished in exact 180° geometry with exactly the equal photon energy of $m_0 c$ as shown on the left side of figure 2.2. The right side of the same figure illustrates the lab system, in which deviations occur: The transversal momentum p_t of the electron positron pair causes a deviation of the emission angle, which can be gathered precisely by Angular Correlation of Annihilation Radiation (ACAR) measurements [36]. The longitudinal momentum component p_l induces a Doppler shift of the energy of the emitted photons, which is recorded in Doppler Broadening Spectroscopy (DBS).

ACAR and DBS measure the momentum distribution of the electrons at the annihilation site. The momentum of the thermalized positron can mostly be neglected.

The advantage of ACAR is that an angular correlation can be measured with principally arbitrary resolution using spatially resolved detectors, if the setup can be built large enough and therefore the angular resolution is enhanced. Hence it is preferably used for studies of the electrons with low momentum, i.e. in the conduction band of a metal. Due to the very small solid angle of the detectors, the detection efficiency of ACAR is relatively low. DBS can measure with a much bigger solid angle with high detector efficiency and is therefore better suited to detect the rare annihilation events, i.e. with core electrons [37].
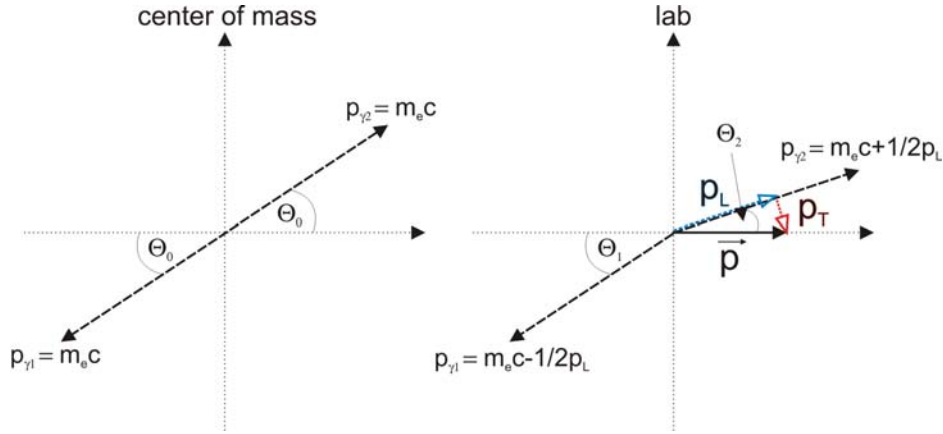
Figure 2.2.: Momentum conservation in the center of mass and in the lab system. Figure from [38].

2.3.2. Doppler broadening spectroscopy

In this section, the relation of the momentum of the annihilated electron with the Doppler shift of the emitted γ quanta is derived.

If a source is moving either toward (index 1) or away (index 2) from the observer while it emits electromagnetic waves with a frequency ν_0, the longitudinal Doppler effect shifts the frequency ν_1 and ν_2 of the received waves [39]. v_l is the longitudinal velocity component of the source.

$$\nu_1 = \nu_0 \cdot \sqrt{\frac{c + v_\mathrm{l}}{c - v_\mathrm{l}}} \quad \text{and} \quad \nu_2 = \nu_0 \cdot \sqrt{\frac{c - v_\mathrm{l}}{c + v_\mathrm{l}}} \tag{2.7}$$

For a transversal movement with the velocity v_t with respect to the emission direction, the Doppler effect accounts to:

$$\nu' = \nu_0 \cdot \sqrt{1 - \frac{v_\mathrm{t}^2}{c^2}} \tag{2.8}$$

Due to $c^2 \gg v_\mathrm{t}^2$ for velocities which affect DBS measurements, the transversal Doppler effect can be neglected and a first order Taylor series approximation is suitable to simplify the longitudinal case. For the same reason, non-relativistic calculation is justified:

$$\nu_{1,2} \approx \nu_0 \cdot (1 \pm \frac{v_\mathrm{l}}{c}) \tag{2.9}$$

For the 2γ decay of an electron positron pair, ν_0 represents the unshifted frequency of $511\,\mathrm{keV}$ photon energy. Consequently, the energy shift of the emitted photons depends on the sum emission energy E_sum and the longitudinal component of the momentum:

$$E_{1,2} = \frac{1}{2}E_{\text{sum}}(1 \pm \frac{p_{\text{l}}}{2m_0 c})$$ (2.10)

The energy E_{sum} equals the rest energy $2m_0 c^2 - E_b$ of the electron positron pair. E_b is the binding energy of the electron positron system, which can be significant for strong bound electrons in the inner shells, but can usually be neglected for evaluation of the Doppler shift.

Assuming $E_b \approx 0$, the energy of both emitted photons is with $E_{\text{kin,l}}$ as the longitudinal component of the kinetic electron energy:

$$E_{1,2} = 511\,\text{keV} \pm \frac{cp_{\text{l}}}{2} = 511\,\text{keV} \pm \sqrt{\frac{1}{2}m_0 c^2 \cdot E_{\text{kin,l}}}$$ (2.11)

For example, an electron moving with a kinetic energy of $10\,\text{eV}$ causes a Doppler shift of $1.6\,\text{keV}$, which can be precisely measured with a High Purity Germanium (HPGe) detector.
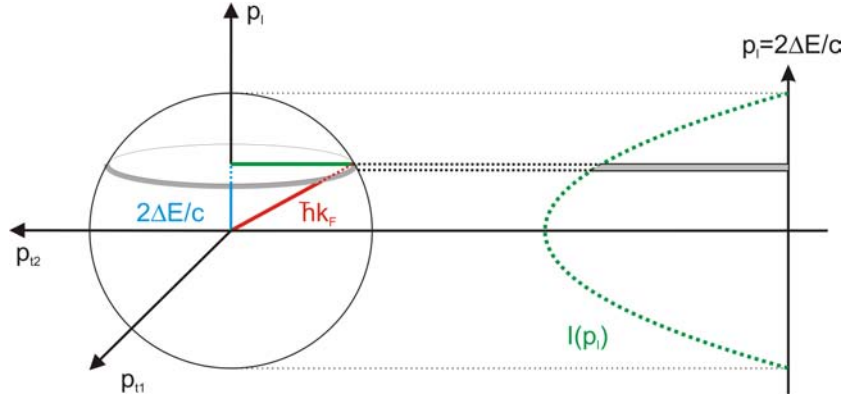

Figure 2.3.: Projection of the momentum distribution of a free electron gas onto the longitudinal component p_l. The resulting intensity distribution I as a function of p_l or ΔE is negatively parabolic. Figure from [38].

The energy of the Doppler shifted annihilation radiation represents the component of the electron momentum distribution which is longitudinal to the emission angle. In figure 2.3 an electron momentum distribution of conduction electrons with a Fermi energy E_{F} is projected onto one axis. As a result a symmetric, parabolic intensity distribution $I(p_{\text{l}})$ is obtained, which represents the Doppler broadened annihilation line.

S-Parameter

Due to the efficient trapping of positrons in vacancy like defects, DBS is frequently used to measure defect concentrations. The amount of Doppler broadening is significantly different, dependent on the annihilation location. As it is shown schematically in figure
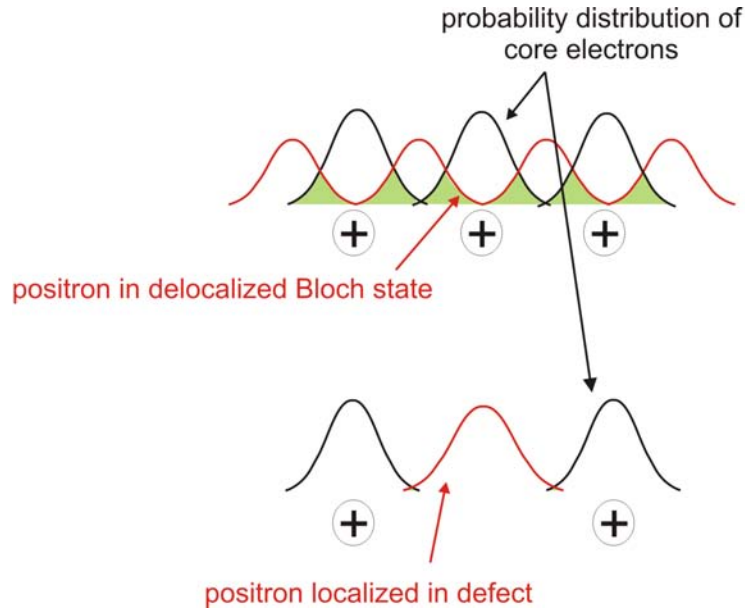
Figure 2.4.: Schematic sketch of a delocalized positron in a Bloch state and the probability distribution of localized core electrons. The overlap between both decreases, if the positron localizes in a defect. If many defects are present, the contribution of high momentum electrons decreases which enables relative measurements of defect densities. Figure from [38].

2.4, the probability distribution of the positron (red curve) overlaps more with the orbitals of core electrons, when the positron is in its localized Bloch state. If localized in a defect, the positron annihilates probably with valence electrons, which do not carry high momenta and therefor cause a lower Doppler shift.

For comparison of measured Doppler broadened annihilation spectra, the so called S-parameter is defined. It represents the ratio between a central region of the photopeak and the complete broadened peak area shown in Figure 2.5

$$S = \frac{A}{A + B} \tag{2.12}$$

Defect free samples will have higher Doppler-shifts and events from the center area (A) are more frequently shifted into the outside area (B). Hence the S-parameter is lowered. In contrary, a high S-value signals the presence of open volume defects.

The maximum accuracy of the S-parameter is obtained when the width of the central region is chosen that way, that the measured values fluctuate around 0.5. Then the propagated statistical error of $\frac{A}{A+B}$ is minimal.
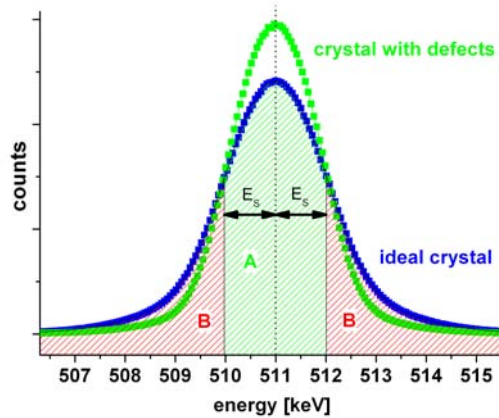
Figure 2.5.: Definition of the S-parameter as a measure for the width of the annihilation line. An arbitrarily chosen central region is divided by the total number of counts such that values roughly around 0.5 are achieved (for details see text). Figure from [38].

Coincident Doppler Broadening Spectroscopy (CDBS)

The probability density of the positron has a small overlap with strongly bound core electrons of the sample, which carry high momenta and whose momentum distribution is element-specific.

These accordingly rare events in the outer tail of the annihilation line can be recorded if the gamma background is reduced to a signal-to-noise ratio of better than 10^5 using two detectors in coincidence to detect the sum energy of $1022\,\text{keV}$ of both emitted photons (see chapter 3.3.1 for the general technique and chapter 3.3.5 for type of results). Consequently, CDBS reveals the contribution to the annihilation line of electrons from different elements by analyzing the photon intensity in the high-momentum region, i.e. at large Doppler shifts, of the recorded spectra and the chemical surrounding of the annihilation site becomes visible [4–8].

For example, CDBS was applied to investigate defects of ion-implanted semiconductors [40] or irradiation induced defects of Mg based alloys [41]. In addition, CDBS allows one not only to study the chemical surrounding of defect sites but also to identify agglomerations such as metallic precipitates in alloys, e.g. the formation of Cu precipitates in reactor pressure vessel steels [10, 11].

2.3.3. Positronium formation

In interaction with matter positrons can form positronium [43, 44]. Positronium is an exotic atom, which consists of an electron and a positron. Due to its composition of
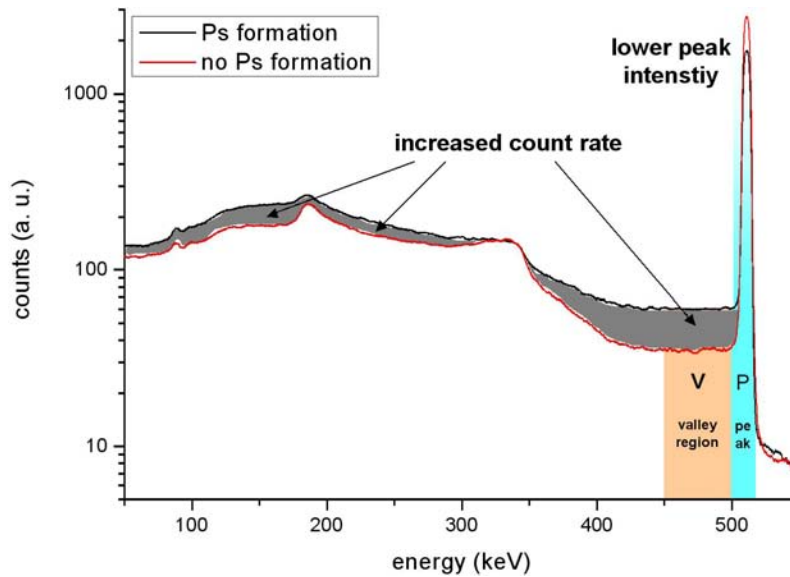
Figure 2.6.: The calculation of the $\frac{P}{V}$ ratio is an indicator for the formation of (ortho-)positronium. The 3γ decay of orthopositronium with a continuous spectrum from 0 to 511 keV generates a significantly higher count rate in the valley region of the annihilation spectrum. Both measurements are performed with germanium (see text). Figure from [42]

particles of exactly the same mass, it is subject of many fundamental studies of two- or three body systems [45]. Positronium appears in singlet state with antiparallel spins ($S = 0, M_S = 0$) which is known as para-positronium or in the triplet state with parallel spins ($S = 1, M_S = -1, 0, 1$) known as ortho-positronium. The singlet state decays quickly with a lifetime of 124.4 ps [46] and preferentially into two γ quanta of 511 keV[1]. Hence the annihilation of para-positronium is hard to distinguish from direct positron annihilation, for instance with conduction electrons of a metallic surface. The triplet state, which is known as ortho-positronium, has a much higher lifetime in vacuum of 142 ns [47] and preferentially decays into three γ-quanta with continuous spectrum. Due to its long life- time it can be analyzed in positron lifetime spectroscopy and due to its continuous decay spectrum, it can be recognized in the Doppler broadening spectra as well.

Orthopositronium decays faster when it interacts with matter and pick-up annihilation occurs [48]. For pick-up annihilation, the ortho-positronium exchanges the spin of the bound electron with electrons of the surrounding matter and quickly annihilates prefer- entially into two 511 keV photons like para-positronium. Hence, the decay rate of ortho- positronium is dependent of the interaction probability with surrounding matter.

---

[1]The decay into all even numbers of γ-quanta is possible for para-positronium due to spin conservation. Anyhow, already the branching ratio for four γ decay is $1.439 \cdot 10^{-6}$, so that the decays into higher numbers of γ-quanta are usually neglected.

Because positronium is frequently formed at surfaces [49], its presence and lifetime can indicate if the implanted positron diffuses to the sample surface or also to an embedded cavity.

Positronium formation is indicated in Doppler broadening spectra in two ways. Para-positronium decays into two γ with a low Doppler shift and hence it lowers the fraction of core electron contribution and increases the S-Parameter. Ortho-positronium can be detected with high sensitivity by calculation of the peak to valley ratio in the annihilation spectra. In figure 2.6 two complete and normalized annihilation spectra are visible. The 'no Ps formation' graph was measured in the bulk of room temperature germanium, where low positronium formation occurs. The black curve was measured at the surface of high temperature germanium, where positronium formation is maximized.

3. Coincident Doppler broadening spectroscopy at NEPOMUC

The principle of a CDBS spectrometer is to guide a sufficient number of positrons onto the sample and to measure the spectrum of the annihilation radiation.

In this chapter, the technical realization of this concept is explained. Monoenergetic positrons are produced and guided into the instrument where they are focused onto the sample surface as well as accelerated to the desired energy. The position of the positron focus on the sample as well as the sample temperature is controllable. The annihilation radiation is measured by a system of semiconductor detectors. The acquired measurement events are processed and stored digitally, and a new developed fitting algorithm determines the Doppler broadening spectrum.

3.1. The spectrometer

3.1.1. From positron generation to annihilation

Positron beam

For the required positron beam intensity, the CDBS spectrometer is set up at the NEutron induced POsitron source MUniCh (NEPOMUC), which itself is located at the high-flux research reactor FRM II. For the first stage of positron production, pair production $\gamma \rightarrow e^+ + e^-$ is used. In the case of the NEPOMUC source, γ-radiation (see figure 3.1) is created by placing ^{113}Cd inside a beam tube of the moderator vessel of the reactor. ^{113}Cd has a high cross section of 20600 barn for thermal neutron capture, so that effectively all neutrons are absorbed in the cadmium cap. The ^{113}Cd+n $\rightarrow$ ^{114}Cd+γ process generates a γ-cascade with in average 2.3 photons of an energy higher than 1.5 MeV, which is over the pair production threshold. Hence in the volume near the Cadmium a region of extremely intense and high-energetic gamma radiation is created.

A platinum structure is placed inside this region, so that the high atomic charge Z of platinum induces a high production rate of electron positron pairs. Furthermore, platinum is one of the few elements [50] which are suitable for positron moderation because of their sufficiently negative positron work function. It allows an directed emission of the moderated positrons into the vacuum. Hence, the pair production and the first stage of

moderation are performed in the same material. After emission from the platinum surface with $E_{\mathrm{kin}} = 1.95\,\mathrm{eV}$ [51] the positrons are accelerated electrostatically and coupled into the magnetic guidance field of the beam line. The beamline is led non-straight through several meters of biological shield around the reactor to shield the γ-radiation. An intensity of up to $9 \cdot 10^8\,\frac{e^+}{\mathrm{s}}$ [52] is reached at the output of the beamline.

Due to the overlap of electric and magnetic fields in the in-pile source, the width of the energy spectrum as well as the transversal momentum of the positron beam are far higher than the physical limits of the moderation process. This is undesired for accurate guidance and focusing of the beam. Hence a second moderation stage, from now on called remoderator, is set up behind the reactor shielding. A tungsten single crystal (tungsten has a negative work function for positrons of $-2.9\,\mathrm{eV}$ [50]) is placed in a magnetically shielded volume and the primary positron beam is focused onto the crystal. A fraction of the positrons implanted into the crystal is emitted after remoderation with an energy spectrum width and with a transversal momentum in the magnitude of thermal energies. Because the direction of the incoming beam is opposite to the outgoing positrons, this is a reflection-type remoderator. The remoderated positrons are guided into the beamline by electric and magnetic fields in a geometry which conserves their low phase-space volume. Hence the brightness of the remoderated beam is higher than of the primary beam [33].

Sample chamber

The sample chamber has to fulfill numerous requirements. Like the beamline it is a chamber for ultra high vacuum (UHV) to ensure that the positrons do not interact with residual gas before reaching the sample. The connection to the beamline needs a magnetic termination (Figure 3.2) at the entrance port, because no magnetic fields should interfere with electrostatic acceleration in the chamber. In the beamline, the positrons follow the magnetic flux lines as long as their gyration length is small compared to the gradient of the magnetic field. This type of beam guidance is called adiabatic [54]. The purpose of a magnetic field termination is to change the magnetic field so abruptly, that the positrons do not follow the magnetic flux lines at this point and are emitted into the magnetic field free space. To enhance this process, the magnetic termination is constructed of μ-metal and set to $-3\,\mathrm{kV}$ potential. This accelerates the positrons of the remoderated beam with $E_{kin} = 20\,\mathrm{eV}$ to $E_{kin} = 3.02\,\mathrm{keV}$ which increases the gyration length and therefore allows non-adiabatic extraction. The magnetic field at the termination was simulated with the FEM-program COMSOL. The result of the simulation shows, that the gyration length at $3\,\mathrm{keV}$ positron energy is about one order of magnitude higher than the length of the magnetic breakdown [38].

Below the magnetic field termination, there is a variable aperture. For best focus on the sample, it is necessary to cut the outer part of the positron beam. A turnable wheel
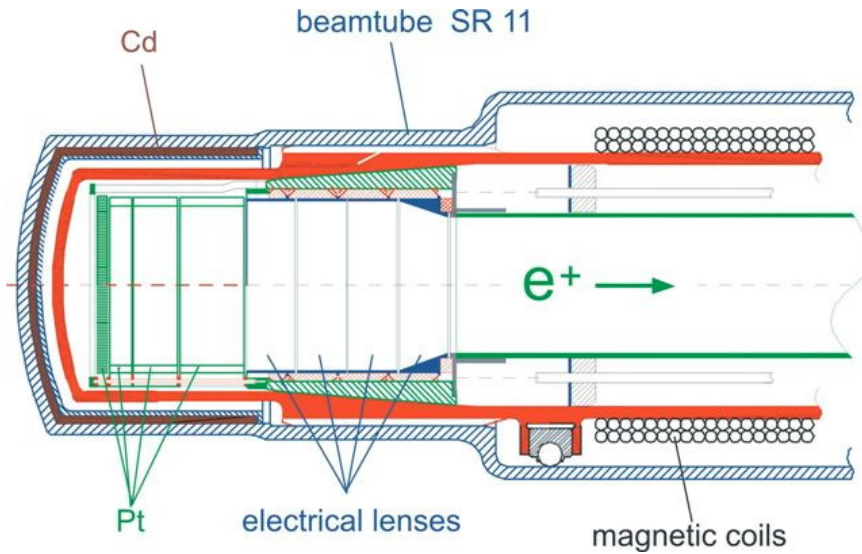
Figure 3.1.: Design of the high-intensity positron source NEPOMUC. The setup is inserted in the beam tube SR11 of the high-flux research reactor FRM II in Garching. Thermal neutrons from the reactor are captured in ^{113}Cd and the excited ^{114}Cd emits high energy γ-radiation. A platinum structure converts the γ-quanta into electrons and positrons. The positrons are moderated by the platinum itself and then electrically accelerated and magnetically guided to form a beam [53].

with boreholes from 0.1 to 30 mm which is set to the same potential as the magnetic field termination allows to choose between big apertures for higher positron intensity and small apertures for smaller positron focus.

Below the aperture, the electrical lens system starts. Lens 1 has to be set on the same potential as the aperture, to minimize the influence of different aperture setting to the beam optics. By the alternation of the potentials of lenses 2 to 4, the positron beam is focused. Every potential transition encloses focusing and defocusing areas. Due to the separation of the focusing and defocussing planes, the overall lens system is focusing.

The sample holder itself is connected to a negative high voltage power supply which defines the kinetic energy of the positrons on hitting the sample. Hence the positron energy can be adjusted between ≈ 0 and -30 keV.

On the bottom of the sample chamber there are the flanges for the sample positioning, the cryostat and the heater. Depending on the planned measurement, a positionable sample holder for a temperature range of $-200\,°\mathrm{C}$ to $300\,°\mathrm{C}$ or a non-positionable sample holder for a temperature range of $25\,°\mathrm{C}$ to $800\,°\mathrm{C}$ can be inserted. For scanning and for the measurement of different samples which are mounted on the sample holder at the same time, a stepping motor assembly is used. The sample is inserted through a port window
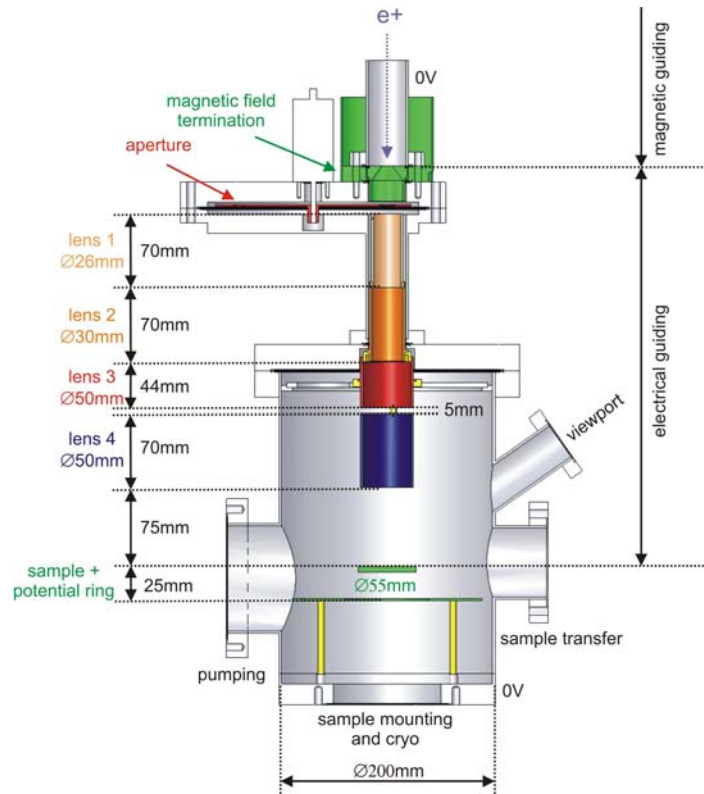
Figure 3.2.: Sketch of the sample chamber of the CDBS2. The magnetic field termination, the variable aperture, the lens system, the sample holder and the potential ring are shown together with all relevant measures. The fittings for pumping, the view port and sample transfer are located in one single plane in order to leave free space for the detectors which are located in a plane perpendicular to the drawing plane. Figure from [38]

below the view port, and the vacuum and the high voltage connection are provided through the flange opposite to the sample transfer window.

The spectrometer chamber including the beam guidance was developed and established by Martin Stadlbauer who gave a detailed description in his thesis [38]. During this work, a heatable sample holder and new a detector system was introduced.

Heatable sample holder

For many applications it is eligible to heat the sample in-situ during a (C)DB measurement. For this reason a mirror lamp assembly, consisting of a 150 W halogen lamp and an ellipsoid reflector is installed in the sample chamber (see figure 3.3) of the CDB spectrometer. To allow highest possible heating power, the lamp reflector and socket are cooled by water.

For a temperature range limited to 300 °C the standard positionable sample holder can be used. The sample holder is coated on its lower side with colloidal graphite for maximum light absorption. Thermal contact to the sample is ensured by usage of vacuum qualified silicone grease. The temperature of the sample holder is precisely measured by a fiber-optical thermometer, because electrical temperature sensors can not be used due to the high voltage of the sample holder ($\leq 30\,\text{kV}$). The fiber optical thermometer consists of an optical fiber, which is glued to a small gallium-arsenide (GaAs) chip. White light is reflected by the GaAs and its temperature is determined by the evaluation of the spectrum of the reflected light. The power of the heater lamp is regulated by a proportional-integral (PI) regulator. The temperature range of this setup is limited to 300 °C because of the limited thermal stability of the contact between the optical fiber and the GaAs chip.
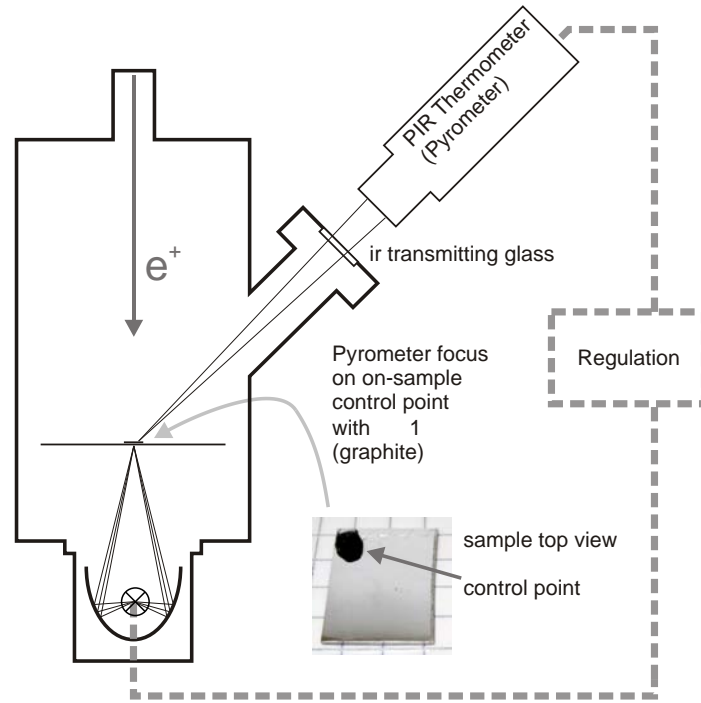

Figure 3.3.: The temperature of the sample is regulated by a passive infrared (PIR) thermometer and a halogen heater. The PIR thermometer is focused onto a control point with well-known emissivity ϵ which is directly applied to the sample.

For many materials, it is of interest to perform measurements at temperatures higher than 300 °C. Hence, a high temperature sample holder was constructed. It replaces the positioning unit, so that the light of the heater can be focused to a small, fixed and thermally isolated molybdenum sheet. At temperatures over 300 °C the use of silicone grease to ensure thermal contact is not recommended. For this reason the molybdenum

Positron energy	0.02 to 30 keV
Positron intensity on sample	up to $10^7 \frac{e^+}{s}$ maximum
Focal diameter on sample	0.3 to 4 mm
Positioning range	30 x 30 mm
Temperature range	$-200\,^{\circ}\mathrm{C}$ to $800\,^{\circ}\mathrm{C}$

Table 3.1.: The performance values reached by the CDBS spectrometer at NEPOMUC.

sheet has a hole in its middle, so that the mirror lamp directly shines at the backside of the sample. Because thermal contact to a temperature sensor is also difficult under these conditions, the sample's temperature is measured contact free by a passive infrared (PIR) thermometer. A two color pyrometer METIS MQ22 from Sensortherm™ is used together with a vacuum window which is transparent at the regarding wavelengths (see. Fig 3.3). To avoid measurement errors on shining metallic sample surfaces, the pyrometer is exactly focused on a temperature control point of colloidal graphite, which has to be applied to the sample before measurement. Control measurements with a thermocouple proof an accuracy of $\pm 2\,^{\circ}\mathrm{C}$ of this setup. As before, the power of the lamp is regulated by a PI control loop.

Sample chamber performance

In summary, the sample chamber setup reaches the performance values listed in table 3.1.

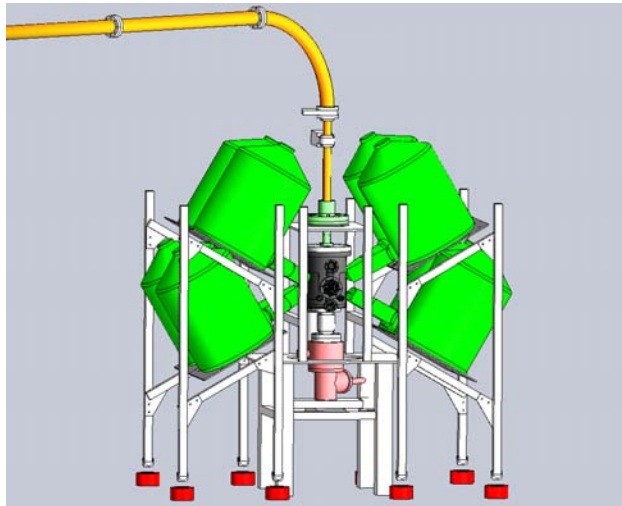### 3.1.2. Detector geometry

Figure 3.4.: The CDB spectrometer with eight detectors

The number of HPGe-Detectors has been increased from four to eight to furthermore reduce measurement times. In the previous setup, the detectors were placed X-shaped with variable distance to the chamber. In the new setup (Figure 3.4) the detectors are placed in a double-X-shape and have a fixed, minimal distance to the sample. The experiences with the variable distance setup showed that lowest possible distances between sample and detector are preferable.

3.1.3. Instrument control software

The unprecedented short measurement times of this CDB spectrometer make an automatic steering of the measurements parameters essential to allow a productive operation without continuous surveillance by the user. By usage of the positionable sample holder, up to nine different samples of 1cm^2 can be measured without user interaction. The sample- and lens-voltages as well as the samples temperature are automatically controlled together with the following auxiliary devices:

Nr.	Component
4	High voltage supplies for lenses
1	High voltage supply for sample potential
2	Stepper motors for sample positioning
1	Heater assembly
1	Pyrometer
1	MCA 3 Data aquisition system
2	Vacuum gauges

The steered instruments require a multi-threaded control software which simultaneously communicates with all connected devices. This could be reliably realized by a set of Labview™ virtual instruments (VI). Each connected device is controlled by its own VI, which itself is steered by a queuing message system. A graphical user interface enables easy definition of measurement lists and steady control of the instrument status (see Appendix B.1).

3.2. Detectors, electronics and data acquisition

3.2.1. High purity Germanium (HPGe) Detectors

To measure the Doppler broadening of the positron annihilation line, which is in the scope of several keV, radiation detectors with a sufficient energy resolution are needed. Furthermore, their efficiency should be high enough to reach an acceptable probability of coincident detection of a γ-quanta pair. γ-radiation detectors generally use a volume

which is ionized by γ-quanta in order to measure the energy deposited by the ionization process. Positron annihilation radiation can either deposit energy in matter by photo effect or by Compton scattering. For CDB spectroscopy the photo effect where the full γ-energy is deposited[1] is desired. The energy resolution of a γ-detector strongly depends on the average number of charge carriers, which are produced by a γ-quantum [55]. It gets better, the more ionizations are generated by a γ-quantum, which improve the statistical accuracy. The statistic distribution of the signal is also described by the so called Fano factor, which describes the variance of the number of generated charge carriers.

For these reasons, semiconductor detectors can be used for Doppler Broadening spectroscopy. For γ-energies in the $511\,\text{keV}$-range usually Germanium is used as semiconductor material due to its high Z and therefore its high efficiency, and due to its small band gap of $\approx 0.7\,\text{eV}$ which causes a high number of produced charge carriers. Together with its small Fano factor it enables a best possible energy resolution of $\approx 1.3\,\text{keV}$ at $511\,\text{keV}$ γ-energy [55, 56].

To realize a semiconductor radiation detector, a so called PIN-diode has to be established. Between the positive (P) and negative (N) doped areas of the semiconductor, an as big as possible intrinsic (I) volume has to be spawned, which allows the produced charge carriers to drift to the P and N contacts without prior recombination.

The intrinsic volume is generated by a reverse bias voltage on the semiconductor diode, which also drives the drift process. An intrinsic depletion zone is created in the semiconductor crystal, which thickness is proportional to $\sqrt{\frac{U}{n}}$ with U, the voltage of the reverse bias and n, the net impurity concentration of the crystal [55]. Hence, by a combination of high purity Germanium with a reverse bias voltage of up to $4.5\,\text{kV}$ a depletion zone of several centimeter thickness can be realized. Figure 3.5 shows a coaxial geometry of the intrinsic volume and the respective electronic output signals for three different interaction positions.

HPGe detectors have to be cooled to the temperature of liquid nitrogen during operation. At room temperature the number electron-hole pairs created by self-dissociation would lead to a devastating leakage current.

3.2.2. Signal chain

To reach an optimal acquisition performance, the current flowing through the detector crystal has to be amplified and shaped in several stages. Due to considerations, which are explained in detail in the electronics section (3.2.3), a signal chain like delineated in figure 3.6 was designed. The charge from the HPGe-crystal I_{Det} is collected in a capacitor

---

[1]The photo peak in the detector spectrum is composited of two effects: Either the γ-quantum is fully absorbed by the photo effect in one step, or it deposits a part of its energy by Compton scattering and the residual energy by subsequent photo-absorption. For CDB spectroscopy, both ways are equivalent and classified as photo effect.
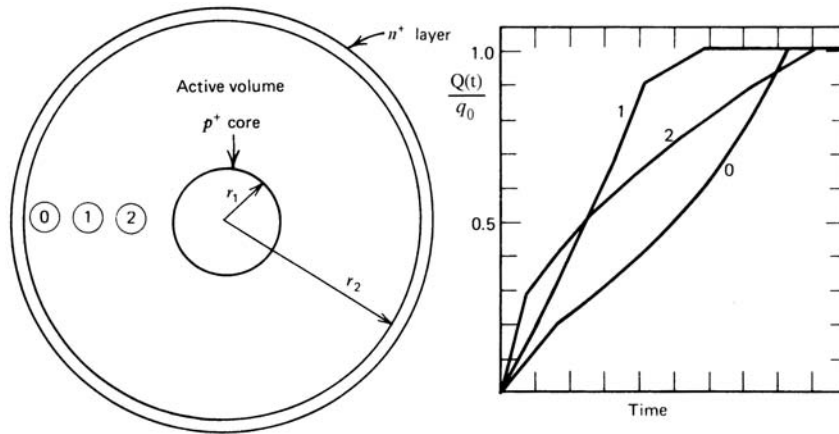
Figure 3.5.: Coaxial germanium detector: Three different interaction points are indicated as 0,1 and 2 (left). Leading edge of the output pulse(right). Figure from [55]

resulting in a voltage U_C. The voltage of this capacitor is amplified by the Transistor Reset Preamplifier (TRP) which is mounted at the detector capsule and delivered by Canberra with a specified amplification of $\frac{50\,\mathrm{mV}}{\mathrm{MeV}}$ and a fixed maximum voltage range of $4\,\mathrm{V}$.
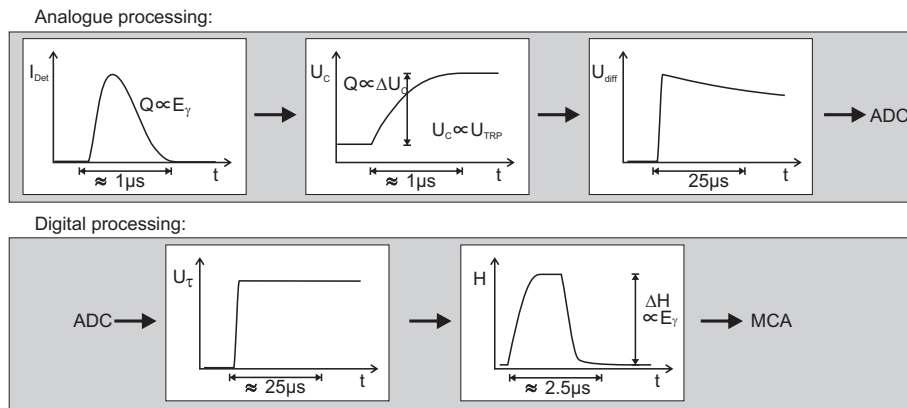

Figure 3.6.: The signal chain from the current I_{Det} through the detector crystal to the pulse height ΔH which is transmitted to the Multichannel Analyzer (MCA). The processing steps are explained in detail in the electronics section.

The other parts of the electronic as well as the Analogue-Digital-Converter (ADC) are built to own specifications. To determine the required performance values, artificial detector signals have been calculated and the whole signal chain was simulated.

For generation of the artificial detector signal the following components have been summed up:

- The current which flows through the detector crystal when it measures a $511\,\mathrm{keV}$

by photo effect. To investigate only the resolution of the connected signal chain, an infinite detector resolution has been assumed. The gradient of the detector current is varied stochastically to simulate different interaction points like outlined in figure 3.5. Also a stochastic timing of the 511 keV events has been assumed, so that different events might overlap.

- The background noise and leakage current according to measurements at the detector.

U_{TRP} is the output voltage of the TRP which is proportional to the charge in the capacitor which collects the current from the detector crystal. Then - still in the analogue signal chain - the edges of U_{TRP}, which represent the measured γ-events, are differentiated and amplified to U_{diff}. This signal is digitized and the pulse height is analyzed by τ-correction and trapezoidal shaping (see next section).

The result of the simulation are the following performance values:

Counting rate: $\leq 10^5$ $\frac{\text{counts}}{\text{s}}$

Energy resolution: < 430 eV at $10^5 \frac{\text{counts}}{\text{s}}$

Dead time: < 8 % at $10^5 \frac{\text{counts}}{\text{s}}$

The overall resolution R_{tot} of the γ-detection is the quadratic sum of the detectors resolution R_{Det} with the electronic resolution R_E.

$$R_{tot} = \sqrt{R_{Det}^2 + R_E^2} \approx \sqrt{(1.3\,\text{keV})^2 + (430\,\text{eV})^2} = 1.37\,\text{keV} \tag{3.1}$$

The simulated overall resolution is highly sufficient regarding the very high assumed counting rate of $10^5 \frac{\text{counts}}{\text{s}}$.

3.2.3. Electronics

To provide the maximum energy resolution even at high counting rates, the HPGe detectors used for the spectrometer are equipped with transistor reset preamplifiers (TRP). A TRP collects the whole charge which flows through the semiconductor crystal in a capacitor, and it is not discharged during operation. The voltage at the capacitor is amplified by a field effect transistor, which is also cooled together with the detector crystal. Hence the voltage level of the capacitor rises by a γ-energy dependent step for every time the active volume of the detector crystal is ionized. When the voltage level of the preamplifier exceeds an operational limit, the reset is performed. The reset transistor shortcuts the capacitor, so that the output voltage drops back to its initial value. During the reset the system is blind for γ-detection, but the reset occurs in less than 1μs.

A simulated output of the TRP with its whole voltage level range is plotted in figure 3.7 and a detail is shown in figure 3.8. The information of the single gamma events is contained in the small rising edges which are in the rising slope of the signal. Every time
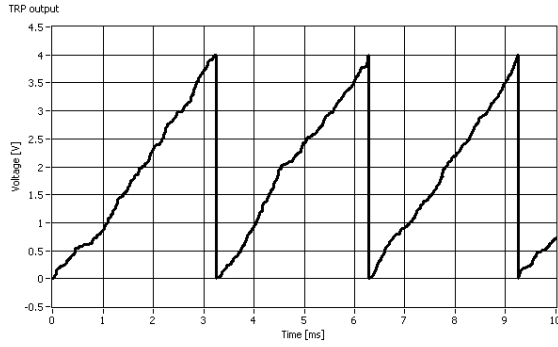
Figure 3.7.: A simulated output of a transistor reset preamplifier (TRP). γ-event information is contained in the small steps on the rising slope.
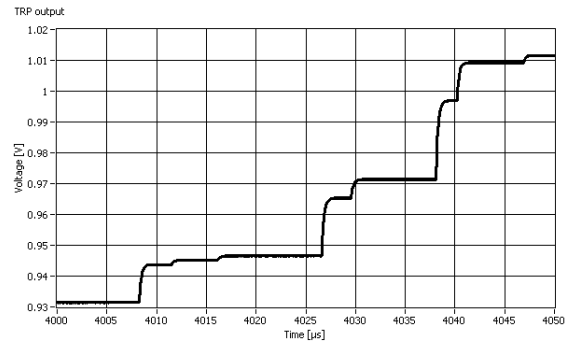
Figure 3.8.: Detail of the TRP output, making eight single γ-events visible.

the output limit of the preamplifier (4 V) is reached, the reset sets back the signal to 0V. Eight simulated γ-events are visible in figure 3.8 with stochastic timing. The height of each rising edge is proportional to the deposited energy of the regarding event.

Differentiating amplifiers

The most convenient way to process the output signal of the TRP would be to directly digitize it. The digitizer has to meet the following requirements:

- The rise time of an event's edge is about 200-300 ns, the time of complete charge collection is about $1\,\mu$s. Hence, a typical sampling rate of commercially available analogue to digital converters (ADC) of 100 MHz is widely sufficient.

- The voltage range of the TRP output is 4 V. Hence, a digitizer input with 5 V input range has to be chosen.

- The resolution of a HPGe Detector amounts to $E_{\mathrm{res}} = 1.3\,$keV. The whole voltage range of the TRP output equals an integrated γ-energy of 80 MeV, so that the digitizer has to accurately measure signals, which are $\approx \frac{1}{60000}$ of its voltage range. For this purpose, the accuracy of the digitizer should be at least one order of magnitude better than the resolution of the signal, which is reached with 20 bits of discretization levels.

Digitizers with 20 bits of effective resolution are available, but only for single channels and for inappropriate costs. Hence, the effective resolution of a standard 16 bit ADC

should be used to measure only the rising edges of the γ-events, and not the whole voltage range, which contains no additional information about the γ-spectrum.

This can be achieved by differentiation of the signal with subsequent amplification. The differentiation only passes the rising edges, hence they can be amplified so that the input range of the ADC is optimally utilized. A standard circuit with an operational amplifier (Figure 3.9) fulfills this task. The diode in the input circuit lowers the amplification of the reset edges, which are in opposite direction to γ-event edges.
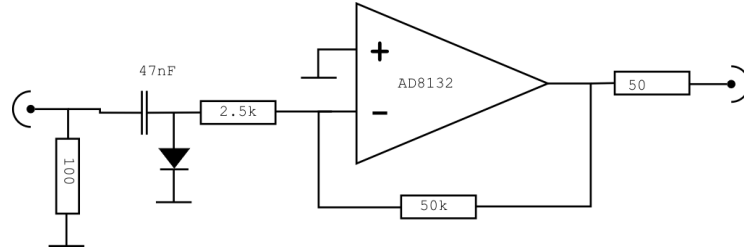

Figure 3.9.: The differentiating amplifier for rising edge amplification.

The operation of the differentiation amplifier is illustrated in figure 3.10. In the upper graph, three rising edges of the TRP output, resembling three events with different deposited energy, are plotted. The first event represents a 511 keV acquisition in the photo peak. The lower graph shows the output of the differentiating amplifier with the timing constants defined by the component values in figure 3.9. The amplitude of one 511 keV event is now in the range of 400 mV, which can be accurately measured with a 16-bit ADC. The falling slope of the tail of a γ-event is equalized after digitalization by τ-compensation (Figure 3.11).

Digital signal processing

A 16-bit, 100MHz ADC with 8 channels reads out the signals of the eight detectors. Afterwards, the τ-correction compensates the exponential falling of the differentiated signal and digital trapezoidal filters perform the pulse height analysis. As illustrated in figure 3.12, the trapezoidal shaping completely eliminates the influences of the rise time on the height analysis and it increases the measurements' accuracy by averaging over an adjustable time t_{peak}.

$U_{\text{diff}}(t)$ is the output voltage of the differentiating amplifier which is digitalized. $U_\tau(t)$ is the τ-compensated signal and $H(t)$ is the trapezoidal shaped signal. t_0 is the trigger time, which is approximately set to the position of the rising edge of an γ-event. τ is the time constant, which has to be channel wise adjusted to the timing of the differentiating amplifier.
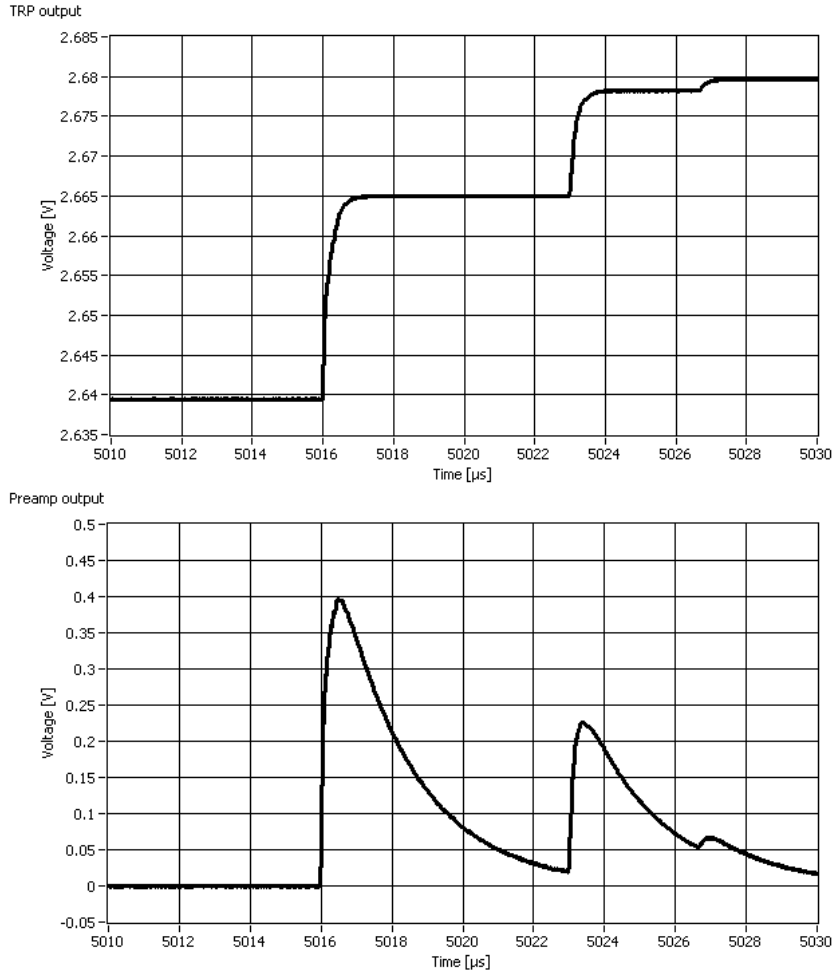
Figure 3.10.: The TRP signal (upper graph) and the output (lower graph) of the differentiating amplifier.

$$U_\tau(t) = U_{diff}(t) + \int_{a=t_0}^{t} U_{\text{diff}}(a)da \cdot \tau^{-1} \tag{3.2}$$

$$H(t) = \int_{a=t+t_{\text{peak}}+t_{\text{gap}}}^{t+2\cdot t_{\text{peak}}+t_{\text{gap}}} U_\tau(a)da - \int_{a=t}^{t+t_{\text{peak}}} U_\tau(a)da \tag{3.3}$$

t_{gap} and t_{peak} are defining the shape of the trapeze. They are optimized to enhance the resolution and minimize the noise of the detector system. The difference between the base and the top of the shaped trapeze (Figure 3.12) corresponds to the height of the rising edge in $U_\tau(t)$ and therefore to the height of the detectors signal.

After pulse height analysis, the events are checked for detector-pair-wise coincidence. If coincidence is confirmed within a timespan of $0.5\,\mu$s, the event is counted in one two-
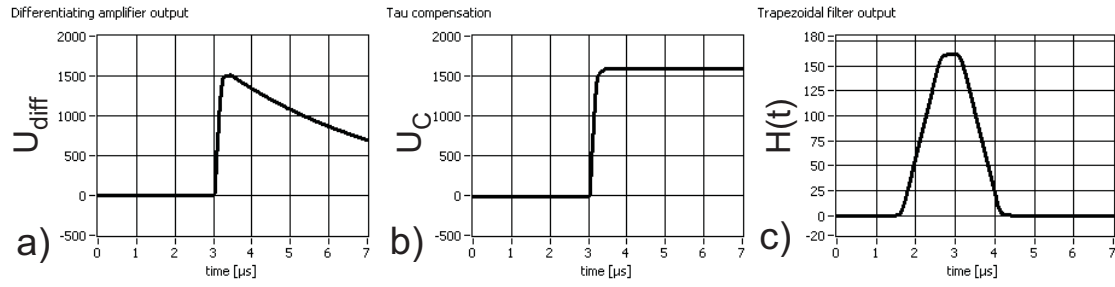
Figure 3.11.: The digital steps of signal processing. a) A single event from the differentiation amplifier. b) τ-compensation. c) trapezoidal shaping.

dimensional histogram per detector pair. The function of these histograms is explained in detail in the next section.

Acquisition system performance

The acquisition system was set up as simulated. So far, the simulated performance values could not be reached, supposedly due to non-linearities in the differentiating amplifier and due to noise issues. With reference γ sources, an energy resolution of only 1.8 keV at the 384 keV line of ^{133}Ba could be reached yet. This value is still to be improved by the installation of a improved version of the differentiating amplifier within a ongoing project.

Parallel to the development of the development of the new amplifiers, the CDB spectrometer at NEPOMUC is operated with a four-channel data acquisition system from Canberra and Fast Comtech™. The measurements presented in this work were performed with this setup. It reaches an overall energy resolution of 1.4 keV at a counting rate of $4 \cdot 10^4 \frac{\text{counts}}{\text{s}}$.
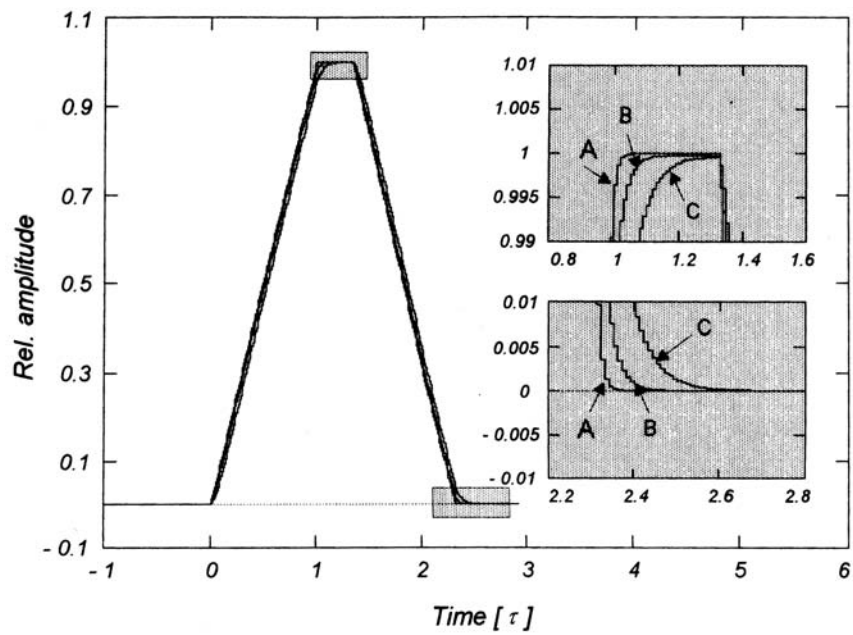
Figure 3.12.: Effect of trapezoidal shaping of detector pulses with three different rise times that increase in the sequence A, B, and C. In the case shown, if the trapezoidal flat top ($= t_{gap}$) is longer than the variation in rise time, the shaped pulses reach the same amplitude and ballistic deficit is avoided. Figure from [55]

3.3. Data evaluation

As described in section 2.3.2 the annihilation radiation of the electron positron pair carries the longitudinal projection of the electron momentum. The purpose of coincident acquisition is to gather the Doppler-broadened annihilation line precisely. In this section, first it will be defined what inevitable effects disturb the acquisition. Subsequently, a novel evaluation procedure is presented, which provides the spectrum with optimally suppressed disturbances and best possible statistics.

3.3.1. CDB spectra composition

The Doppler shifted energy of the positron annihilation radiation can be measured in both $\gamma-$photons of the dominant 2-γ decay. The original spectrum of the annihilation radiation is exemplary shown in figure 3.13. One ideal detector would be sufficient for the complete acquisition of the Doppler broadening, if there would be no disturbances. The detection of both annihilation quanta with two detectors gives redundant information for the Doppler Broadening, but additional information which is used for background suppression.
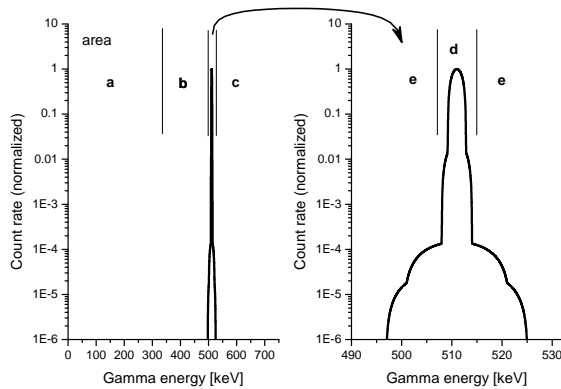

Figure 3.13.: The schematic[2] spectrum of the positron annihilation line. Area (e) contains the high momentum Doppler shifts, which are most interesting for CDBS evaluation.
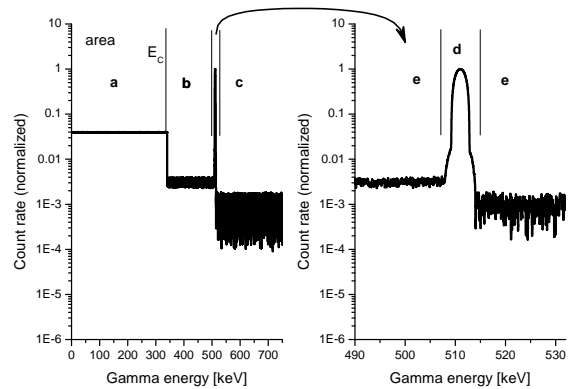
Figure 3.14.: Gamma ray detection is disturbed by several effects (see text). Area (e) of the Doppler broadened annihilation peak is hidden by the background. Compare to left figure

The best available detectors for the annihilation radiation are High purity Germanium (HPGe) detectors. By effects which are physically immanent to detector technology, the spectrum recorded with a HPGe detector is affected by several intrinsic distortions:

---

[2]The plots in figure 3.13 and figure 3.14 are schematic. Levels of high-momentum Doppler broadening, noise and Compton scattering are comparable to experimental results.

1. The detectors have an energy resolution of about $1.3\,\text{keV}$. This leads to a folding of the γ-spectrum with the approximately Gaussian resolution function.

2. γ-photon interaction with the detector occurs in two ways possible for 511keV-photons: Either by the photo effect, which deposits the total energy of the photon in the detector (Figure 3.14, area d & e), or by Compton scattering which leads to a continuous spectrum from $0\,\text{keV}$ to E_C (The highest energy, which is deposited by Compton scattering in the detector crystal, see Figure 3.14, area a): E_C is sufficiently far away from the Doppler broadened $511\,\text{keV}$ line so that Compton scattering does not directly influence Doppler broadening spectroscopy.

3. Compton scattering outside of the active detector volume: If γ-photons are scattered between the source and the detector, the detector measures a lower γ-energy (Figure 3.14, area b). Because the energy loss $\Delta E_\gamma = cos\Phi * E_C$ is low for a small scattering angle, it can not be distinguished if a photon slightly below 511keV is Doppler-shifted, or small-angle scattered. This generates a significant background in the left side of the annihilation line.

4. The 3-γ decay of ortho-positronium, which can always be formed when positrons reach surfaces, has also a continuous contribution to area b.

5. Incomplete charge collection in the detector crystal also contributes to area b.

6. Pile-up: The stochastic time distribution of the emitted positrons allows two decays to occur practically at the same time, so that the detector measures the sum of both deposited energies. Because Compton scattering is mostly involved in the pile-up, this causes an additional background over the whole energy region which is of importance for Doppler broadening spectroscopy (Figure 3.14, area a-c).

7. Positron reflection: Even if all positrons are ideally focused onto the sample, some of them get reflected and annihilate at some other part of the spectrometer. A single detector can not distinguish their radiation from annihilations in the sample

These effects decrease the SNR of single detector measurements to about 10^3. As it can be seen in figure 3.14 this does not allow to reveal the rare annihilations with core electrons, which carry the chemical information (see section 2.3.2).

In a setup with two detectors, each photon from a 2-γ annihilation event is measured with a separate HPGe-detector. The energy of both photons is correlated: $E_1 + E_2 \approx 1022\,\text{keV}$. But disturbances 2-6 all change the sum of measured energy significantly. The energy resolution increases by a theoretical factor of $\sqrt{2}$. The' disturbance 5 is greatly decreased because both γ-photons can only be detected if their source is in the line of both detectors.

The sum-energy condition can be achieved with an one dimensional multichannel analyzer, and a gate [57] which checks the right sum energy of both detector events. A more versatile approach is to record the detector events two-dimensionally. If both detectors measure an event during the coincidence timespan, it is counted in a coincidence matrix. One axis of the CDB-spectrum shows the energy measured by the first detector, the second axis shows the energy corresponding to the second detector. This is illustrated by figure 3.15 for an exemplary measurement.

In the 2-dimensional spectrum, different areas can be identified. Parallel to the detector energy axis, the events are located which result of the disturbance of a single detector, like small angle Compton scattering, incomplete charge collection or pile-ups. These events concentrate on lines parallel to the detector energy axis, because it is most probable that one event with low Doppler-shift is recorded by one detector without disturbance, while the energy measured by the other detector is shifted. In the lower left or upper right quadrant, there is a flat background consisting of the rare events, where both detectors have been disturbed simultaneously. In the 511 keV-center the non-Doppler-broadened and non-disturbed annihilation events are measured. On the diagonal line of constant sum energy $E_1 + E_2 = 1022$ keV only the low-level background and the Doppler-broadened annihilation events are located.
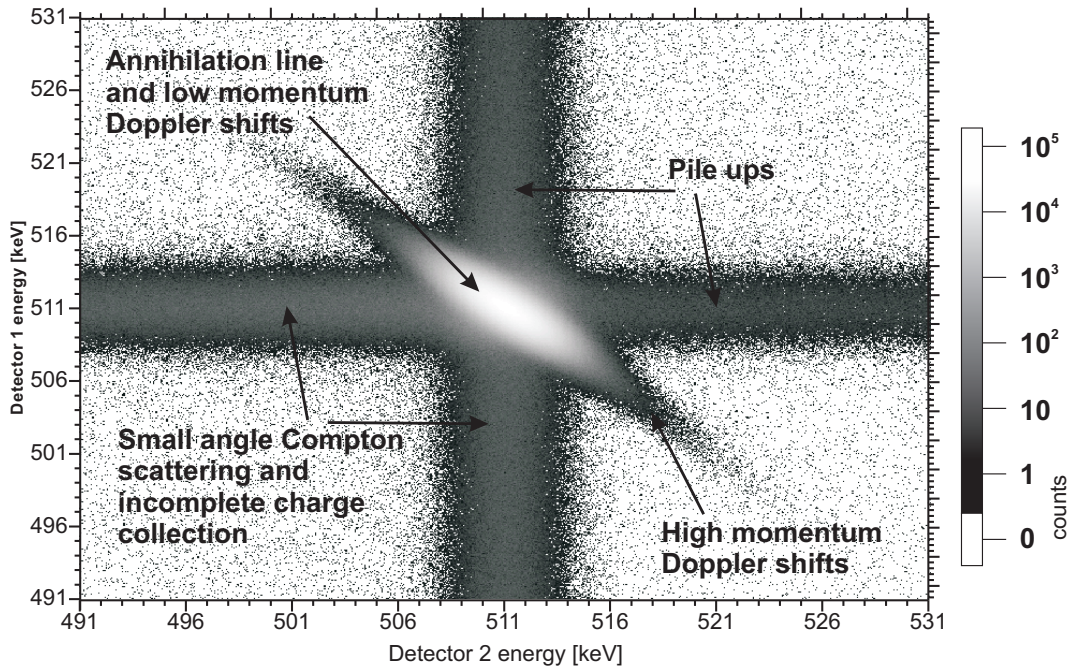

Figure 3.15.: In the 2-dimensional spectrum the energy of both coincident events is recorded. In the diagonal line with a sum energy of $E_{Sum} = 1022$ keV only the events are located which are not disturbed by effects 2-4 (see text.)

3.3.2. Conventional projection

The purpose of the data evaluation software is to extract the events of the diagonal Doppler-broadening area and project them onto a 1-dimensional axis of the Doppler-shift ΔE.

So far, at NEPOMUC, this was done by the MSPEC software from M. Haaks, which projects all events of a rectangular Region Of Interest (ROI) (see figure 3.16) onto the axis of energy difference. That way, all disturbances which lay outside this ROI are masked out, and the projection orthogonal to ΔE increases the energy resolution to $\approx \frac{1}{\sqrt{2}}$ of the resolution of a single detector. It uses a spline transformation to prevent aliasing when the discrete bins of the 2 dimensional source spectrum are projected to ΔE values of the target spectrum.
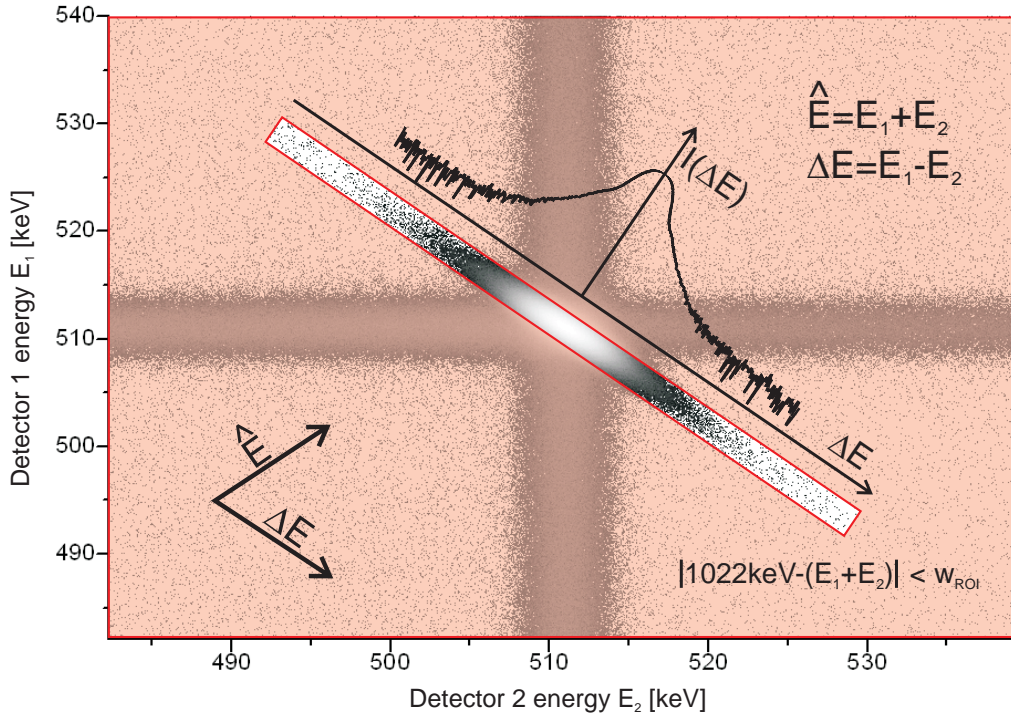

Figure 3.16.: Conventionally, a ROI (masked areas are red.) of the 2-dimensional spectrum is projected onto the axis of energy difference ΔE to gather the CDB spectrum $I(\Delta E)$.

By this projection technique, the background of the annihilation line can be successfully reduced by more than two orders of magnitude. Figure 3.17 clearly demonstrates that the high-momentum range up to $50 \cdot 10^{-3}\, m_0 c$ gets observable only in the spectra of coincident
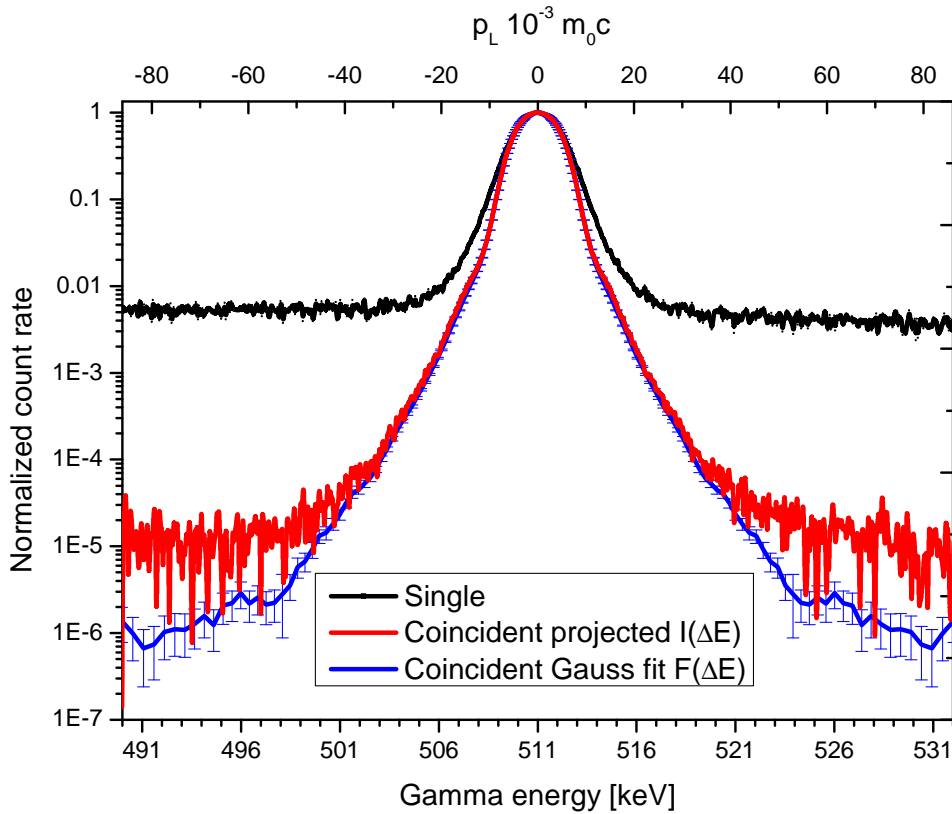
Figure 3.17.: The comparison of a single detector measurement (black) with coincident measurements (red and blue).

measurements. The red line in this diagram results of the conventional projection described in this section. In the next section it will be explained how the further improvement into the blue line was realized by more sophisticated evaluation of the 2-dimensional spectrum.

3.3.3. New evaluation

Principle

The previously described projection method is easy to realize, but has two disadvantages: Because of the technically limited detector resolution, a diagonal ROI like in figure 3.16 needs a sufficient width w_{ROI}. The wider this ROI gets, the more background of the 2D spectrum area is projected into the target spectrum. Furthermore, the wider the ROI gets, the more the disturbances from the small angle scattering and pile-up lines (see figure 3.15)

reach into the Doppler broadening spectrum.

For this reason, a new evaluation routine was developed, which inherently suppresses background and disturbances by fitting the instrument function to the complete 2-dimensional spectrum. Therefore, no ROI width has to be defined so that an optimal collection of all good events in the spectrum is ensured.

The new evaluation routine is also based on projections from the 2-dimensional spectrum to 1-dimensional functions. The orientation of the projection is rotated so that the data is no more projected onto the difference energy axis (ΔE) but onto the sum energy axis ($E_1 + E_2 = \hat{E}$). The result is from now on designated by $I_{dE}(\hat{E})$. dE denotes the ΔE range, where the projection is performed. Typical results for $I_{dE}(\hat{E})$ are shown in figure 3.19. For a Doppler broadened detector signal with a constant sum energy and without background or disturbances, these projections carry the shape $S_{sd}^2(\hat{E})$ if $S_{sd}(E)$ is the instrument function of a single detector at 511keV. $S_{sd}^2(\hat{E})$ can be well approximated by a Gaussian function[3].

Hence, the projection ROI has to be chosen so narrow that in the aspect of the detectors resolution, only events of a defined energy difference range in $[\Delta E_1, \Delta E_2] = w_{\mathrm{ROI}}$ are projected into $I_{dE}(\hat{E})$. Then a Gaussian function is fitted by a least square error optimization to $I_{dE}(\hat{E})$. The Gauss-fit delivers in the first place the area A_{dE}, which represents the number of counts for a defined Doppler broadening value ΔE. This procedure is repeated for the whole range of measurable Doppler shifts, so that as a result the function $A(\Delta E)$ is gathered, which contains the undisturbed Doppler broadening spectrum like the blue line in figure 3.17.

Projection technique

To get the best possible resolution and statistics, a projection $P : N(E_1, E_2) \rightarrow I(\hat{E})$ is used, which is defined by the following linear mapping:

$$I_{\Delta E}(\hat{E}) = \overbrace{\int \int}^{B} N(e_1, e_2) de_1 de_2 \tag{3.4}$$

$$B \equiv (\frac{\hat{E}}{2} - \Delta E - e_1)^2 + (\frac{\hat{E}}{2} + \Delta E - e_2)^2 \leq \frac{w_{\mathrm{ROI}}}{2}^2 \tag{3.5}$$

This mapping projects circular integrals over the 2D-matrix into the $I(\hat{E})$ function belonging to an energy shift ΔE. The projection of circular areas is optimal for the statistics, because the stochastic distribution of events in the 2D-spectrum, resulting from

---

[3]The instrument function of the averaged signal of two independent detectors measuring the same event is a multiplication of the instrument functions of both detectors. Because the detectors used for CDBS have the same instrument function $S_{sd}(E)$, their combined instrument function is $S_{sd}^2(E)$

the limited detector resolution, is in good approximation rotationally symmetric. In this step of processing only one interpolation is necessary to avoid aliasing effects (see Appendix A.2).
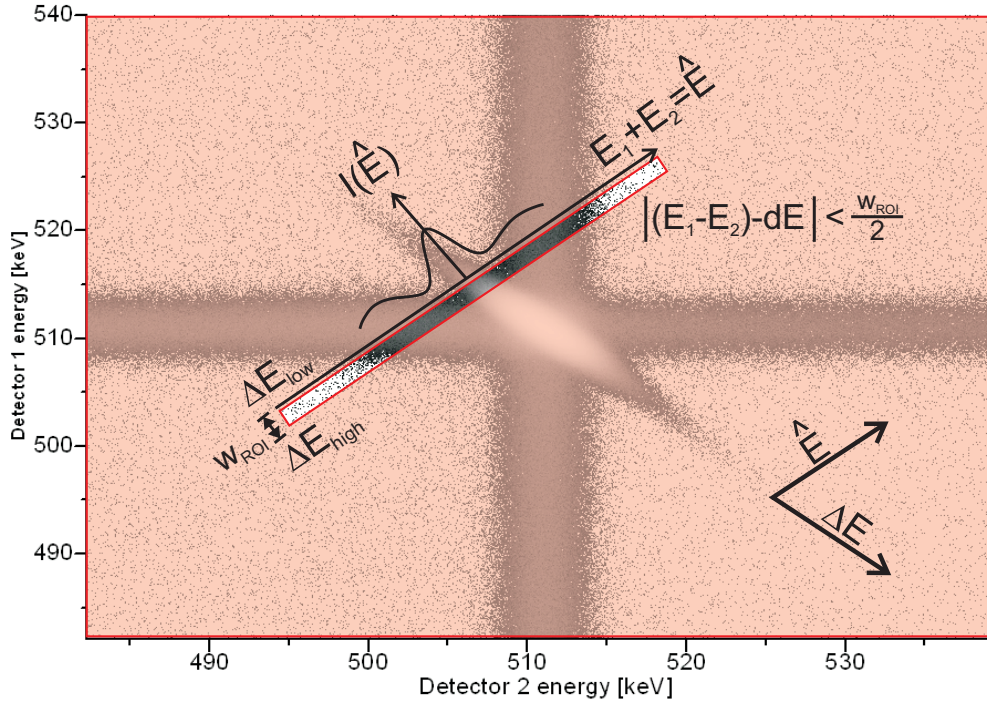

Figure 3.18.: The projection of one single ROI perpendicular to the Doppler broadening. The area of the ROI is projected onto the sum energy axis $\hat{E}$. The projection result is processed by Gauss-fitting like illustrated in fig. 3.19.

Gauss fitting & error calculation

The process of Gaussian fitting to projections $I_{dE}(\hat{E})$ with various difference energy dE is illustrated in figure 3.19. The orange lines in part a) mark the dE-values for the exemplary energy differences, where projections $I_{dE}(\hat{E})$ have been calculated and Gauss-fitted. Partial figure b) results from the projection of a center cut ($dE = 0.2$keV), where the count rate is very high but also the disturbances directly overlap with the annihilation line. Partial figure c) illustrates the same procedure at low Doppler shifts ($dE = 2$keV), where the disturbances begin to separate from the good events in the projection. Partial figure d) respectively shows the fit for a projection of the highest measurable Doppler shifts ($dE = 20$keV), where only the background overlaps with the undisturbed events but
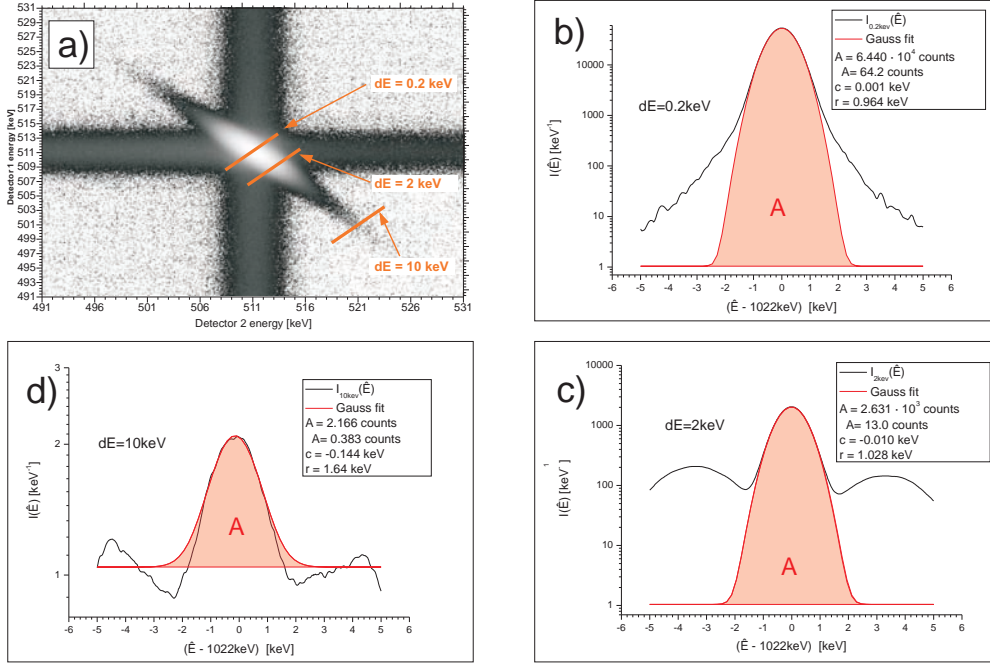
Figure 3.19.: Partial figure a) is an exemplary two-dimensional CDB spectrum. Partial figures b) to d) show the suppression of different disturbances by Gauss-fitting.

where the count rate is very low.

The Gauss-fitting causes a suppression of all disturbances which are not Gauss-shaped in the projection over $\hat{E}$. The area of the Gaussian A equals the number of counts in the evaluated ROI. The width of the Gauss fit r is directly measuring the resolution of the detectors and is averaged and reported by the evaluation software. The center of the Gauss fit c measures the deviation of the annihilation peak from its $1022\,\text{keV}$ sum energy position. This value is also reported in dependence of the Doppler shift $c(dE)$ and can be used to measure the binding energy deficit. (see section 4.2).

The output F of the Gauss-fitting procedure is divided by the width of the ROI w_{ROI} to make results with different w_{ROI} comparable.

$$F = \frac{A}{w_{\text{ROI}}} \left[keV^{-1} \right] \tag{3.6}$$

For Doppler broadening evaluations, F is the most important result, because it́s Doppler-shift dependent function $F(\Delta E)$ corresponds to the undisturbed spectrum of the annihilation line.

The error σ_F has to be calculated for two components: σ_A is a further result of the fitting procedure, which is calculated from χ^2 in the center of the peak, which is defined by the width of the Gauss fit r. The area outside of the center is not used for χ^2 calculation because it contains disturbances which are not modeled by the fit.

The second component of the error calculation is the statistical error $\sqrt{A}$. The area of the fit A is the number of events in the evaluated ROI of the two dimensional spectrum. Because the collection principle (see appendix A.2) smooths the data before it is Gauss-fitted, the statistical error is not completely contained in χ^2.

The total error is calculated by quadratic summation of the fitting error and the statistical error:

$$\sigma_F = \frac{\sqrt{A + \sigma_A{}^2}}{w_{\mathrm{ROI}}} \tag{3.7}$$

3.3.4. Variable ROI width

In the new evaluation program, the set of target energies is already chosen before the 2-dimensional spectra are processed. The difference of two target energies dE in the table defines the ROI width w_{ROI}. This way, each DB-spectrum calculated by the new evaluation program can be directly compared to each other and ratio curves can be obtained by simple division.

The setting of the ROI width is a compromise. Small ROI widths deliver better energy resolution in the processed spectrum, whereas a large ROI width collects more events for a single Doppler shift and therefore results in a lower statistical error. Furthermore, there are very high counting rates in the low momentum part of the spectrum, while counts of high Doppler shifts are comparatively rare. This distribution is best evaluated by using a variable size w_{ROI}, in order to display the low momentum part with highest possible resolution, while the high momentum part is optimized for statistics. In the region over 520 keV Doppler events are so rare, that the bin size even may exceed the detectors resolution (1.3 keV) to collect an processable amount of events at all.

Table A.1 (Appendix) contains a typical set of ROIs which was regularly used for CDBS evaluations with variable binning. Its ROI widths w_{ROI} are adapted empirically to good energy resolution in the low momentum range and best statistical significance in the high momentum range. $dE(n)$ is the energy value that is designating the according ROI with No. n for a set of $n_{\max}$ target energies. The limits of the $ROI_n = [\Delta E_{\mathrm{low}}, \Delta E_{\mathrm{high}}]$ are calculated by the evaluation program according to the following table. The position of the regarding energy shifts is illustrated in figure 3.20.
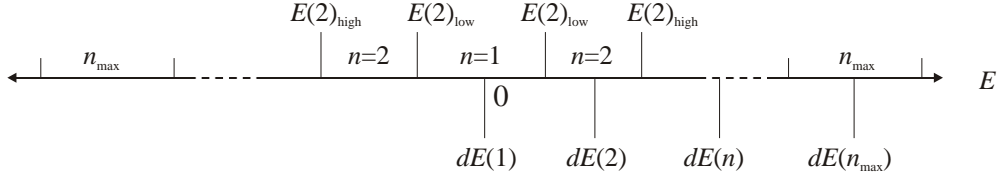
Figure 3.20.: The calculation of energy shift intervals $[\Delta E(n)_{\text{low}}, \Delta E(n)_{\text{high}}]$ from an unequally spaced set of target energies $dE(n)$. For $dE(1) = 0\,\text{keV}$ a central interval over $\Delta E = 0\,\text{keV}$ is spawned. For the other target energies $n \geq 2$ two symmetrical energy shift intervals are chosen in a way without overlap. For $n = 2$ the position of $\Delta E(n)_{\text{low}}$ and $\Delta E(n)_{\text{high}}$ as well as of the symmetrical interval is designated.

$\forall n \in [1..n_{\max}]$	$n = 1$	$1 < n < n_{\max}$	$n = n_{\max}$
$\Delta E_{\text{low}} =$	$-\frac{dE(1)+dE(2)}{2}$	$\frac{dE(n)+dE(n-1)}{2}$	$\frac{dE(n)+dE(n-1)}{2}$
$\Delta E_{\text{high}} =$	$\frac{dE(n)+dE(n+1)}{2}$	$\frac{dE(n)+dE(n+1)}{2}$	$2 \cdot dE(n) - \Delta E_{\text{low}}$
$\overline{E_{\text{high}}} =$	$[]$	$-\Delta E_{\text{low}}$	$-\Delta E_{\text{low}}$
$\overline{E_{\text{low}}} =$	$[]$	$-\Delta E_{\text{high}}$	$-\Delta E_{\text{high}}$

$\overline{E_{\text{low}}}$ and $\overline{E_{\text{high}}}$ are the mirrored energy intervals. They are summing up of both symmetrically sides of the Doppler broadened annihilation line. This definition of the ROI ensures that there is no overlapping of ROIs with variable width.

The advantage of variable ROI size w_{ROI} evaluation can be directly seen in the Doppler spectrum of a single measurement. Figure 3.21 compares the reference measurement on zinc using a fixed step width and a commonly used set of variable size ROIs. The main improvement of variable ROI size is the significantly lower statistical error in the high-momentum area. For further comparison, also the result of the previously used projection algorithm is displayed in this diagram. The green line $I_P(E)$ is the original output of the projection software MSPEC without background correction. The black line $\bar{I}_P(E)$ results from the same projected spectrum, but with a constant background correction. The background subtraction is necessary to compare the Gauss-fitting with the projection results, because Gauss-fitting inherently eliminates the constant background, while the conventional projection results include the background, dependent on the projection ROI
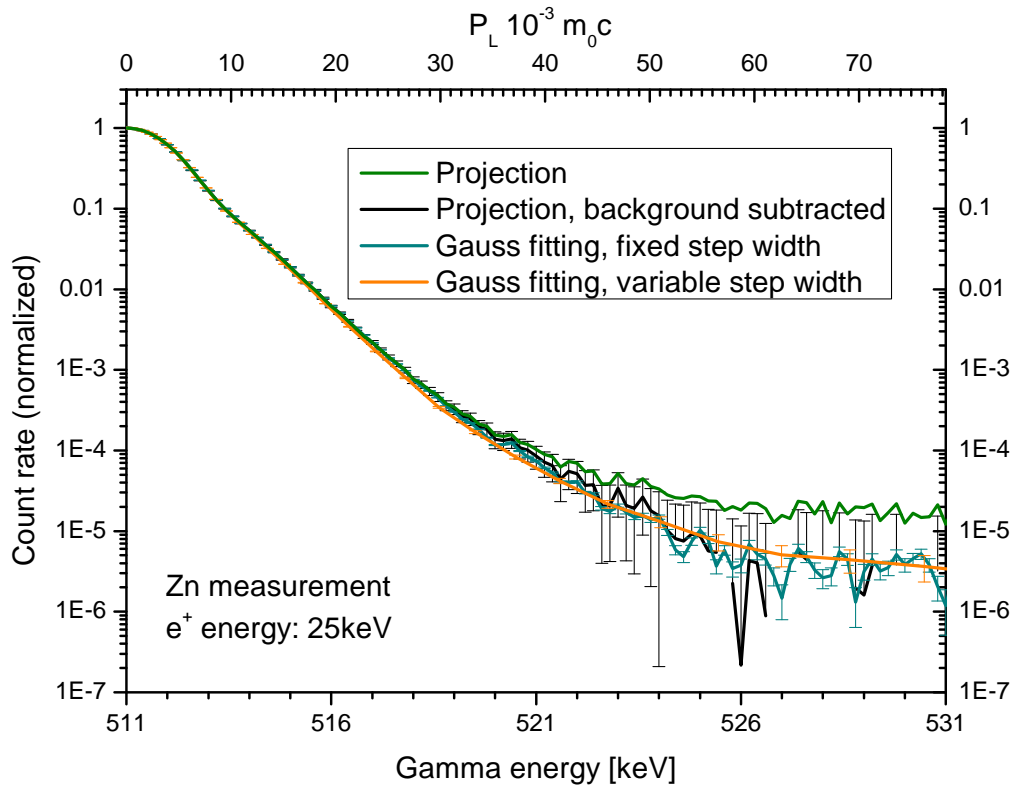
Figure 3.21.: The same CDB measurement evaluated with fixed and variable binning.

width. For the background correction of the black line, the data at the Doppler shift $\Delta E = 25\,\text{keV}$ according to $E = 536\,\text{keV}$ was used because this energy is out of range of measurable Doppler shifts.

$$\bar{I}_P(E) = I_P(E) - I_P(536\,\text{keV}) \tag{3.8}$$

For better clarity the error bars in figure 3.21 are only displayed for the background corrected results.

3.3.5. Ratio curves

For convenient viewing, the CDBS results are usually presented in a mode which is referred to as ratio curves. The projection results (Figure 3.22, left part) are normalized to one reference material and mirrored at their peak position, so that they loose their general

peak-shape and their differences get visible to the eye. Conventionally, this processing step requires one more interpolation, because the projected spectra do not always have the same binning energies. For this reason, the calculation of the ratio curves is embedded in the new CDB evaluation software, so that the program can generate Doppler broadening spectra $F(\Delta E)$ with an equal energy table of $\Delta E \in \{E_1, E_2, ..., E_{\max}\}$. Hence another interpolation procedure, which principally degrades the spectrum's resolution, is avoided.
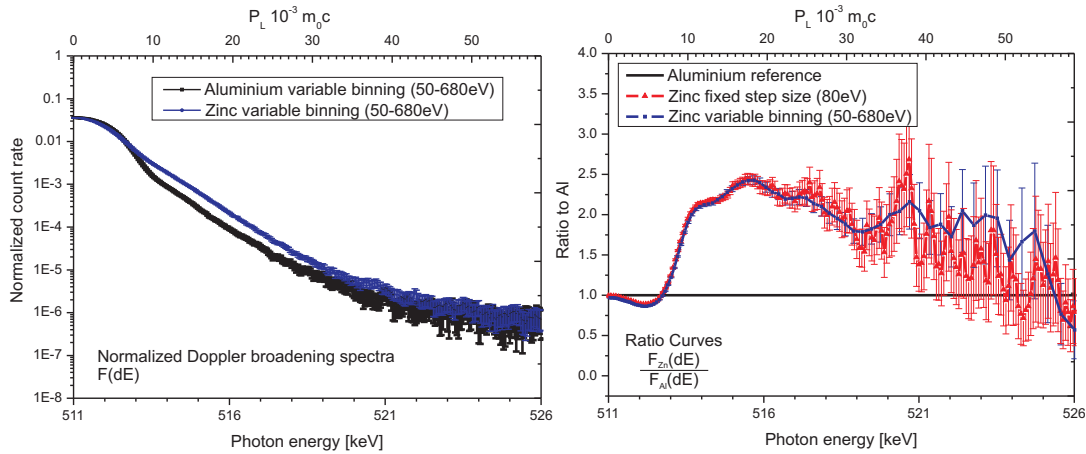

Figure 3.22.: Ratio curves are calculated from the normalized Doppler broadening spectra (left side) by division. On the right side, ratio curves from fixed and variable binning are compared.

The right part of figure 3.22 shows exemplary ratio curves of the CDB spectrum of zinc, normalized to the spectrum of aluminium. The result is presented once using a fixed bin size (red curve) and an evaluation with variable binning (blue curve). Due to the ratio curve illustrations even small differences in the absolute counting rates can be easily recognized by eye. In the area of high counting rates $(0-15m_0c)$ the results are practically identical due to similar bin sizes. In the high-momentum range which is most important for the interpretation of CDB-results $(10-30m_0c)$ the curves are close to each other, but in this place the variable bins are larger and hence the statistical error is significantly lower. In the highest momentum range $(30-55m_0c)$ the results with fixed binning are insignificant compared to their respective error values, while the variable bins are that big, that energy resolution of the spectrum is degraded, but count rates are still sufficient for statistically significant results. For momenta over $55m_0c$ no useful information can be gathered from the zinc spectrum anymore.

3.3.6. Ratio fitter

In many CDB applications, a mixture of elemental signatures in a binary system of the components A and B is measured. For the quantitative evaluation of the results, it is of high interest, which ratio η defines a linear combination $F_{AB}(\Delta E)$ which fits best to the measurement result.

$$F_{AB}(\Delta E) = \eta \cdot F_A(\Delta E) + (1 - \eta) \cdot F_B(\Delta E) \ \forall \ \eta \in [0..1] \tag{3.9}$$

$F_A(\Delta E)$ is the CDB spectrum of component A and $F_B(\Delta E)$ of component B respectively. $F(\Delta E)$ is the measurement containing both components A and B.

To find the best value for η a least square error fit is applied. Hence the function $Q(\eta)$ is minimized.

$$Q(\eta) = \int_{\Delta E = \Delta E_{\min}}^{\Delta E_{\max}} (F(\Delta E) - (\eta \cdot F_A(\Delta E) + (1 - \eta) \cdot F_B(\Delta E)))^2 \, d\Delta E \tag{3.10}$$

The minimum of $Q(\eta) \ \forall \ \eta \in [0, 1]$ reflects the fraction η of positrons annihilating with core electrons of the component A in a binary system.

The energy window $[E_{\min}, E_{\max}]$ which is used for the fitting procedure is user-definable. $E_{\min}$ should be chosen high enough so that annihilations with valence electrons are neglected, while $E_{\max}$ should be in the range of maximal measurable Doppler shifts.

3.3.7. Conclusion

The new evaluation algorithm clearly enhances the efficiency of CDB spectroscopy. The Gauss-fitting procedure itself provides an effective background suppression which enhances the signal to noise ratio of the Doppler-broadened annihilation line from $\approx 10^5$ to $\approx 10^6$ (see figure 3.17). The variable ROI size evaluation enables the interpretation of very high momentum Doppler-shifts $(> 45 \, m_0 c)$ and generally reduces the statistical error, so that short CDB measurements $(\geq 1 \, \text{h})$ already deliver significant results. At last, the evaluation by fitting the approximately Gaussian instrument function, not only delivers the Doppler-shift dependent count rate, but also the energy resolution of the instrument and the precise center of the annihilation line, which enables measurements of binding energies with CDBS (see section 4.2).

4. CDBS on reference samples

4.1. Database of pure elements

The (coincident) Doppler spectrometer at NEPOMUC is part of a user facility. Due to its unprecedented short measurement times and high quality of the acquired spectra, a large number of samples is measured. Thanks to the constant instrumental conditions, one can directly compare new to prior CDBS results. Especially measurements on pure elements serve as reference spectra which can be reused for comparison after they are once recorded.

For this reason, all recorded spectra are stored and handled in a database. A file structure (see Appendix B.2.1) and a front end for the projection software were developed which enables convenient and quick access to all results, while the software automatically ensures uniform processing of all data. Hence an unprecedented number of different reference materials was measured which are used to calculate ratio curves. All measurements on elements listed in table 4.1 have been performed with high purity ($> 99.99\%$) and well annealed materials. The ratio curves to a silicon reference are shown in figure 4.1.

In this figure the ratio curves are sorted to different groups. The group of the noble metals and the group of the transition metals 26-30 (Fe, Co, Ni, Cu, Zn) exemplarily show the capabilities of CDBS to distinguish different elements. The signatures of the noble metals mainly differ in their amplitude, and not in their slope. Hence, this set of noble metals cannot be distinguished in the CDB spectrum easily.

Lighter elements have more distinct variations in their orbital structure so that more distinct differences in the CDB spectra are expected. Indeed in the group of the transition metals only Fe and Co carry a similar CDBS shape due to their similar electron configuration. All other metals in these group are clearly distinguishable in spite of being neighbors in the same period of the periodic table of the elements. The measured spectrum of annealed copper shows one of the highest amplitudes in the momentum range from $10 - 20 \cdot 10^{-3} \, m_0 c$ which is reported so far.

The comparison of reference elements illustrates again the advantage of the data processing with variable binning, which enables evaluation of Doppler shifts up to $60 \cdot 10^{-3} m_0 c$ with standard measurement times of typically 3 hours according to about 20 million counts in the coincident photo peak.
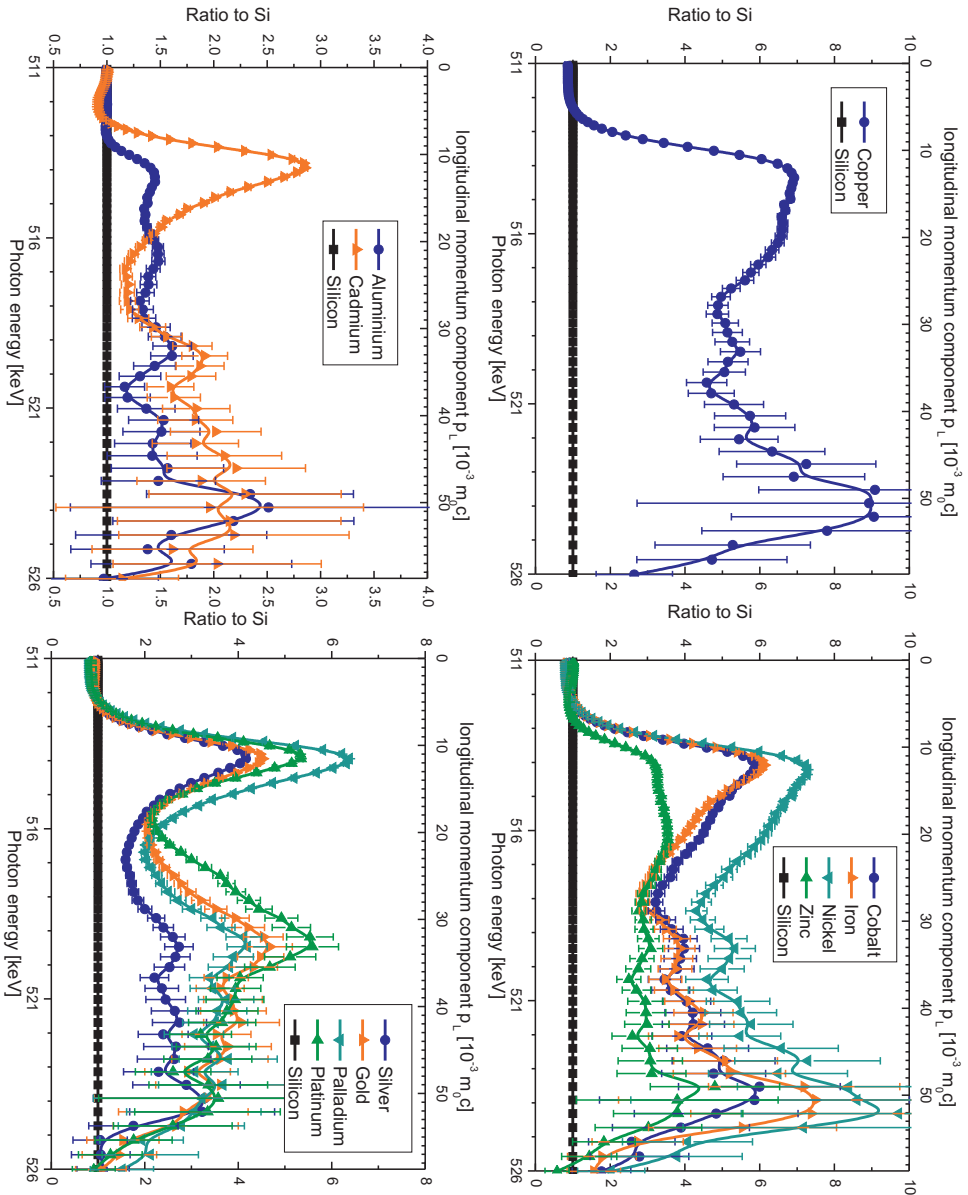
Figure 4.1.: Ratio curves of all measured reference elements. All plots are normalized to silicon. Variable binning is used. The lines in all CDB spectra presented in this work are plotted to guide the eye.

The reference element database gives a good opportunity to test theoretical calculations of CDB spectra by comparison with measured results. Figure 4.2 shows this exemplarily for three different elements, for copper, gold and silicon. Due to restrictions of the used atomic superposition calculation tool MIKA-Doppler the low momentum area up to $17 \cdot 10^{-3} m_0 c$ can not be simulated accurately [58, 59]. For higher Doppler momenta, the simulated data shows a deviation for the reference curve of gold, which is known to be non-well described. The spectra of copper and silicon show excellent agreement, which additionally confirms the correct function of the annihilation radiation detection system as well as of the new evaluation algorithm.

	Element	E_{kin}^+ [keV]	E_{res} [keV]
Ag	Silver	15	1.09
Al	Aluminium	30	1.12
Cd	Cadmium	15	1.10
Co	Cobalt	25	1.15
Cu	Copper	25	1.18
Au	Gold	25	1.11
Ni	Nickel	25	1.15
Pd	Palladium	25	1.21
Pt	Platinum	25	1.11
Si	Silicon	20	1.12
Zn	Zinc	25	1.12
H_2O	Water	7	1.09
SiO_2	Quartz	25	1.17

Table 4.1.: The reference measurements performed at NEPOMUC. E_{kin}^+ designates the energy of the positron beam. For spectra of pure elements, typically E_{kin}^+ is chosen over 15 keV to prevent back diffusion to the surface. E_{res} is the effective energy resolution of the coincident detector system.

CDBS on Water

The measurement of water with a monoenergetic positron beam evoked a special experimental challenge. The positron beam can only be applied to the sample, if the quality of the experimental chambers vacuum is better than $\approx 10^{-5}$ mbar. To reach this pressure with water as sample, the temperature of the sample has to be kept below $\approx 188\,\text{K}$ [60]. The problem is, for insertion of the sample the experimental chamber has to be vented while the sample holder is at room temperature, otherwise the high voltage isolators in the instrument will fail due to condensation. Hence, liquid water has to be inserted in a crucible into the vented chamber. Then, the chamber has to be evacuated while the tem-
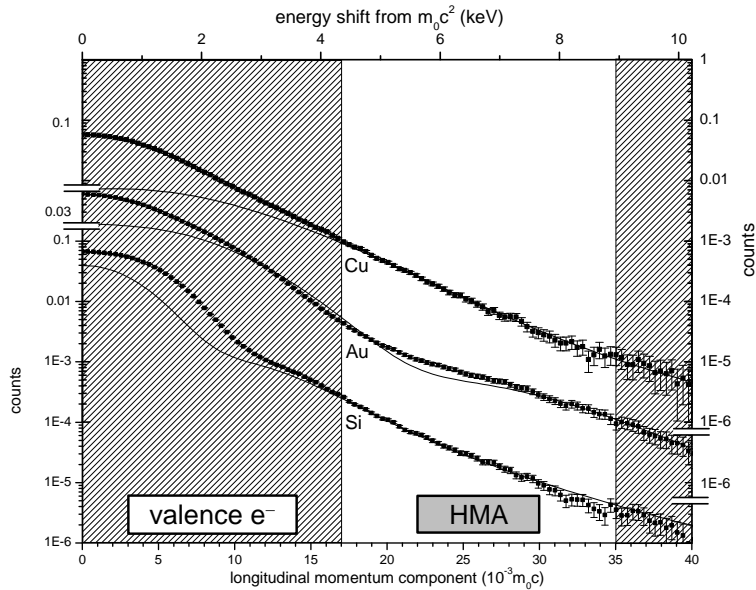
Figure 4.2.: Comparison of calculated and measured spectra. Continuous lines are simulated data points, the points with error bars are measurements.

perature of the sample holder is quickly lowered. Consequently the water freezes, during water vapor is removed by the vacuum pumps and the isolators stay clean. Principally, part of the water vaporizes during this process, so that a clean surface remains.

This method requires de-gassed water. For this purpose, the chamber pressure can be decreased periodically before final evacuation, until no bubble formation occurs before the camber's pressure falls below the vapor pressure of water. This way, a clear block of crystalline ice can be produced in vacuum conditions.

4.2. Electron binding energies determined with CDB

4.2.1. Extraction of binding energies from 2D CDB spectra

The low background of coincident Doppler broadening measurements is based on the evaluation of the sum energy E_{sum}, which is usually regarded to be 1022 keV in the case of a valid detection of the annihilation photons in both detectors (see section 3.3.1). Precisely, the sum energy is not 1022 keV, it is slightly reduced by the binding energy E_B of the annihilated electron.

$$E_{\text{sum}} = E_1 + E_2 - E_{\text{B}} = 1022\,\text{keV} - E_{\text{B}} \tag{4.1}$$

E_1 and E_2 are the energy values of a collinear emitted photon pair. In practical use, E_{B} is often neglected due to its level in orbitals with a significant positron annihilation probability [37], which is usually one order of magnitude lower than the energy resolution of the used detector system.
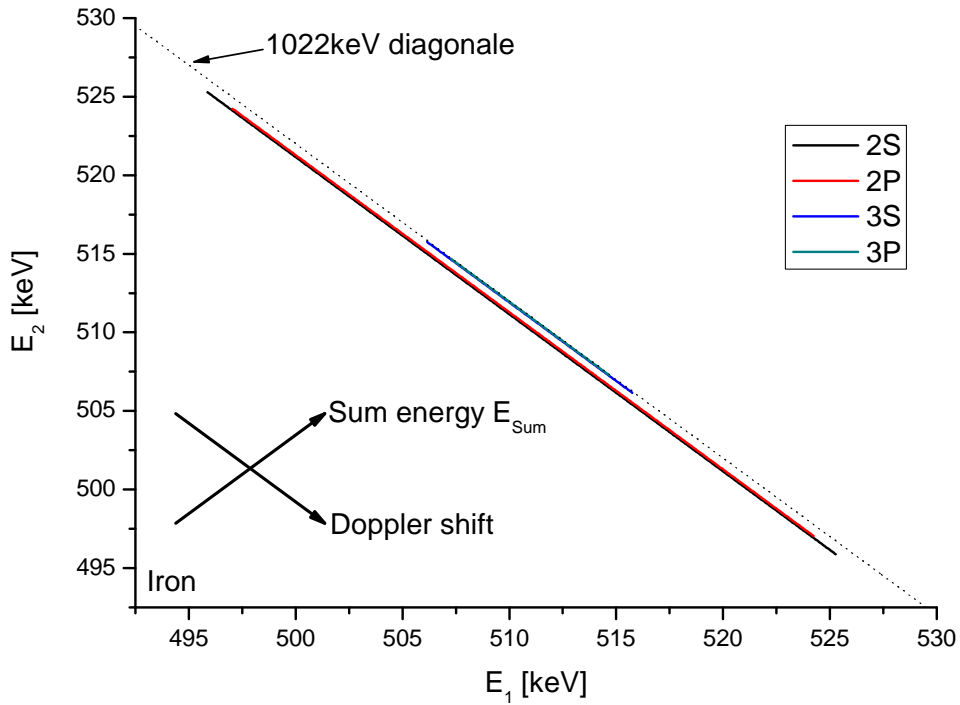

Figure 4.3.: The schematic distribution of annihilation events from different orbitals in the CDB spectrum, exemplarily for iron. The diagonal arrows designate the axis of sum energy and Doppler shift. The distance of the event to the 1022keV diagonal on the sum energy axis is the sum energy deficit ΔE_{sum}.

In order to find out, whether the binding energy can be identified in the CDB spectrum, iron was chosen due to its 2s and 2p orbitals, which annihilate with positrons with a 0.034 % and 0.076 % probability [37]. The binding energy of these orbitals is 845 eV and 720 eV respectively.In the 2-dimensional CDB spectrum, the according events may be isolated in the outer wings of the Doppler broadened photo peak. As figure 4.3 illustrates, the different orbitals of the measured element contribute to different areas in the 2-detector

spectrum. The Doppler broadening leads to diagonal lines in the spectrum which are confined by the maximal momentum of the electron in the direction of the detector axis. All events on one line have the same sum energy. This respective sum energy varies slightly due to the energy deficit caused by the binding energy. In the schematic diagram of figure 4.3 it is visible that the 3p and 3s orbitals practically overlap with the 1022 keV line due to their low binding energy. The 2p and 2s orbitals have a broad area of high Doppler shifts, which is undisturbed by other events. Although the annihilation rate with these core orbitals is below 0.1%, the signal background in the relevant quadrants of the spectrum is in the range of 10^{-5} compared to the photopeak, so that a measuerment of 2p and 2s electron annihilations was expected to be feasible. The according events are expected to be placed below the 1022 keV line. Their distance to the 1022 keV diagonale is called sum energy deficit ΔE_{sum}.

So far, such an effect was not accessible because after conventional projection (see section 3.3.2) of CDB spectra the exact sum energy information is lost. The new evaluation algorithm, developed in the scope of this work, works by fitting the instrument function of the detector system, approximated by a Gaussian, to cuts in the spectrum with a common amount of Doppler broadening (see section 3.3). For the usual evaluation of CDB spectra, only the amplitude of the Gauss-fits is necessary. But the fitting algorithm also provides the width of the Gauss-function, which can be used to determine the detectors resolution, as well as the center of the peak.

In case of neglected binding energies, all Gauss-fits should center on the 1022 keV line of sum energy. In the case that isolated areas of the spectrum are visible with a binding energy which is significant compared to the detectors resolution of about 1.3 keV, the center of the Gauss-Fits should be shifted accordingly.

One more problem arises from the limited detector resolution. Due to the ratio of core annihilation probability between the 3s and 2p orbital, which amounts to more than 25, various events from the 3s and 3p lines stray into the Doppler broadening area of the 2p and 2s orbitals. This blurs the distribution of the energy deficit.

Figure 4.4 is a plot of the centers of the Gaussian fits (green crosses) directly on the 2-dimensional CDB spectrum. Counts of more than 10 events are clipped to pronounce the low count rate high-momentum part of the spectrum. For comparison, the yellow dotted line shows the diagonal line of Doppler shifted annihilations with exactly 1022 keV sum energy.

In the raw data (blueish to white points) the binding energy is not visibly by eye. The centers of the Gaussian fits (green crosses) follow the 1022 keV-diagonal in the center area. In the area between 517 keV and 520 keV a significant deviation to lower sum energy gets visible, which is attributed to the binding energies of the 2s and 2p orbitals. Over 520 keV the number of counts in the measured data is to low to generate stable Gauss fits and
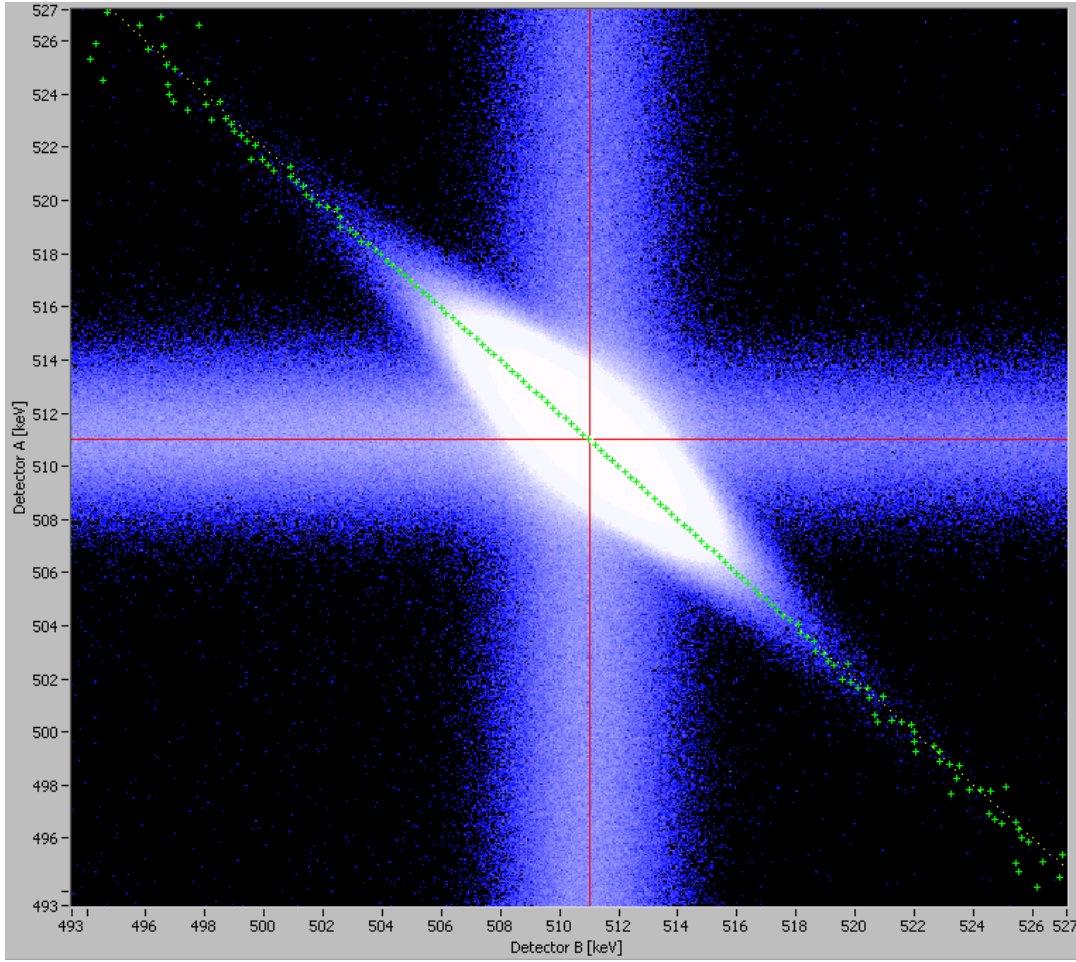
Figure 4.4.: 2D plot of the CDB spectrum for Fe: The electron binding energies can be extracted from deviation of the annihilation line centers (green crosses) from the 1022 keV-diagonal (yellow dotted line).

hence the center position varies largely.

4.2.2. Calculations

For the calculation of the two dimensional Doppler spectrum, the contributions from the relevant orbitals are calculated separately. The count rate $I_n(p)$ in the line shaped Doppler broadening areas is approximated by a parabolic function due to the projection of an isotropic electron momentum distribution to one dimension (see section 2.3.2). The intensity of each line is set to the respective core annihilation probability. The spectra are folded with a Gaussian function with a FWHM of 1.35 keV which represents the detector resolution $Res(E)$. Then for each specific value of Doppler shift, the weighted average of

the sum energy is calculated.

$$I_n(p) = \overbrace{\frac{\sqrt{p_{\max,n}^2 - p^2}}{\frac{2}{3} \cdot p^3}}^{0 \, for \, intensities < 0} \cdot P_{\text{Ca},n} \tag{4.2}$$

$$Res(E) = \frac{1}{\sqrt{2\pi}} \cdot e^{-\frac{1}{2}\left(\frac{E \cdot 2\sqrt{2ln(2)}}{\text{FWHM}}\right)^2} \tag{4.3}$$

$$E(p) = 511\text{keV} + \frac{1}{2}cp \tag{4.4}$$

$$I_{\text{folded}\,n}(p) = (I_n(p) * Res(E(p))) \tag{4.5}$$

I_n is the intensity distribution of each orbital n dependent of the Doppler shift p and is normalized to the core annihilation probability P_{Ca}. $p_{\max}$ is the maximum Doppler shift of the orbital n which can be easily calculated due to conservation of momenta (see section 2.3.2).

$$\hat{E}(p) = \frac{\sum_{n=1}^{n_{max}} I_n(p) \cdot (1022keV - E_{\text{B}\,i})}{\sum_{n=1}^{n_{max}} I_n(p)} \tag{4.6}$$

$\hat{E}(p)$ is the median sum energy of all events with a specific Doppler shift p. n_{max} is the number of orbitals included in the calculation. $E_{\text{B},n}$ is the binding energy of the respective orbital.

4.2.3. Comparison with experimental results and discussion

In figure 4.5 the measured sum energy deficit ΔE_{Sum} and the calculated sum energy deficit $\hat{E} - 1022\,\text{keV}$ are plotted. The statistical error of the measured values is calculated by variance analysis of neighbored but independent evaluation points.

In the momentum area of $15 \cdot 10^{-3} m_0 c < p < 30 \cdot 10^{-3} m_0 c$ a significant decrease of $\hat{E}$ is visible. This sum energy deficit is in good agreement with the calculated data. The deviation from the calculated data can be explained by the strongly simplified momentum distribution of the single electron orbitals. For $p > 30 \cdot 10^{-3}\,m_0 c$ the number of events in the evaluated area was to small to detect a stable center of the peak.

To test this new evaluation technique, two reference materials with very similar shape of the CDB spectrum have been evaluated for the Sum Energy Deficit Spectrum (SEDS) and calculations have been performed analogue to the iron measurement. Figure 4.6 shows the additional spectra. In the low momentum range the sum energy deficit is again in good agreement with calculation. But practically no distinction of the SEDS from gold and
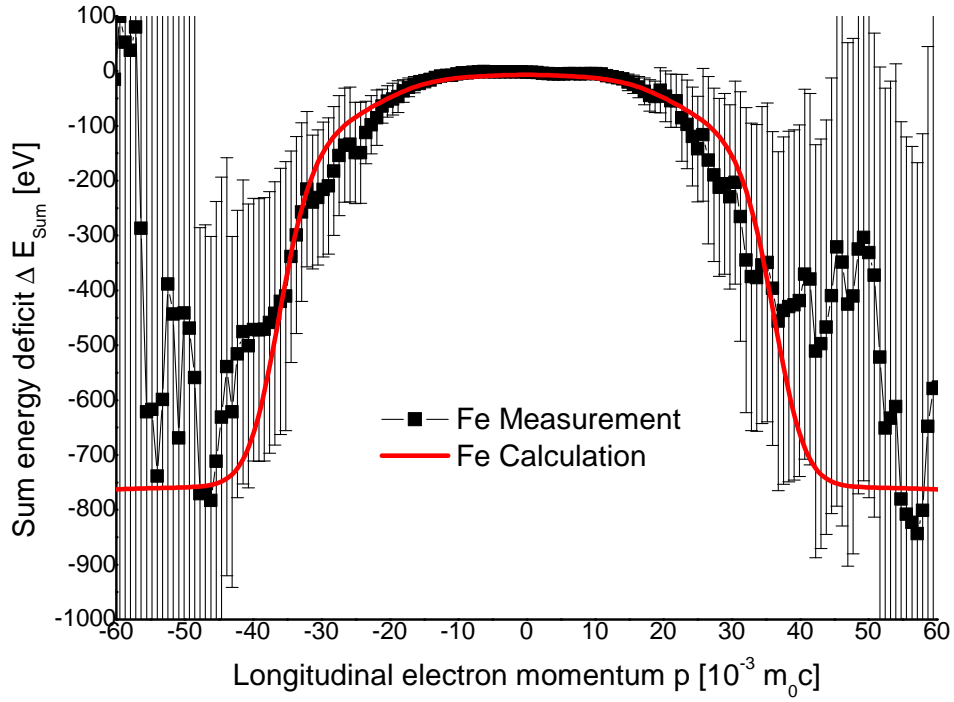
Figure 4.5.: For each Doppler shift p the center of weight $\hat{E}$ of the contributing events is calculated. The distance of the center of weight to the sum energy line of $1022\,\text{keV}$ (see figure 4.4) is the sum energy deficit, caused by the binding energy of the annihilated electron.

palladium is possible, because the measurement results lay completely in their mutual error bars. The calculated curves (cyan and orange) differ significantly in the momentum range of $20 < 10^{-3}m_0c < 32$ but the Gauss-fitting in these areas of the spectrum is not exact enough to show the differences at these measurement examples.
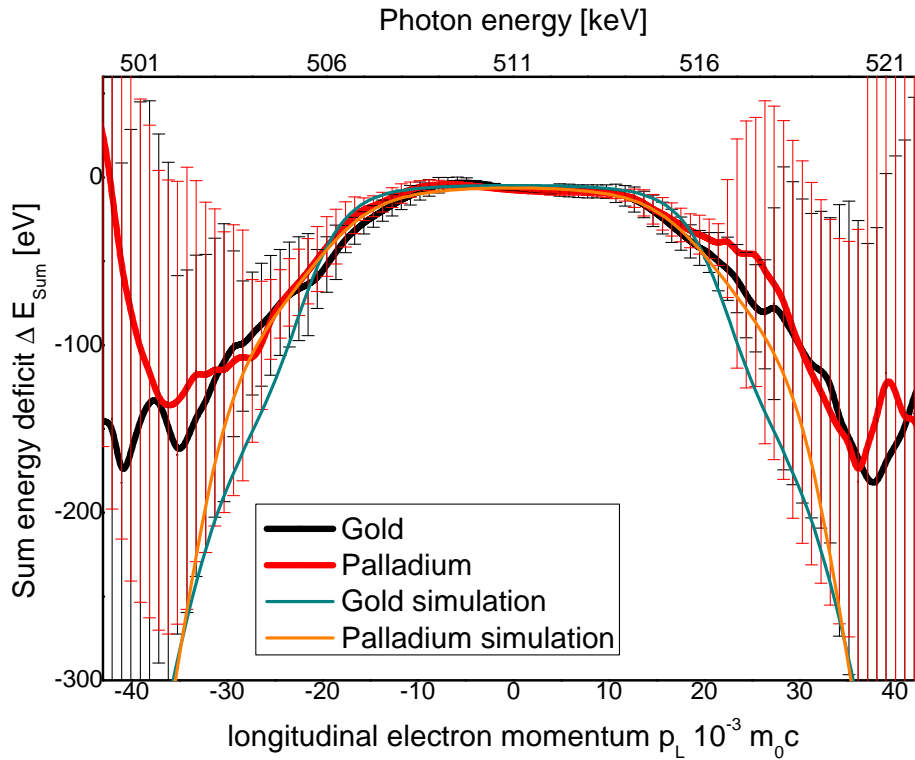
Figure 4.6.: The measured and simulated binding energy deficit spectra for gold and paladium.[1]

4.2.4. Conclusion

The measurement of the binding energies creates one element-specific parameter more than conventional evaluation of Doppler broadening only. It was shown that the sum energy deficit spectrum can be extracted from one CDB spectrum with a standard number of counts. For future applications, this may help interpreting indistinct CDB results which often occur when alloys or elements with a similar CDB-spectrum are measured.

To get more exact SEDS, more experiments with higher statistics and better energy

---

[1]In the momentum area from $20 \cdot 10^{-3} m_0 c - 32 \cdot 10^{-3} m_0 c$ a strong correlation between the simulated curve and the lower limit of the error bars seems to be visible. This is in accordance with the evaluation method, which calculates the error bars from the variation of the center of the Gauss fits. If the number of events gets too low to properly fit Gaussian functions, the result of the fit varies between the start values, which are defined by the 1022 keV diagonal and the statistically intermittent correct fit value. Hence the error bars are an indicator for the lowest limit of successful fits and therewith they follow the simulation curves in momentum areas of low counting rate.

resolution have to be performed. Furthermore, other material combinations, like iron and cobalt, which also have an almost identical CDBS shape, may be distinguished after extensive calculations of their core annihilation probabilities, which are not published for cobalt yet.

In conclusion this new data evaluation clearly proves the suitability of Gauss fit processing for the evaluation of CDB spectra. It could be shown that it is possible to extract one parameter more from CDB-spectra than with conventional projection methods. The possibility to simulate the SEDS results, enables the careful selection of materials for reference measurements, so that the possibility to identify elements by their binding energies is expected to be proofed with measurements with higher statistics in the $20-40 \cdot 10^{-3} \, m_0 c$ range.

5. Quantum confinement of positrons in thin metallic layers

The quantum confinement of positrons in metallic agglomerations is a topic of current research. For this reason, large parts of the following section are published in [13].

5.1. Study on metallic layers of various thickness and positron affinity

Agglomerations of atoms with a higher relative positron affinity $\Delta A^+ < 0$ (by definition, the negative sign specifies an attractive potential) form a trapping potential for positrons if the size of the agglomeration and the affinity difference ΔA^+ are appropriate. Therefore, due to its elemental selectivity CDBS is particularly suited to detect small metallic clusters or precipitates embedded in a matrix. In addition, the application of a monoenergetic positron beam allows to adjust the positron implantation depth which leads to a greatly enhanced sensitivity in a selected depth. For this reason, vacancy-like defects and precipitates in the near surface region of up to a few μm as well as layered systems can be measured.

For the investigation of layered samples, thin films or multilayers, conventional β^+ sources cannot be applied. For these studies, the use of a monoenergetic positron beam is required since the implantation profile can be adjusted by setting the positron implantation energy. This technique was first applied to Al covered polymer samples [61] and then to buried (ultra-) thin Sn layers in Al [9, 62]. In the latter experiment it was demonstrated that even a 0.1 nm layer of tin covered by 200 nm of aluminium is still detectable [9, 63]. The extremely high sensitivity to observe such a low amount of Sn was explained by efficient trapping due to the highly attractive positron affinity of Sn compared to Al [27] . The according calculation showed that in this system Sn clusters of sub-nanometer size in Al lead to a confinement of the positron wave function.

The present measurement of layered metallic systems shows three advantages over positron measurements on bulk binary systems. First, by choosing the thickness of the intermediate layer, the size of the embedded structure can be controlled. Second, the targeted implantation of the monoenergetic positron beam at the intermediate layer maximizes the trapping probability there and thus minimizes influences from the surface or

the substrate of the layer. Third, in the present study we extended our investigation to embedded metallic layers with elements of highly different positron affinities.

Consequently, the interfaces of the layer to the Al matrix are expected to form an attractive well which amounts to -1.82 eV for Au and -0.06 eV for Cu or even a repulsive potential of +1.58 eV at the Cr layers (see Table 5.2). The purpose of this experiment is the systematic examination of different materials and of different layer thicknesses to experimentally study the positron trapping probability and in particular its correlation to the structure size of the embedded layer. These properties are difficult to calculate due to the high number of concuring processes of the positron in the sample like trapping in open volume defects, in agglomerations or in phases of various alloys.

5.1.1. Calculations and samples

(Coincident) Doppler broadening spectroscopy and positron affinity

The positron affinities A^+ and the differences with respect to Al ΔA^+ were calculated from the experimentally determined values for Φ^+ and Φ^- given by Coleman [64] and are listed in Table 5.2. If multiple data was available as in the case of Al and Cu, A^+ was averaged for different crystallographic orientations. Assuming spherical clusters of the respective elements embedded in the Al matrix one can calculate its minimum size with the critical radius r_c that is necessary to form a bound state of the positron inside. According to the definition given above for $\Delta A^+ < 0$, r_c can be calculated in units of the Bohr radius a_0 by $r_c \cong 5.8 \cdot a_0 / \sqrt{|\Delta A^+| / [eV]}$ [27].

Calculation of the positron implantation profiles

The positron implantation profile in materials can be approximated by Makhovian functions with high precision [28]. Figure 2.1 exemplarily shows implantation profiles calculated for three different positron energies in Al. It can be clearly seen that a positron beam of 6 keV is well suited to study thin layers embedded below 200 nm Al. Hence, highest sensitivity to reveal information of the embedded layer at this depth is expected at medium energies like 6 keV where the overlap of the positron implantation profile with the intermediate layer is maximized. At 2.5 keV the positrons are implanted nearly completely in the cover layer of 200 nm whereas at 30 keV almost all positrons thermalize in the substrate. Consequently, by adjusting the positron implantation energy, results from CDBS can be gained for the cover layer, for the intermediate region and for the substrate.

Figure 5.1 shows the implantation profile calculated for a 6 keV positron beam in a 100 nm thick layer of Au embedded in Al. The high peak at the Au layer is attributed to the high density and high nuclear charge Z which result in high positron stopping power of Au. It was calculated that a fraction f=62.2 % of the positrons are directly implanted

into the Au layer, and the other fraction is implanted near the Al-Au interface. The fractions f of positrons implanted in the embedded layer were calculated for all samples and are summarized in Table 5.3. The required Makhov-parameters for Al, Cu and Au are taken from Puska et al. [28]. Since no experimental values for Cr are reported so far, the according parameters have been well approximated by linear interpolations as a function of the mass density. Vehannen [65] shows that a modified Makhovian function fairly represents the implantation in a layered system. If $P_x(z)$ represents the transmission probability function for a positron in a material x then a transmission probability function can be defined piecewise for a layered system according to table 5.1. The implantation density $P'(z) = \frac{\partial P(z)}{\partial z}$ (see section 2.2.1) is defined as the derivate of the transmission probability. Figure 5.1 shows the calculated implantation profile for the layered system with a gold layer of 100 nm thickness.

Layer	Depth	Function
Covering layer	$z \leq d_0$	$P_{Al}(z)$
Intermediate layer	$d_0 < z \leq d_0 + d$	$P_x(z + s_1)$
Substrate	$d_0 + d < z$	$P_{Al}(z + s_2)$
Continuity condition 1		$P_{Al}(d_0) = P_x(d_0 + s_1)$
Continuity condition 2		$P_x(d_0 + d + s_1) = P_{Al}(d_0 + d + s_2)$

Table 5.1.: The sections of the transmission probability function for a layered system of an Al substrate, an intermediate layer of material x and thickness d, and a covering layer of $d_0 = 200$ nm Al. s_1 and s_2 have to be solved to fulfill the continuity conditions.

element	a [nm]	Δa %	A^+ [eV]	ΔA^+ [eV]
Al	0.405	0	-4.28	0
Au	0.408	+0.7	-6.1	-1.82
Cu	0.361	-10.8	-4.34	-0.06
Cr	0.291	-28.1	-2.7	+1.58

Table 5.2.: Characteristics of the used elements: Layers of Au, Cu, and Cr are buried in the Al matrix. The lattice mismatch Δa is calculated from the lattice constants a of the respective bulk material by $\Delta a = a_{\text{layer}}/a_{\text{Al}} - 1$. The positron affinity A^+ is calculated from the work functions of the positron and the electron (experimental values from Coleman[64]). The relative positron affinity is defined as $\Delta A^+ = A^+_{\text{layer}} - A^+_{\text{Al}}$. Negative values of ΔA^+ indicate an attractive potential for positrons.
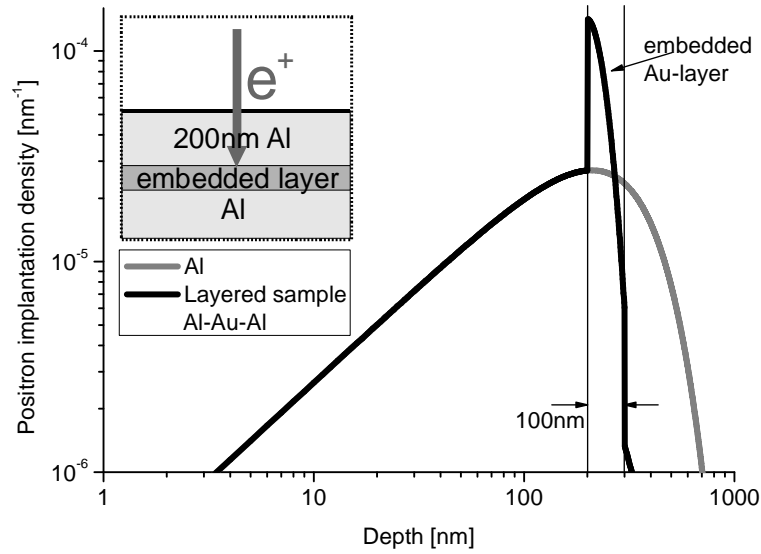
Figure 5.1.: The implantation profile of a 6 keV positron beam in a 100 nm thick layer of Au embedded in Al (sample no. 3) compared with the profile for pure Al.

Sample preparation

The general structure of the investigated samples is shown in the insert of Figure 5.1. The substrate consists of annealed Al of 1 mm thickness. Hence, even at a positron energy of 30 keV according to a mean positron implantation depth of 4.0 μm, no positron can reach the bottom. The layers according to Table 5.3 are grown by magnetron sputtering out of high purity materials at the Paul Scherrer Institute [13]. Magnetron sputtering produces films of comparatively high densities, i.e. samples with low amount of free volume [66]. Complementary Scanning Electron Microscopy (SEM) assured the quality of the samples. Vertical cuts have been performed with a focused ion beam and have been examined by SEM. The SEM images show the polycrystalline structure of the intermediate and cover layer, while the crystallites of the annealed substrate are too large to be visible in the image dimensions. As an example, the SEM image of the 100nm chrome sample is shown in Figure 5.2. The rough structure of the sample surface, which is visible above the cutting edge is a side effect of the ion-beam cutting.
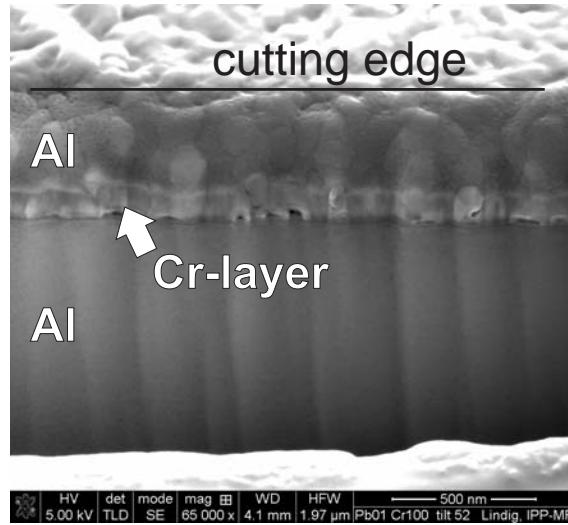
Figure 5.2.: An electron microscopic (SEM) image of the focused ion beam (FIB) prepared sample with a 100 nm Cr layer embedded in Al (sample no. 7).
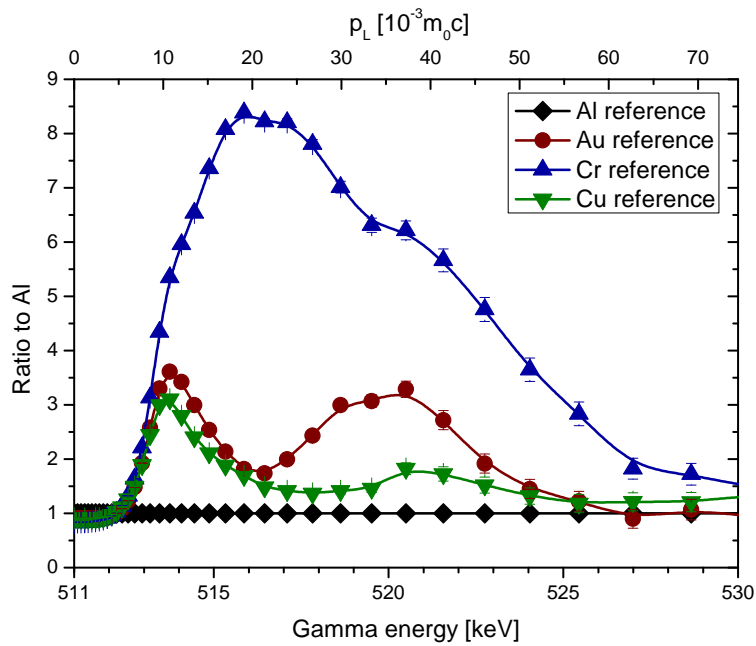

Figure 5.3.: CDBS results of the pure reference materials. All recorded spectra were divided by the spectrum of pure Al to show the element specific shapes as clearly distinguishable ratio curves.

no.	element	d	f	η
		[nm]		
1	Au	0.5	0.006	0
2	Au	2	0.024	0.83
3	Au	100	0.622	0.92
4	Cu	10	0.081	0
5	Cu	100	0.561	0.88
6	Cr	10	0.087	0
7	Cr	100	0.574	0

Table 5.3.: The layered samples: The thickness of the layer consisting of the listed element embedded in Al is denoted with d. The cover layer at all samples is 200 nm Al. The calculated fraction of positrons implanted into the layer with a positron beam of 6 keV energy is f. The experimentally obtained values of η reflect the relative portion of positrons annihilating with electrons from elements of the layer [13].

5.1.2. CDB measurements and results

Reference spectra and energy dependent CDBS

CDB measurements on reference samples of high-purity materials (Al, Au, Cr, and Cu) were performed. The ratio curves (Figure 5.3) show that all elements are clearly distinguishable compared to the aluminium substrate.

Energy dependent CDB measurements on sample no. 2 with the 2 nm Au layer embedded in Al were performed in order to confirm the calculated implantation profiles. The according ratio curves obtained for a positron energy of 2.5, 6 and 30 keV are shown in Figure 5.4 A2. At 6 keV the Au layer is clearly visible due to the targeted positron implantation in the layer's depth. At 2.5 keV the positrons are implanted near the surface in the cover layer according to Figure 2.1. At 30 keV almost all positrons are implanted in the Al substrate at a mean depth of 4 μm. In contrast to the implantation at 6 keV no Au signature is revealed at 2.5 and 30 keV implantation energy. Consequently, the results confirm the implantation calculations and clearly demonstrate the advantages of using a monoenergetic positron beam and thin layered systems.

Layers of Cr, Cu and Au embedded in Al

The ratio curves obtained by CDBS for all layered samples are presented in Figure 5.4. Figure 5.4 C shows the spectra of the samples with Cr layers embedded in Al (samples no. 6 and 7). As expected due to the repulsive positron affinity of Cr in Al the 10 nm layer is not visible in the spectrum. Even the measurement in the 100 nm layer revealed no significant contribution of the pronounced Cr signature, although according to the Makhov
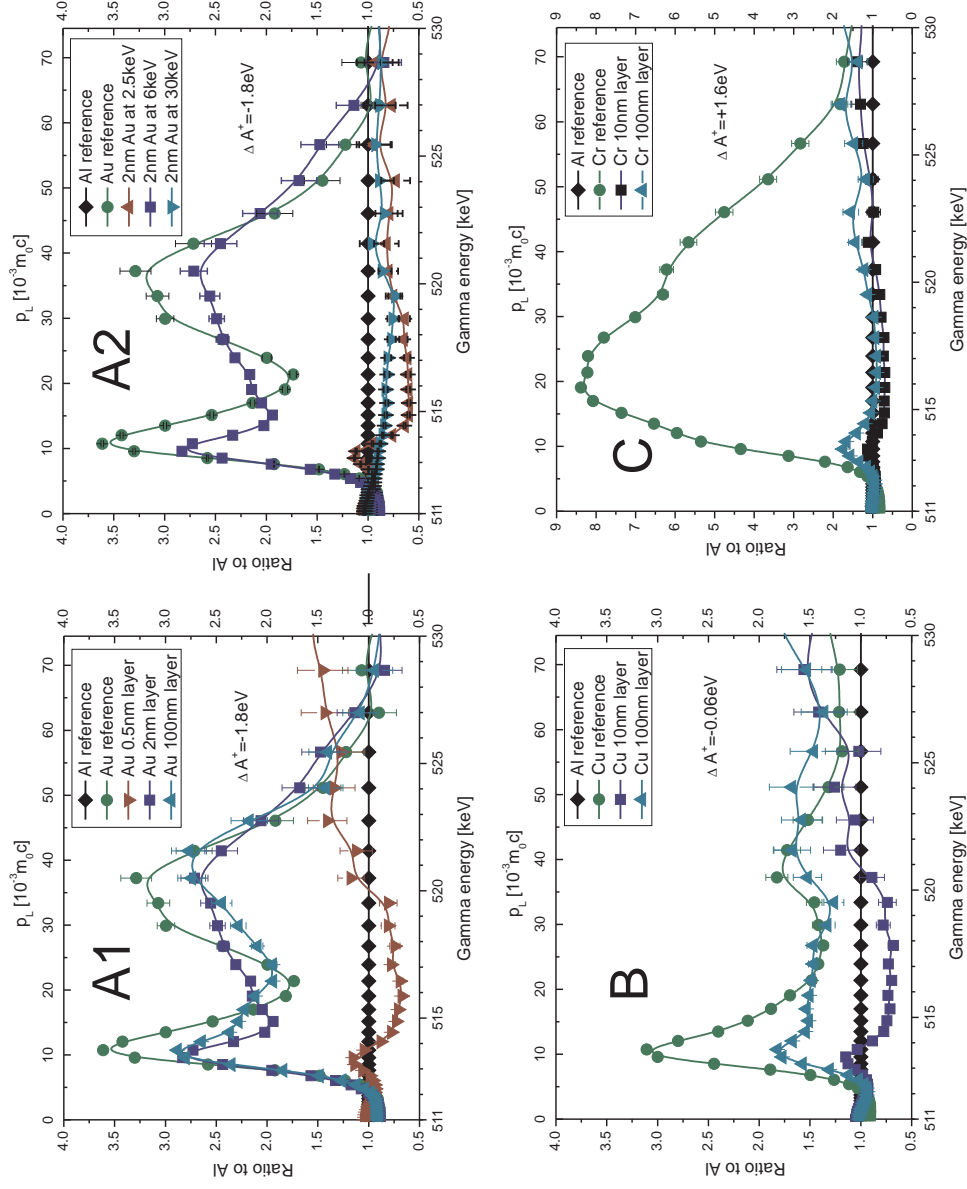
Figure 5.4.: Ratio curves of metallic layers of different thicknesses embedded in Al: Au in Al (A), Cu in Al (B), and Cr in Al (C). The respective reference spectra of the pure elements are plotted as well. Note the different relative positron affinity ΔA^+ of the layered systems (see Table 5.2) [13].

calculations 57.4 % of the positrons are implanted in the layer.

In Figure 5.4 B the results of two embedded Cu layers with different thickness are presented (samples no. 4 and 5). The 100 nm layer, in which 56.1 % of the positrons are implanted, creates a clearly visible Cu signature, whereas the spectrum of the 10 nm Cu layer is similar to that observed at the thin Cr layer.

The ratio curves for three different embedded Au layers (samples no. 1-3) are shown in Figure 5.4 A1. Due to the highly attractive positron affinity of Au in Al, a clear Au signature at the 100 nm layer was recorded which remained almost the same even at the 2 nm layer. A further sample with an embedded Au layer with only 0.5 nm showed no Au signature at all.

Before the reasons for this strongly non-linear behavior are discussed in section 5.1.5, the amount of positrons, which annihilate in the embedded layer, is quantified. For this purpose, least square error fits have been applied to the recorded spectra according to the procedure presented in section 3.3.6. The fitting range was limited to the high momentum area between 513.5 keV and 525 keV to minimize the influence of conduction electrons with momenta below $10 \cdot 10^{-3} m_0 c$ and background events at electron momenta higher than $55 \cdot 10^{-3} m_0 c$.

The fitting parameter η reflects the fraction of positrons annihilating with electrons from the element of the embedded layer. If positron annihilation would only occur inside defect free layers and agglomerations of the used elements, the fit would agree with the data within the statistical error. However, defects due to the lattice mismatch and due to the grain boundaries would lead to a deviation of the measured spectrum of the layered sample from the linear combination of the pure reference spectra [67].

The resulting values for η obtained from the CDBS measurements are compared with the calculated fractions of positrons implanted in the embedded layer f and summarized in Table 5.3. For the samples no. 1, 4, 6 and 7 no minimum in the square error function for $0 < \eta < 1$ could be found. Thus, at these samples no signature of the embedded elements is observed, i.e. the embedded layer of these samples was not detectable by CDBS.

5.1.3. Complementary TEM measurements

The astonishing high sensitivity of the CDBS measurement to the 2 nm thin gold layer is explained by an efficient trapping of the positrons at the intermediate layer. Though the high trapping rate can be easily explained by positron confinement due to an attractive positron affinity difference, the positron has to move from its implantation site to the intermediate layer by thermal diffusion. To understand the diffusion process, it is necessary to know the structure of the trapping layer. For this reason, Transmission Electron Microscope (TEM) images have been taken of this particular sample. The sample was prepared by conventional FIB lift-out technique. The multi-layers are in crosscut-view,
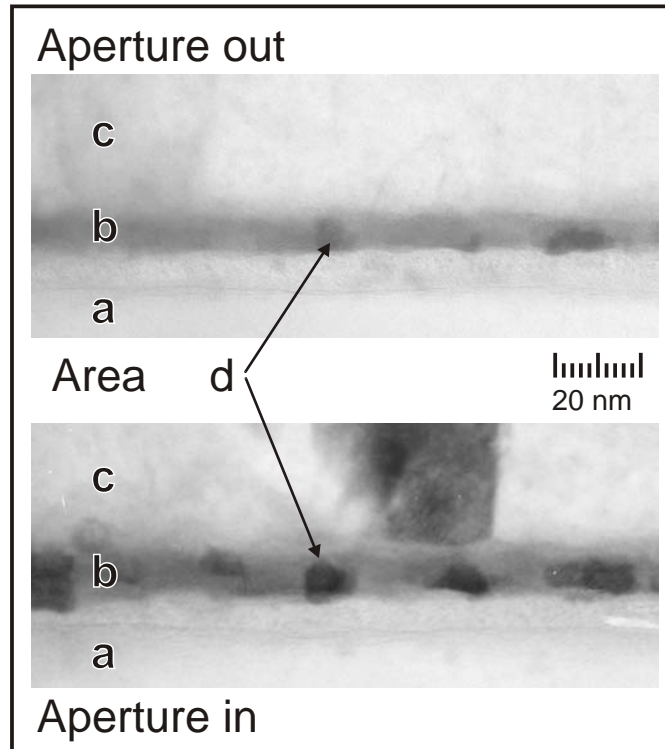
Figure 5.5.: This TEM picture shows the intermediate layer of the Al sample containing 2 nm gold [13]. Area (a) is identified as the aluminium substrate. Area (b) is the polycrystaline intermediate layer containing gold. Area (c) is the cover layer of pure aluminium. Area (d) shows clusters in the intermediate layer of Au-Al alloy with higher gold concentration. The same area of the sample is imaged with and without the objective lens aperture.
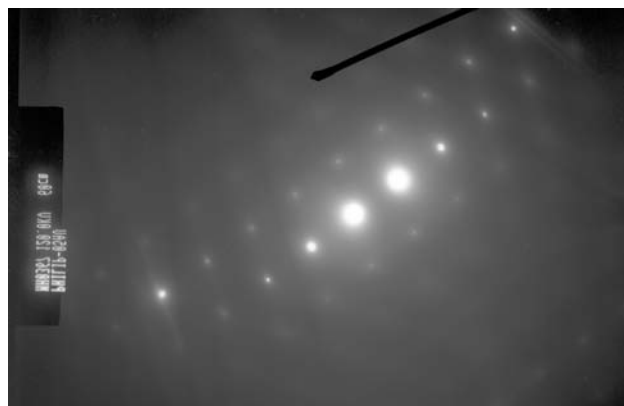

Figure 5.6.: This TEM picture shows the diffraction pattern of the Al substrate of the 2nm gold sample.

and they are parallel to the edge of the wedge-shaped TEM specimen. The FIB machine and the TEM of Tohoku University at the IMR Oarai, Japan have been used.

Figure 5.5 shows the essential results of the TEM. The upper image was obtained with no objective lens aperture. The gray-scale contrast in the upper image originates from inelastic scattering primarily dependent on the atomic number and therefore provides information of local chemical composition. Heavier elements exhibit darker contrast. The Aperture out-image indicates that areas (a) and (c) consist of lighter elements, i.e. aluminium in this case, and the area (b) contains gold, respectively. The area (b) exhibits non-uniform contrast, indicating compositional fragmentation within the layer. The dark portions are most likely gold precipitates (area (d))embedded in a gold-aluminium alloy matrix. The average thickness of the alloy is 9 ± 1.5 nm. Because the amount of deposited gold is known from the sample preparation process, the gold concentration in the intermediate layer can be calculated. It amounts to 66 ± 11 mass percent according to 22 ± 3.7 atomic percent.

The lower TEM picture ("Aperture in") is a bright-field images that visualizes grains and their boundaries. The substrate shows no grain boundaries at all due to a grain size which is much larger than the field of view. In relation to positron diffusion lengths the substrate is quasi monocrystalline, which is confirmed by stable diffraction patterns (Figure 5.6). The intermediate layer (area (b)) is polycrystalline due to grain boundaries visible very next to the area (d) clusters. The cover layer is polycrystalline with a typical grain size larger than 100nm. This grain size is in the same order of magnitude than positron diffusion length, so that diffusion along grain boundaries must not be neglected.

In conclusion of the TEM results the layered aluminium gold sample has optimal characteristics for effective positron trapping at the buried layer: The aluminium grains are big enough to enable long positron diffusion lengths. In addition, the accordance of the lattice constants, i.e. the negligible lattice mismatch of gold and aluminium minimizes the concentration of open volume defects at the interface.

5.1.4. Monte Carlo simulations of thermal positron diffusion

One of the TEM results is the presence of a continuous layer of up to $22\%_{at.}$ gold content. According to the CDBS results this aluminium gold alloy is apparently able to trap the thermally diffusing positron. In order to explain the efficient positron trapping no detrapping is considered. Monte Carlo simulations can provide an upper limit for the trapping rate at the intermediate layer by the simulation of a three dimensional random walk which represents the thermal positron diffusion at an atomic scale [65]. For trapping at planar layers not the mean diffusion length according to Fick's law and the Einstein-Smoluchowski-relation is directly relevant [68], but it is necessary to know the probability for a positron which is implanted in the depth z to once reach a layer in depth d during
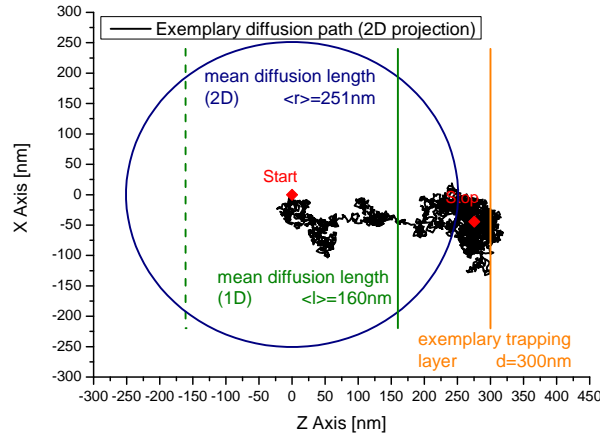
Figure 5.7.: An exemplary three dimensional random walk projected to two dimensions. A comparatively small mean diffusion length in 1D-projection (162nm) corresponds to a $\approx \frac{\pi}{2}$ longer diffusion length in two dimensions (circle). In this exemplary path the particle reaches the trapping layer at a distance $d = 300\,\text{nm}$ to the implantation site.

the diffusion process. Figure 5.7 demonstrates that during the random walk a layer can be reached which is more distant to the implantation depth than the end-point of the free diffusion.

For this study, the influence of positron trapping at the surface or in vacancies is not implemented in the random walk simulation. The necessary parameters $\bar{l}$, the mean free path of the positron and N, the number of scatterings can be calculated from the diffusion law [68]. The lifetime of the positron in an aluminium crystal is $\tau = 161 \pm 2\text{ps}$ [29] and the diffusion length is $L_+ = 160 \pm 15\text{nm}$ [30]. The mean velocitiy of the thermalized positron is $\bar{v} = \sqrt{\frac{8k_BT}{\pi m}}$ and the average free path $\bar{l} = \frac{3D_+}{\sqrt{\frac{3k_BT}{m}}}$ with a diffusion coefficient $D_+ = 1.7\frac{\text{cm}^2}{\text{s}}$ [30]. Room temperature $T = 300\text{K}$ is assumed for all calculations. As a result, the mean free path of the positron is $\bar{l} = 4.37\text{nm}$ and the mean number of scatterings until annihilation is $N = 3964$.

Figure 5.8 shows the results of the Monte Carlo simulation and their relevance to the measurement of the 2nm gold layer. From top to bottom, the graphs contain: (a) The implantation profile $I(z)$ of the 6 keV positron beam according to the modified Makhovian function (see section 2). (b) The result of the Monte-Carlo simulation which shows the probability $p(z)$ of a positron which is implanted in a depth z to reach an intermediate layer at $z = 200\,\text{nm}$. (c) The product $I(z) \cdot p(z)$ shows the part of the implanted positrons which are able to reach the intermediate layer. (d) The positron density $\rho_+(z)$ is calculated from the endpoints of the Monte-Carlo simulation. After the diffusion process, a small

ratio of the positrons remains in the aluminium of the sample. $73 \pm 3\%$ of the implanted positrons are trapped in the intermediate layer.
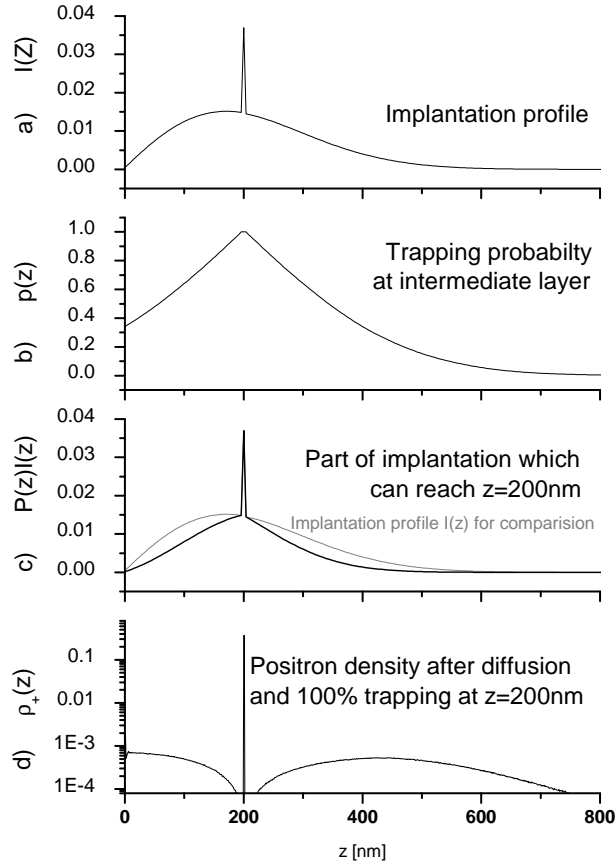

Figure 5.8.: Sample (2): Positron implantation profile (a), diffusion probabilities (b and c) and the resulting positron density after diffusion (d).

The measured value $\eta = 82\%$ of positron annihilation near gold atoms is slightly higher than the calculated maximum trapping ratio of $73 \pm 3\%$ although diffusion limiting effects like vacancy or surface trapping are neglected. This deviation can be explained by several reasons: First, the grain boundaries in the covering layer may be contaminated with gold atoms. Vacancies in aluminium are fully mobile at room temperature and, assuming that in the production process vacancies migrated from the intermediate layer to the surface, gold atoms may have diffused into the covering layer as well. Secondly, the Monte-Carlo simulation used isotropic diffusion all over the specimen. But the TEM mesurements clearly showed grain boundaries in the covering layer which are mainly perpendicular to the gold layer and hence could have caused a more directed positron diffusion to the intermediate layer.

5.1.5. Discussion and conclusion

Positrons in layers

The presented results show a highly non-linear correlation between the positron affinities, the thickness of the embedded layers and the element dependent photon intensities in the high-momentum region of the annihilation line. For the discussion of the results, several aspects have to be considered which influence the shape and the intensity of the CDB spectra. After implantation, thermalized positrons diffuse through the lattice with a diffusion length in the defect free Al of typically 160 nm [30] . Dependent on the concentration on trapping sites such as vacancy-like defects, the diffusion length can be reduced considerably. Both processes play a major role, trapping in open-volume defects and the attraction or repulsion at interfaces due to the element dependent positron affinities.

Positrons diffusing to the layer's interface are trapped if open-volume defects are present. The number of those defects is expected to be large if the lattice mismatch at the interface is high (see Table 5.2). For positrons trapped in open-volume defects the smaller core annihilation probability would lead to a lower photon intensity in the high electron momentum region than annihilation in the unperturbed lattice. The result of positron annihilation at grain boundaries, which become more important if the grain size is smaller than the positron diffusion length, would be similar. On the other hand, due to the higher positron mobility at the grains' surface the probability to reach the layer-matrix interface would increase which becomes more important if the grain size is in the order of the layer thickness.

The positron affinities A^+ of the materials have to be considered in particular if its difference ΔA^+ is higher than the thermal energy of the positron. For example, an attractive (repulsive) potential barrier is formed at the Al-Au (Al-Cr) interface which attracts (repels) positrons diffusing from the Al matrix to the Au (Cr) layer. In addition, small clusters of a material with strong positron affinity would form positron trapping sites.

Defect trapping

For all samples with the thinnest embedded layer –10 nm at Cr and Cu as well as only 0.5 nm of Au– a very similar shape and a lower intensity in the high-momentum region is observed (see Figure 5.4). This effect is due to the presence of open-volume defects which lead to a reduced core annihilation probability for trapped positrons. For instance, due to the missing repulsive core potential, a single vacancy in Al forms a potential well for positrons of about 1 eV depth [4].

Even at the thickest Cr layer embedded in Al (Figure 5.4a), although the Cr signature is very pronounced (see reference in Figures 5.3) Cr is not visible and the Cr signature could not be fitted reliably. In this case, trapping in vacancy-like defects in Al and Cr plays a

major role, since the concentration of open-volume defects is expected to be particularly high due to the large lattice mismatch of -28 % (see Table 5.2). Moreover, due to the high $\Delta A^+ = +1.58\,\text{eV}$ of Cr in Al the Cr-Al interface forms a repulsive potential. For this reason, the diffusion of thermalized positrons from Al into the Cr layer is inhibited and positrons implanted in the Cr layer diffuse into the Al matrix, which is energetically more favorable. Consequently, due to both, vacancy-like defects near the Cr-Al interface as well as the repulsive potential formed by the Cr layer the Cr signature becomes not visible in the CDB spectra.

The 100 nm Cu layer in Al (sample no. 5) leads to a measured fraction of positrons annihilating in Cu of η=88 % which is higher than the fraction of implanted positrons in the Cu layer (f=56.1 %). This effect cannot be explained only by open-volume defects related to the lattice mismatch (Δa=-10.8 %). Although positron detrapping is expected at room temperature due to the shallow potential formed by the Cu layer of $\Delta A^+ = -0.06\,\text{eV}$, positrons implanted in Cu would barely diffuse into Al. Accordingly, positrons implanted in Al, which reach the Al-Cu interface would rather annihilate with electrons from Cu than from Al.

In sample no. 3, the 100 nm Au layer is clearly visible in the CDB spectrum (Figure 5.4 A1) due to the high positron affinity of Au embedded in Al ($\Delta A^+ = -1.82\,eV$). The fitting parameter $\eta = 0.92$, which corresponds to the positron fraction annihilating in Au, is considerably higher than the implantation ratio $f = 62\%$. This is a clear indication that positrons diffuse from the Al matrix into the embedded Au layer. In addition, this diffusion process is not hindered by lattice mismatch induced defects since the amount of those is expected to be negligible due to the very similar lattice constants of Au and Al (see Table 5.2).

Quantum confinement

The most astonishing result was obtained for the sample no.(2) with a 2 nm Au layer embedded in Al. At this sample the Au signature is almost as strong as in the spectrum of the sample with the buried 100 nm Au layer (no. 3), although at 0.5 nm Au in Al no Au signature was detected at all. The accordingly very small amount of positrons implanted in the 2 nm Au layer of $f = 2.4\%$ leads to a huge fraction of positrons annihilating in Au of $\eta = 83\%$.

This strong effect can be only explained by very efficient positron trapping into the energetically more favorable Au layer. The results of the Monte-Carlo simulation (section 5.1.4) support that the Al-Au alloy layer, which was analyzed by TEM (section 5.1.3), confines the positron diffusion into the 2-dimensional alloy layer. A stable positron trapping only in the clusters of high gold concentration but not in the alloy layer (see figure 5.5) could not sufficiently explain the high trapping rate. The low momentum part of the

CDB spectrum shows significant deviations from the gold reference. Studies conducted on copper clusters in iron [67] demonstrate that these deviations can be caused by the positron localization in pure bulk material, in small clusters or in alloys. Hence the low momentum deviation indicates that annihilation occurs in the alloy or in small clusters.

The high difference of the positron affinity of $\Delta A^+ = -1.82\,\mathrm{eV}$ for this material combination leads to the formation of an attractive potential for positrons. Therefore, thermalized positrons inside the Au layer or in Au clusters are repelled at the Au/Al interface, and positrons diffusing from Al to the Au layer are efficiently trapped inside the Au layer or Au clusters which have been observed by TEM. As shown in Section 5.1.1 the positron wave function will be confined inside an Au cluster with a minimum size, i.e. the well needs a certain extension in order to possess at least one bound positron state. Assuming a spherical Au cluster with $\Delta A^+ = -1.82\,\mathrm{eV}$ its critical radius r_c is calculated to $r_c \cong 0.23\,\mathrm{nm}$. Thus, $0.46\,\mathrm{nm}$ is the minimum extension of the Au cluster to form a bound positron state. By comparison with the lattice constant of Au (a$=0.408\,\mathrm{nm}$) the clusters would be at least of the size of a unit cell and hence contain at least 14 Au atoms. Such clusters (see figure 5.5) hence lead to a three dimensional quantum confinement of the positron wave function. Moreover the Al-Au alloy formed in the Al matrix first acts as a confinement of the positron diffusion and hence the gold rich clusters with a mean distance of typically $20\,\mathrm{nm}$ are reached in the subsequent 2-dimensional diffusion process with very high probability. CDBS data can not finally distinguish if the annihilation occurs in the layer of lower Au concentration or in the clusters of high Au concentration.

For the same reason, no positron trapping sites are formed by Au at the sample (no. 1) containing $0.5\,\mathrm{nm}$ Au where no Au signature was observed at all. Consequently, the evaporated Au layer of only $0.5\,\mathrm{nm}$ thickness is expected to form a Au-Al alloy with lower Au amount than the $2\,\mathrm{nm}$ Au layer which does not trap positrons. In addition, the maximum radius of possibly formed Au clusters in this layer is smaller than $0.23\,\mathrm{nm}$ which do not lead to the confinement of the positron wave function. Hence positrons get trapped at vacancies and consequently the CDB spectrum looks similar like the spectra obtained for thin copper or chrome layers.

5.1.6. Conclusion

A series of CDBS measurements were performed on samples with embedded layers of different positron affinities (Cr, Cu and Au in Al) and various thickness. This systematic investigation using a monoenergetic positron beam revealed a strong non-linearity in the response of the CDBS measurements due to the variation of the layer thickness with different elements which was attributed to two main effects. Firstly, vacancy-like defects lead to positron trapping at the layer-matrix interface particularly if the lattice mismatch is high. Secondly, due the difference of the element dependent positron affinity

a potential step is formed at the interface that enhances the positron annihilation with electrons of the elements with higher positron affinity. Moreover, the huge difference of the results obtained for the 0.5 nm and the 2 nm Au layers embedded in Al demonstrates the extremely high sensitivity to small variations of the elemental concentration in the sample. The theoretically calculated positron affinity was proofed to be a profound basis for the understanding of a quantum confinement based model of the positron trapping in Au clusters with a minimum diameter of 0.46 nm surrounded by Al [13].

5.2. Temperature dependent measurements

As it is shown in the previous section, CDBS is well suited to study the size of metallic agglomerations. Due to its non-destructiveness CDBS is predestined for in-situ measurements of time dependent processes like diffusion or cluster growth at increased temperatures. In conventional techniques, it is hardly possible to measure the growth or solution of low-concentration precipitates without destructive sample preparation.

With appropriate material combinations, which can be determined by positron affinities A^+, CDBS allows to measure in-situ positron trapping in agglomerations which are created or dissolved during thermal treatment. In that case it is relevant to measure in the shortest possible time intervals, so that the application of a high-intense positron source is obligatory. To gather experiences with this new experimental technique, temperature dependent CDBS measurements of agglomeration changes in a layered system have been performed.

Agglomeration growth and solution

The heating of a binary metallic mixture can initiate structural changes until a state of thermodynamical equilibrium is reached. If the sample consists of a metastable alloy, which is energetically unfavorable to a heterogeneous mixture of different phases, precipitate growth can be the consequence. Alternatively, if a heterogeneous structure is heated which tends to form an alloy, clusters dissipate.

5.2.1. Samples

To study the structural changes, layered samples consisting of aluminium with an embedded gold layer are produced and heat treated during CDBS measurements. The combination of these materials is chosen according to the results of section 5.1. First a set of samples with 2 nm, 5 nm and 10 nm gold layers embedded under 100 nm aluminium was produced by physical vapor deposition (PVD). CDB spectra indicated, that the 2 nm and 5 nm thick embedded layers can not be detected. This can be explained by the higher substrate temperature during the PVD process, compared to the sputtering process which

was used for the samples in section 5.1. The higher substrate temperature strongly increases the diffusion of the gold atoms into the aluminium during the deposition process, so that more gold is needed to form agglomerations of sufficient gold concentration. A 10 nm thick embedded gold layer leads to a visible gold signature which is shown in figure 5.10.
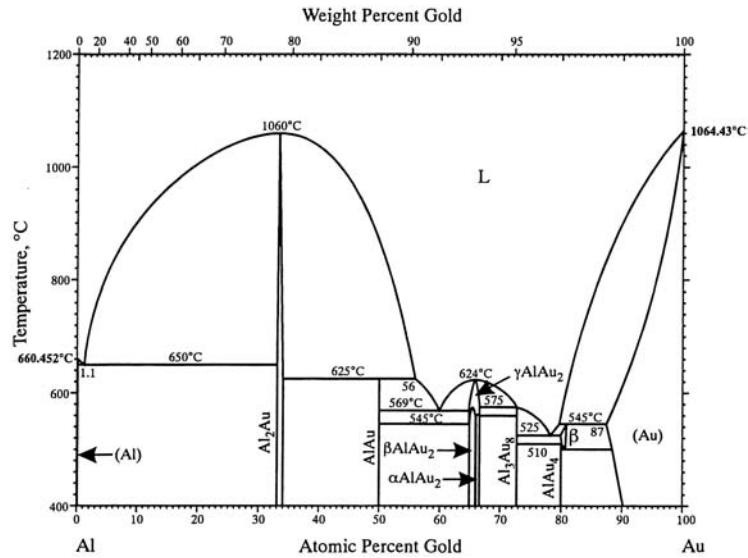

Figure 5.9.: The phase diagram of AlAu. Figure from [69].

The phase diagram in figure 5.9 shows that low concentrations of gold are stable in the Al_2Au compositions. In section 5.1 it was shown that these amounts of gold are able to delimit the positron diffusion, but not to generate a gold signature in the CDB spectrum. Hence in the prepared sample, clusters or a layer of higher gold concentration must be present, so that a gold signature is visible at 2 keV (figure 5.10). The CDBS measurement will show if the concurring processes of defect annealing and gold diffusion lead to a growth of AlAu clusters, which are expected to show a distinct gold signature, or if the layer of high gold concentration is diluted by diffusion processes so that the gold signature vanishes.

5.2.2. Experimental results and discussion

The sample with the embedded gold layer of 10 nm thickness in its "as prepared" state was measured with a set of different beam energies. The measurement at 1 keV shows mainly the surface of the sample due to the according mean implantation depth of < 10 nm. Figure 5.10 shows the results as ratio to the samples substrate reference curve exemplarily for 1, 2 and 6 keV. At energies from 2-4 keV a gold signature could be detected. An agglomeration growth is expected to increase the gold signature significantly, as in the previous section
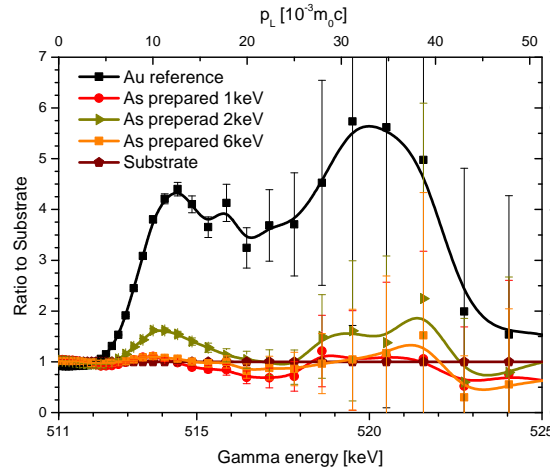
Figure 5.10.: The CDBS spectra at different implantation energies before tempering (as prepared).

was shown that gold clusters can effectively trap positrons and cause a distinct signature. A further dissolving of the gold layer in the aluminium will decrease the signature because gold-aluminium phases with low gold amount carry the CDB signature of pure aluminium.

In figure 5.12 linear combination fits of the substrate material and the gold reference have been applied to all 13 measured energies. This produces depth profiles of the sample, with the amount of positrons which can be trapped at gold plotted over the implantation energy. Once more it can be concluded, that the maximum gold amount is in the depth of the 2 keV positron implantation in the "as-prepared" state. After heating for 120 min at 430 °C the maximum gold amount was detected at the samples surface. Further, there seems to be high AlAu amount in the bulk of the sample.

A further investigation of the measured spectra (figure 5.13) confirms only the high gold amount at the surface, which could also be seen by eye, because during the thermal treatment the samples surface turned into violet, which is the colour of AlAu (see figure 5.11). For higher positron beam energies, the high momentum part of the CDB spectrum rises, but not characteristically in the shape of elemental gold. Obviously, the thermal treatment of the sample lowered the amount of vacancies in the bulk of the sample. This increased the high momentum part of the aluminium spectrum, so that the linear combination fitter could not find a valid fit using the spectra of the reference materials. In conclusion, after the heat treatment, the gold is only trapping positrons at the sample surface. In the bulk of the sample, an alloy of gold and aluminium has formed, which does not trap positrons and hence generates no visible signature in the CDB spectrum.
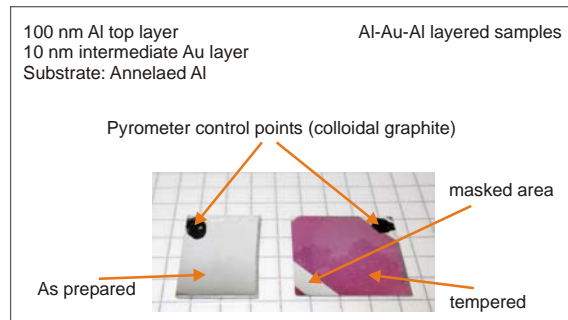
Figure 5.11.: This photograph shows the aluminium gold aluminium sample in its "as-prepared" and "tempered" state. The as-prepared state shows simply a uniform aluminium surface, while after tempering the surface color turned violet, except for the areas which were masked during evaporation. The black points on the samples are obligatory for reliable temperature measurement by the pyrometer.

5.2.3. Conclusion

The comparison of the CDB spectra before and after heat treatment indicates: First, the gold signature at 2keV clearly diminishes after heat treatment. This behavior can only be explained by a dissolving of the layer into the surrounding aluminium, which is in accordance to the formation of most likely Al_2Au. Second, the gold signature at the surface increased strongly while the signature in the samples bulk decreased, which indicates a diffusion of gold atoms to the surface.
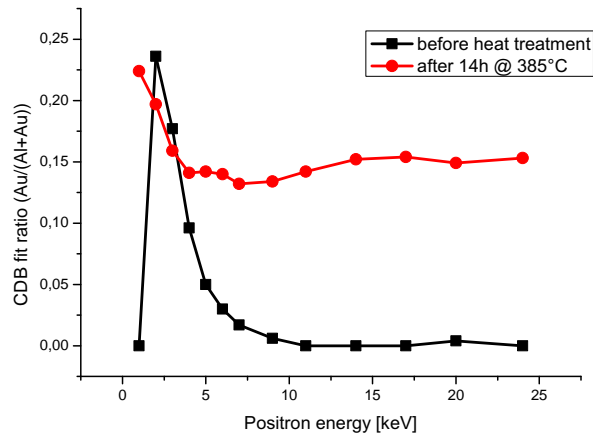
Figure 5.12.: The diffusion of gold into aluminium after a heating process measured by energy dependent CDBS.
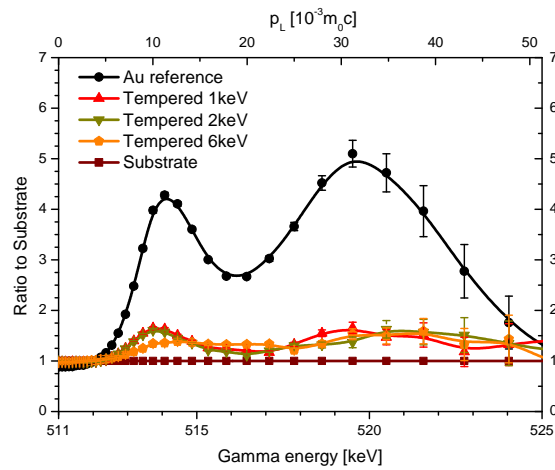
Figure 5.13.: The CDBS spectra at different implantation energies after tempering for 120min at 430 °C. Due to higher statistics compared to the "as-prepared" measurement the error bars are smaller.

6. Case study on ionic liquids

Temperature dependent measurements are of high interest for the investigation of phase transitions. The investigation of the transition from the liquid to solid phase or vice versa with positrons is well suited for fundamental studies of positron trapping in these both states. The experimental difficulty for these investigations is that the vapor pressure of the vast majority of liquids is considerably too large to sustain appropriate vacuum conditions for a positron beam. In contrast, ionic liquids can be measured in UHV conditions over a very wide temperature range. Unlike water (see section 4.1) ionic liquids have a negligible vapor pressure, so no attention has to be paid to the vacuum conditions even at room temperature. This enables the measurements of the liquid phase with the monoenergetic beam, as well as the measurement of different phases by variation of the sample temperature.

Furthermore, depth dependent measurements are of special interest when they are performed on liquids. Obviously, the liquid has a homogeneous structure in its bulk, but the near order structure can be influenced by different surface effects. Positrons in their delocalized state can survey a volume of many molecules there, and detect the presence of voids [70]. The measurement of both aspects, the phase transitions as well as the near-surface-structure, are exemplified in this chapter.

6.1. General properties

6.2. The ionic liquid BMIm-PF6

Ionic liquids consist basically only of weakly coordinated ions. The low degree of coordination can be achieved by choosing at least one organic ion of big size and low symmetry,

Property	Value	Unit
Melting Point	283.51	K
Glass transition temperature	190.6	K
Density (300 K)	1.36	$\frac{g}{cm^3}$
Vapour pressure	$< 1 \cdot 10^{-6}$	mbar

Table 6.1.: Basic properties of BMIm-PF6.
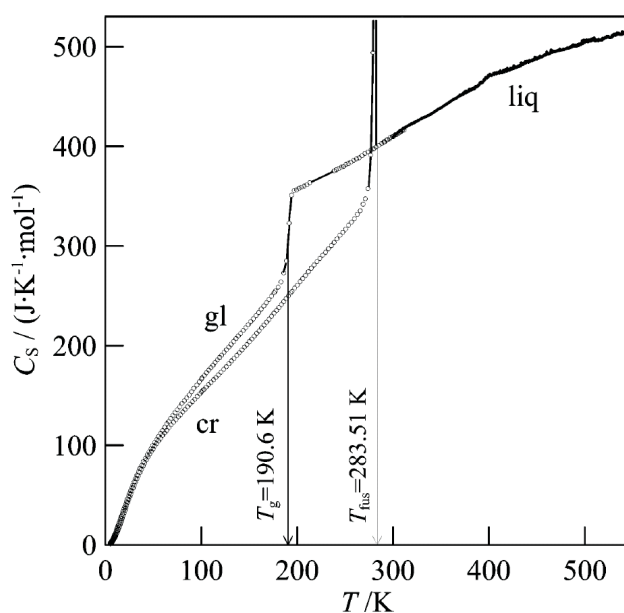
Figure 6.1.: Heat capacity of BMIm-PF6 in the crystalline, glassy,and liquid states. T_g is the glass transition temperature, and T_{fus} is the triple-point temperature. Figure from [71]

which inhibits the creation of a stable lattice at room temperature. So the chemical compound is an organic salt with a remarkable low melting point – for various species – even below room temperature. There is much data available about ionic liquids because of high interest of the chemical industry in this new class of substances. They are very good solutants for hardly dissolvable materials (e.g. cellulose) and they can be more environment-friendly than the commonly used high volatile substances.

For this study, 1-Butyl-3-methylimidazolium hexafluorophosphate (BMIm-PF6) is chosen. Its characteristics are shown in table 6.1. Highly important for this measurement is the low vapor pressure which could be confirmed in the spectrometers vacuum chamber and the low melting point of 283.5 K. The ionic liquid is contained in a copper crucible of 10 mm diameter, so the positron beam can easily be focused on the surface of the liquid.

6.3. Energy dependent measurements

The use of a monoenergetic positron beam enables depth profiling of the near surface structure of the liquid. Figure 6.2 shows the S-parameter measurement of the ionic liquid as function of implantation energy. This measurement shows a low amplitude of the S-parameter over the whole energy range. A significant effect in the S-parameter can be measured at the surface. To gain more information about the structure below the surface,
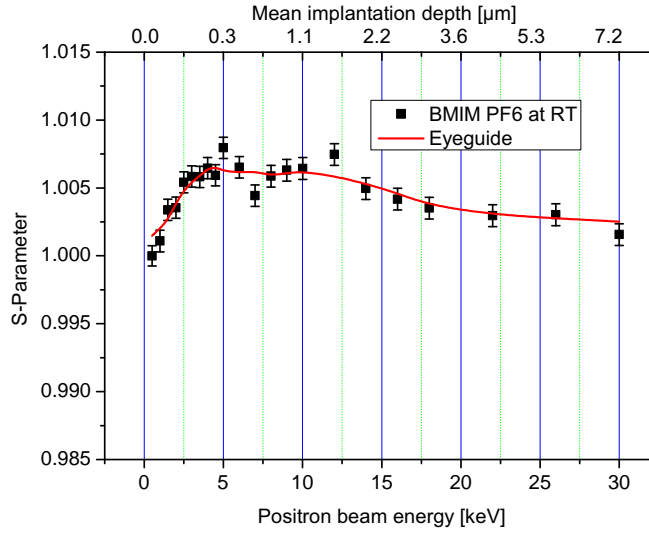
Figure 6.2.: The use of a monoenergetic positron beam allows to vary the mean implantation depth below the surface of the ionic liquid. The amplitude of this measurement is low ($< 1\,\%$).

the formation of positronium was studied by analyzing the data with regard to the PTV-ratio.

6.4. Peak-to-valley measurement

Free positrons in matter usually decay into two γ-quanta of $511\,\mathrm{keV}$. The decay into three γ-quanta is highly suppressed. This ratio changes, when a positron binds with an electron to ortho-positronium at surfaces or voids. As a result, the decay into three γ-photons with a continuous energy distribution gets visible in the full spectra of the HPGe-Detectors. This effect can be revealed by the calculation of the ratio of the integrated counts in the 511keV-photo peak to the counts in the valley between the Compton-edge and the photo peak of the 511keV-photons, the "Peak to Valley (PTV)"-ratio as described in section 2.3.3. If ortho-positronium decays, its continuous spectrum is counted in this energy range and the PTV-value decreases.

In the PTV-measurement of this study (figure 6.3) a clear change in positronium formation over the energy range is visible. As expected, positronium formation is evident at the surface, and - to a lower extent - in the bulk of the liquid where the PTV-value saturates below $\approx 1\,\mu\mathrm{m}$. This surprising observation can be explained by structural voids in the liquid, where positronium formation is possible. The higher PTV-value in the surface
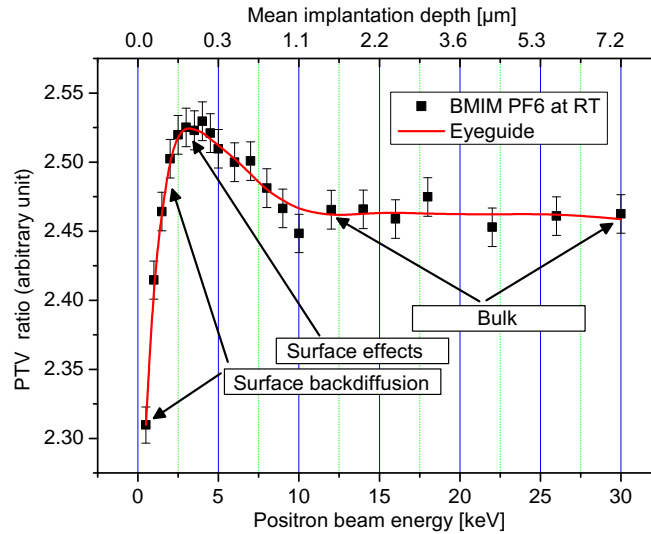
Figure 6.3.: The formation of positronium is measured by the Peak-To-Valley (PTV) Ratio. A high PTV-ratio corresponds to low positronium fraction.

region shows that there are less or smaller voids. This is in agreement with a crystalline layer at the surface as reported in [72], with a reported depth of several nanometers [73]. The higher PTV-value at implantation depths up to $1\,\mu$m may be explained by the non-discrete implantation profile (see section 2.2.1) or by the currently non determined positron diffusion processes in liquids.

6.5. Temperature dependent measurements

For the temperature dependent measurements the cryostat assembly is used, which is described in detail in [38]. It allows Doppler broadening spectroscopy in a sample temperature range from $\approx 100\,$K to room temperature. The energy of the positron beam was set to 15 keV to ensure complete implantation into the bulk.

Figure 6.1 shows the heat capacity of BMIm-PF6 in its three main phases. The substance is liquid above 283.5 K and below this temperature it has a crystalline and an amorphous state [71]. To reach the amorphous state, the sample was cooled rapidly to 100 K, which is sufficiently below the glass transition temperature of 190.6 K. During the cooling the S-parameter was monitored, and a continuous increase from 0.505 to 0.52 was observed (not shown). Then the S-parameter was measured in an interval of 90 s while the sample was heated with an average heating rate of $0.3\frac{\text{K}}{\text{min}}$. As shown in figure 6.4 there occur three sharp gradients in the S-parameter while the sample heats up. All these sharp gradients
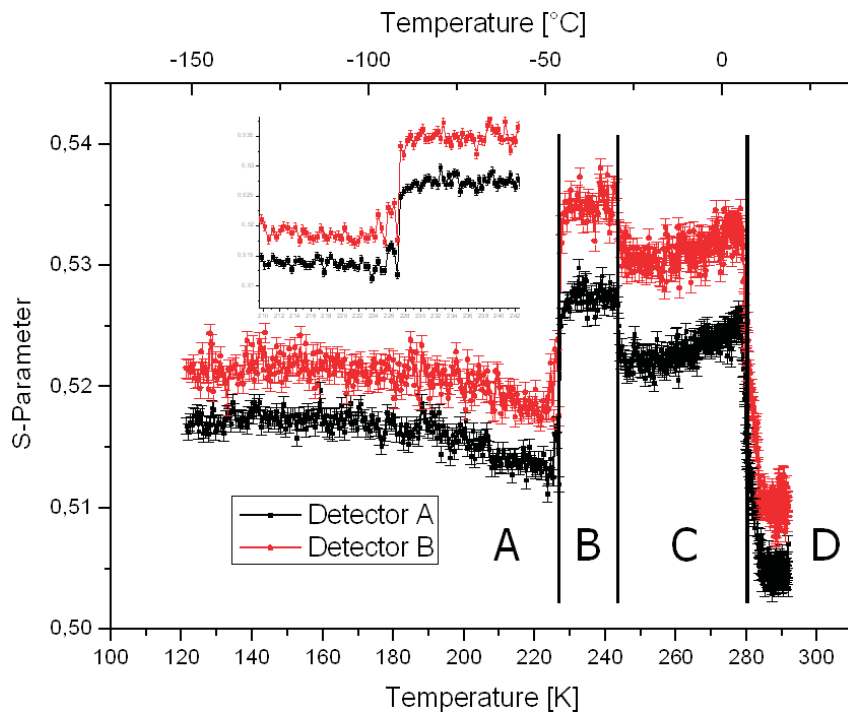
Figure 6.4.: The S-parameter changes several times rapidly while the sample is heated from its amorphous state until melting. This is explained by different phase transitions. The calculation of the S-parameter can be performed with the data of a single detector. Hence the s-parameters gathered by a pair of collinear detectors A and B are plotted to show the accuracy of acquisition.

are caused by phase transitions. Initial phase A is the amorphous state. Shortly above the glass transition temperature T_g the material crystallizes into phase B which causes a very sharp increase in the S-parameter (see insert of the graph). Phase B then changes into phase C which is crystalline too, but has an other structure. Finally, at 281 K, the material melts and the S-parameter decreases again to the value obtained for the liquid. The comparison with first results of the neutron diffractometer TOFTOF confirms the transition temperatures as well as recent studies performed with Raman spectroscopy [74].

6.6. Conclusion

The non-destructiveness of positron measurements made it feasible to study the surface structure of an ionic liquid. In particular, it is demonstrated to to determine the depth, where influences of the surface on void concentration gets negligible. This is done by peak-to-valley measurements, while phase changes between amorphous and different crystalline states could be revealed with high sensitivity by Doppler broadening.

7. Conclusion & Outlook

In this work the positron trapping in ultra-thin metallic layers and at metallic precipitates was investigates systematically with CDBS. The sensitivity of this technique was determined dependent on the nominal thickness of the embedded layer and dependent of the positron affinity with regard to the substrate. For this purpose, layered metallic samples were produced with a well defined composition of aluminium and embedded layer of chrome, copper or gold. The chosen materials cover a wide range of positron affinities, and the embedded layers have been produced in a well defined set of thicknesses.

Embedded layers of chrome with a thickness of 2 nm, 10 nm or 100 nm caused no positron trapping due to their repulsive positron affinity in combination with aluminium. In these samples, only the vacancy like defects at the interface, caused by the lattice mismatch of chrome and aluminium could be observed. In copper layers, with a negligible positron affinity difference to the aluminium substrate, the layer of 100 nm thickness could be clearly detected by CDBS due to the targeted positron implantation into the embedded layer. The thin layers of copper ($d \leq 10$ nm) could not be detected, because the lattice mismatch induced defects dominated the measurement result. CDBS detects, as expected, the gold layer of 100 nm thickness due to the targeted positron implantation and the attractive positron potential at the gold-aluminium interface. The most astonishing result was observed with a gold layer with a nominal thickness of only 2 nm. In this sample a gold signature was observed with nearly the same intensity in the CDB spectrum as it was obtained with the gold layer of 100 nm thickness. This is explained by the efficient trapping of the positrons in gold clusters after nearby implantation and positron diffusion. In this case an astonishing high amount of 83 % of the positrons annihilates in gold clusters, although only a minor amount of 2.4 % is directly implanted there. This diffusion and trapping process could be theoretically described by a three dimensional random walk model. The obtained simulation results were in excellent agreement with the experiment. In addition, the structure of the clusters in the layered sample was also confirmed by complementary TEM images. Furthermore a gold layer of a nominal thickness of 0.5 nm was analyzed with CDBS. This amount of gold turned out to be too small to form agglomerations of the critical size for positron trapping, which was calculated by a quantum well model. For this reason, no gold signature in the CDB spectrum was obtained for this specimen. Consequently a very distinct size effect of the CDBS sensitivity to positron attracting agglomerations was experimentally confirmed.

The combination of the high intense monoenergetic positron beam at NEPOMUC and the CDB spectrometer consisting of up to eight HPGe detectors allows a uniquely short acquisition time of only one hour per CDB spectrum. A novel data evaluation algorithm was developed which lead to an increase of the signal to noise ratio of up to one order of magnitude. Hence both depth-scans over a wide range of positron energies and time dependent measurements at high temperatures became feasible during single day measurements. This entails one very interesting applications like the demonstrated strong size effect of embedded metallic clusters. It was shown that the solution of gold agglomerations in aluminium at high temperatures as well as the diffusion of gold atoms from the embedded layer to the sample surface could be analyzed non-destructively and in-situ.

CDBS has shown to be predestined for the detection of lowest concentrations of precipitates. This technique is non-destructive and it can distinguish between material components in homogeneous solution and in heterogeneous phases with precipitates. By the utilization of layered model systems and complementary imaging methods the conditions for positron trapping can be measured and therefore a quantitative evaluation of the CDBS results in alloys gets feasible. In particular, the application of CDBS in-situ allows to observe the time- and temperature dependence of the early stages of precipitate growth.

Within the scope of this work the analysis of embedded agglomerations was demonstrated with various layered metallic samples, and the experimental equipment and technique for fast in-situ CDBS measurements was established.

This technique is of highest interest for the characterization of age hardening alloys [75]. They are of high value for industrial applications because they combine good machining properties with a high elasticity after hardening. A homogeneous mixture of the alloy components is highly ductile and can be cold-formed to the desired shape. By a rapid heating process, precipitation in the material starts and the growth of the precipitates changes the mechanic properties to the desired type of a more brittle, hard and elastic substance. For further development of these alloys, it is crucial to study the early stages of the precipitate growth. In future measurements, the precipitate growth of Cu-Mg clusters in widely used Al-Mg-Cu alloys is to be studied and compared with layered model systems. This way, not only the formation of Cu-Mg clusters can be detected in an early stage, but also exact quantitative values about the correlation of chemical composition, hardening temperatures and precipitate sizes are to be obtained.

Last but not least the CDB spectrometer at NEPOMUC could be utilized for several successful studies of external users. E.g. B. Oberdorfer could investigate fast defect-annealing in ultra-fine grained materials [76]. Vacancy defects in thin perovskite oxides were identified by D.J. Keeble [77] and domain growth in ternary iron-alloys could be characterized by R. Gilles [78]. In future NEPOMUC will provide CDBS measurements for many further research projects.

A. Appendix - Technical aspects of 2D evaluation

In the section 3.3 the method of the new CDB projection algorithm is explained. In this part, further details of the programming realization are explained.

A.1. 2D preparations

The results of two dimensional data acquisition are 32-bit integer matrices of 1024×1024. The new spectrometer can be operated with up to 8 HPGe-detectors which produce up to four matrices per measurement. The unrivaled short time of one hour for the acquisition of usable CDB count rates enables the recording of up to 96 CDB measurements in one four day beam time, which equals up to 384 single spectra. It is desirable to keep the processing time of the CDB spectra as low as possible, to allow convenient evaluation of this amount of data and to allow the user the examination of different data evaluation settings.

For this reason, the evaluation program does not use floating point operations on the two dimensional data. The projection of ROIs perpendicular to the Doppler broadening area (see figure 3.18) is performed by directly reading the integer matrices.

Each element of one matrix contains the recorded events with energies E_x and E_y of one detector pair. Each detector is calibrated by a reference source. When c_x and c_y are the calibration constants in $\frac{eV}{channel}$ and C_x and C_y are the respective offsets, then one element (x, y) of the matrix stores the number of events in a rectangular energy window:

$$(x - \frac{1}{2}) * c_x + C_x < E_x \leq (x + \frac{1}{2}) * c_x + C_x \tag{A.1}$$

$$(y - \frac{1}{2}) * c_y + C_y < E_y \leq (y + \frac{1}{2}) * c_y + C_y \tag{A.2}$$

The Gauss fitting algorithm of the new evaluation program is based on processing diagonal ROIs in this matrices. These ROIs have to be placed in a way, that their projection generates a function $I_{\Delta E}(\hat{E})$ where ΔE is a specific Doppler shift which is constant in the cutting area, and $\hat{E}$ is the variable which represents one sum energy of both detectors in the spectrum.

$\hat{E}$ and ΔE non-ambiguously define one coordinate in the raw data matrix. Hence the easiest way of projection would be a nearest neighbor method. I.e. the element, which is nearest to the parameters $\hat{E}$ and ΔE defines the output value of $I_{\Delta E}(\hat{E})$. Albeit its simplicity, this method has two strong disadvantages. Firstly it is prone to moire because every transgression from one matrix element to the neighbor element involves a discontinuity in the output function. Especially for calculation of ratio curves from matrices with slightly different energy calibration, these discontinuities may generate artifacts. Secondly the energy resolution of the HpGe detectors is much wider than the usual element size of e.g. $\approx 55 \frac{\text{eV}}{\text{channel}}$. This means, the nearest neighbor only contains a small fraction of the *gamma*-events in its small energy window. For these reasons, a circular data collection with bilinear interpolation is used:

A.2. Circular collection

The bin size of the data acquisition array has to be significantly smaller than the detectors resolution to prevent data loss through aliasing. This facilitates the analysis of spectral shapes but reduces the number of counts in one bin and hence increases the statistical error in one single bin. The statistical error can be reduced by joining several bins for data collection. Obviously, bins have to be joined, in which the detector systems resolution function strays the events. In the case of a Gauss-shaped instrument function, the 2-dimensional instrument function respectively is a 2-dimensional Gaussian, which means the significance levels for data collection are circular. For this reason, circular sets of bins are joined by the data collection algorithm to calculate the projection function. The significance level, and therewith the radius of the collection circle, is variable to enable collection with either best possible energy resolution or with lowest possible statistical error. Large collection circle sizes obviosly decrease the resolution of the projection function (see figure A.1).

The shape of the collection ROIs defines a function $C(\hat{E})$ which is convoluted to the instruments function. According to Fubini's theorem

$$\int C(\hat{E}) * I(\hat{E}) d(\hat{E}) = \int I(\hat{E}) \tag{A.3}$$

for $\int C(E) d(E) = 1$. The processing software normalizes $C(E)$ to $\int C(E) dE = 1$ so that the size and shape of the collection bins does not vary the Gauss fitting result concerning its area A.

A.3. Interpolation

With circular data collection the problem occurs, that some bins of the raw data spectrum are covered only partially by the collection circle. If these bins would be fully summed up to the projection result, edge-shaped output functions would be generated. To prevent moire effects, only bins which are completely in the collection circle, are summed up with a weighting factor of one. Bins crossing the outline are weighted by their overlapping fraction. Further not the raw count value of these bins is summed up, but a bilinear interpolation with the neighbor bins. That way, smooth projection functions are generated even if the circle size and the step size of the projection function are small compared to the bin size of the aquisition matrix.

Figure A.1 shows the effect of variable ROI size to the data collection in the two dimensional matrix. While in the center of the spectrum, where very high counting rates occur, small collection circles allow a most precise distinction of Doppler shifts, background and disturbances, in the high momentum area, large circles collect a larger number of events while they are sufficiently far away from disturbing effects like small angle Compton scattering and pile ups. This artificially reduces the resolution in the Highest momentum area ($> 520\,\mathrm{keV}$), but according to equation A.3 this does not affect the results of Gauss fitting.
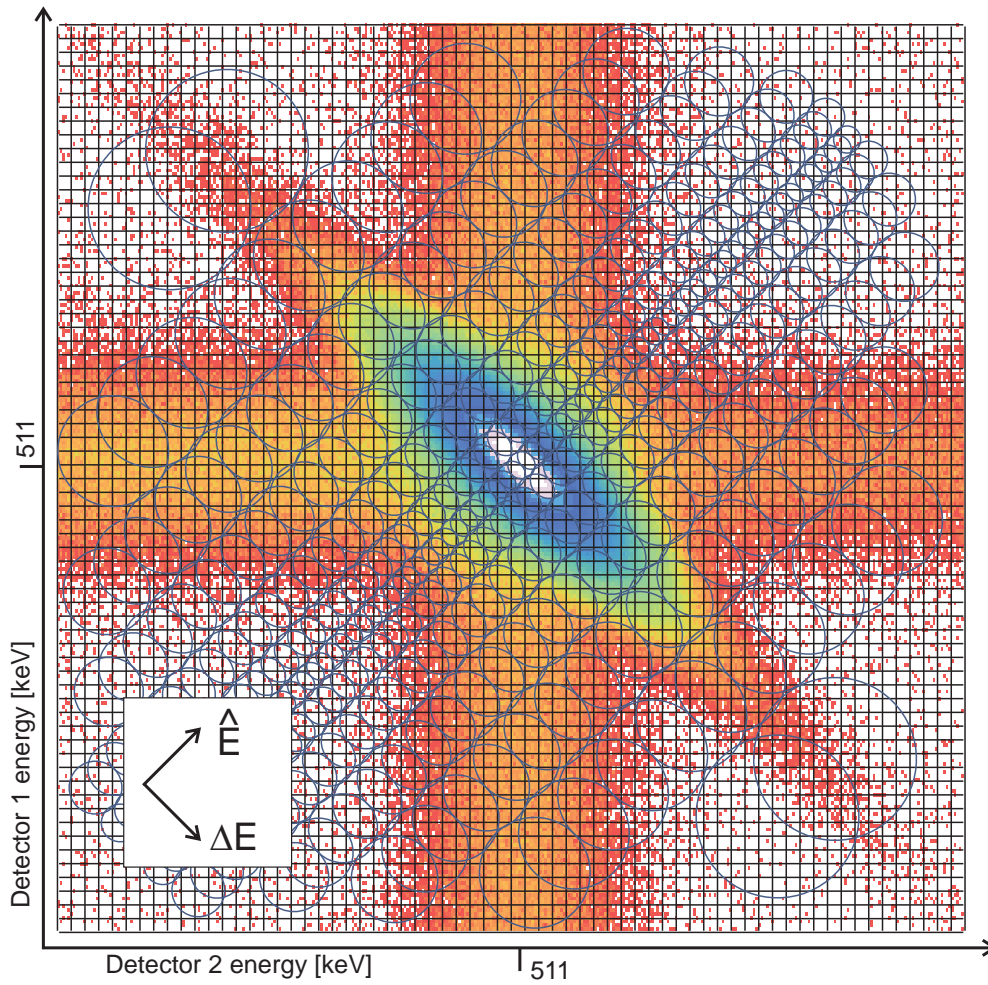
Figure A.1.: This plot schematically illustrates the optimized collection of events in the two dimensional spectrum with variable bin size. In the center area, where intrinsic disturbances are near to the Doppler broadening area and where count rates are high, the counts are evaluated with small collection circles. In the area of high Doppler shifts, where count rates are very low, many bins of the original spectrum are joined to improve the statistics. Collection circle sizes are for schematic illustration and not to scale.

A.4. Variable ROI steps

The processing of CDB spectra requires the assignment of discrete energies to each evaluated ROI. For evaluations with variable ROIs, a set of target energies was defined which turned out to be a good compromise between energy resolution in the low-momentum area and statistical accuracy in the high momentum area. Variable ROI evaluations in this work have been performed with the following target energy set:

n	$E_D(n)$	$w_{ROI}(n)$	n	$E_D(n)$	$w_{ROI}(n)$
1	511.00	0.10	**21**	514.44	0.42
2	511.10	0.10	**22**	514.86	0.47
3	511.20	0.10	**23**	515.33	0.53
4	511.30	0.10	**24**	515.86	0.59
5	511.40	0.10	**25**	516.45	0.65
6	511.50	0.11	**26**	517.10	0.73
7	511.61	0.11	**27**	517.83	0.80
8	511.72	0.11	**28**	518.63	0.89
9	511.83	0.12	**29**	519.52	0.98
10	511.95	0.13	**30**	520.49	1.08
11	512.08	0.14	**31**	521.57	1.18
12	512.22	0.15	**32**	522.75	1.29
13	512.37	0.17	**33**	524.04	1.41
14	512.54	0.19	**34**	525.45	1.54
15	512.73	0.21	**35**	526.99	1.67
16	512.94	0.24	**36**	528.66	1.82
17	513.18	0.26	**37**	530.48	1.97
18	513.44	0.30	**38**	532.44	2.13
19	513.74	0.33	**39**	534.57	2.29
20	514.07	0.37			

Table A.1.: The energy steps for a typical CDBS evaluation with variable ROI width.

B. Appendix - User manual

B.1. Short instructions for CDB control software
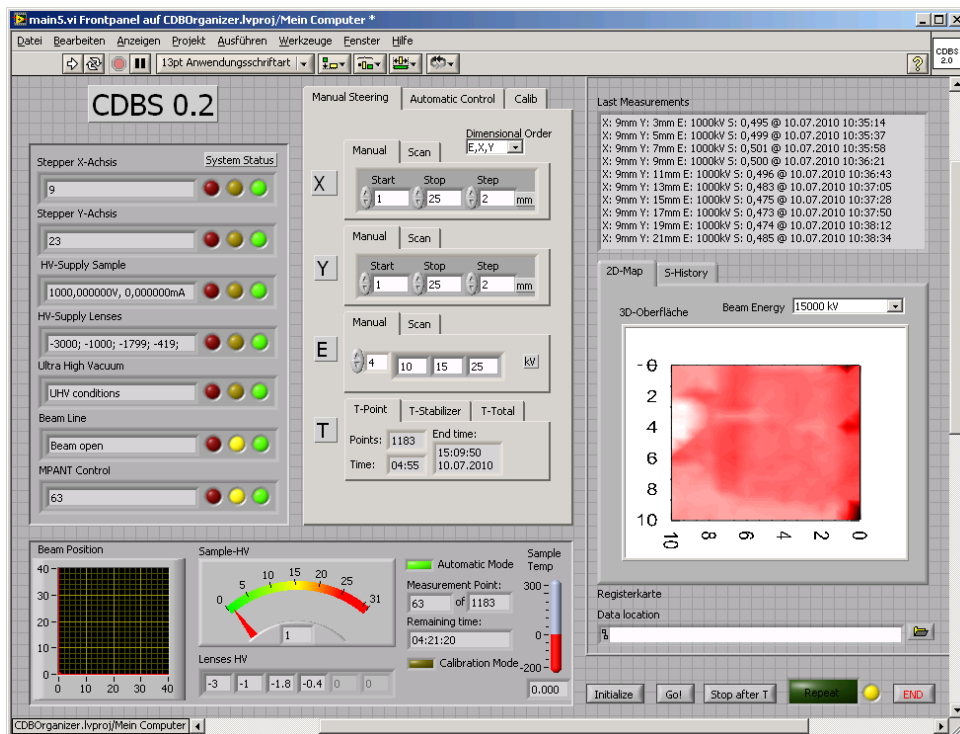
Figure B.1.: The CDB control software main screen

The (coincident) Doppler broadening spectrometer at NEPOMUC is controlled by a Labview™control software. It uses multi threading to simultaneously communicate to all the connected devices. The main screen as shown in figure B.1 gives an instantaneous view over their status. The upper left section labeled "system status" signals the successful communication to the controlled devices. The following states are possible:

Signal	Red	Yellow	Green	Device Status	Action required
	Off	Off	Off	Device not initialized	press "initialize"
	Off	Off	Off	Device initializing	
	On	Off	Off	Device error, non recoverable	check or restart
	On	On	Off	Device error, automatic recovery	check hardware
	Off	On	On	Device in operation	
	Off	Off	On	Device ready	

After initialization, all signals have to be in the "Device ready" state. During measurements, the according devices will be "in operation".

In the middle control window, the main parameters of the measurement are defined. A set of X and Y coordinates defines the beam positions on the sample. Also a set of beam energies E is defined. The "dimensional order" determines the method, how the respective sets of coordinates are linked. E.g. in the "E,X,Y" setting the Y-position is varied with every new measurement point whereas the beam energy E is kept constant over the complete $X \times Y$ scan. Accordingly, in "X,Y,E" the beam energy is varied while the beam position is constant, which is of advantage when multiple samples are to be investigated one at a time. In the mask labeled "T" the measurement time can be entered in "T-total". "T-point" shows the number of measurement points defined by the upper coordinate and energy sets and the estimated time which is required for all the measurements.

The upper right window lists the ten most recent measurements with their position, beam energy and a preliminarily calculated S-parameter. If "NaN" is displayed instead of a valid S-parameter, the acquired spectra were not valid e.g. due to a to low number of recorded annihilation events.

The surface view on the right side gives a first, also preliminary, image of $X \times Y$ scans. It can be used to conveniently and reliably determine the samples' coordinates and to ensure their homogeneity. On the lower left side of the control screen the instrument status and the progress of the actual measurement is displayed.

A measurement batch is started by the "Go!" button and can be aborted by pressing "Stop after T".

Because the control software is part of the CDB spectrometer at NEPOMUC, each user of this program will be comprehensively briefed in the operation of the spectrometers hard- and software.

B.2. User manual for CDB Organizer

The evaluation of the acquired CDB spectra can be done independently by the instruments user with the provided program package "CDB Organizer". It contains a database function

for organization and storage of the raw data files as well as the new data evaluation algorithm as described in section 3.3.

The CDB Organizer is available as a Microsoft Windows™installer package which contains the necessary runtime libraries. It adapts to different regional settings, but the decimal separator may not be changed after installation.

After loading, but before starting with the right arrow which is highlighted in the following screenshot, the paths to the database directories have to be specified. After first installation of the program, these paths may be empty.
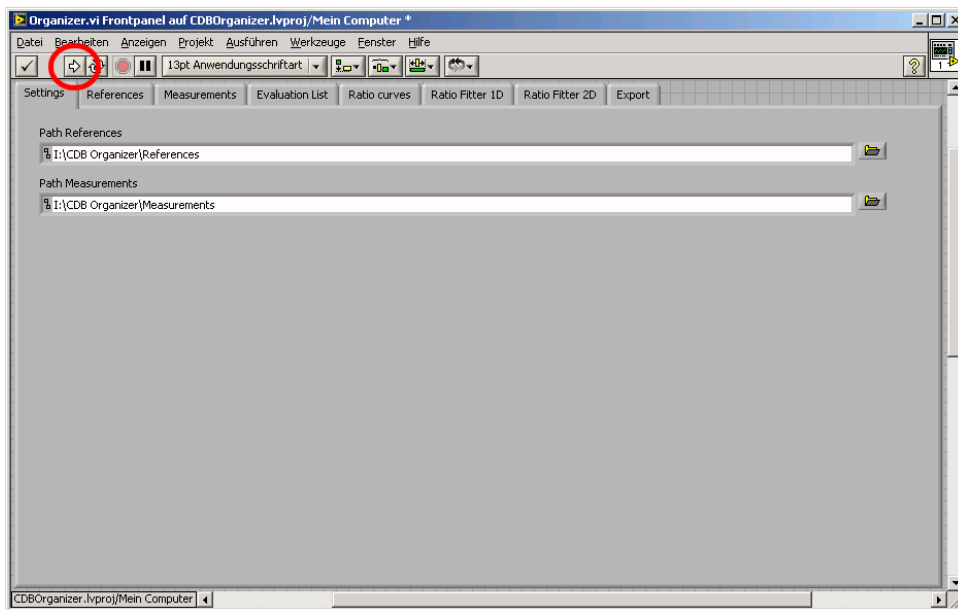
In the "References" and "Measurements" window the content of the previously chosen folders is shown. If the measurement was already previously evaluated, the evaluation values of this previous processing is displayed. By pressing the "Add" button highlighted in the following screenshot, a new measurement is integrated into the database. For this process, the data file from the acquisition system, a calibration file, a measurement name and a description have to be entered.
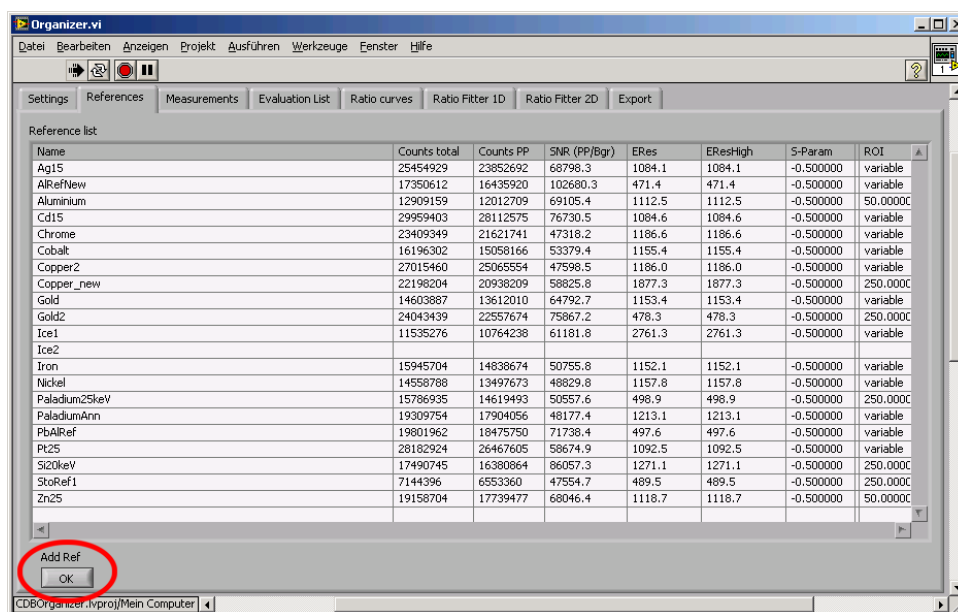
After integration of new files, all measurements and references which are of interest for the evaluation have to be highlighted in both of their windows. Multiple selection is possible by usage of the "ctrl" and "shift" key.

The selected datasets appear in the following "Evaluation List" window. The target energies of the evaluation can be defined in two ways: Either in the highlighted "ROI / STEP" box a fix step width is entered or the variable binning is chosen by entering zero. When variable binning is used, the target energies according to section 3.3.4 are to be defined in a file "Bins".

Pressing "Recalculate" starts the processing of the raw spectra. Depending on CPU speed and the bin setting, one spectrum can take up to several minutes of processing time.
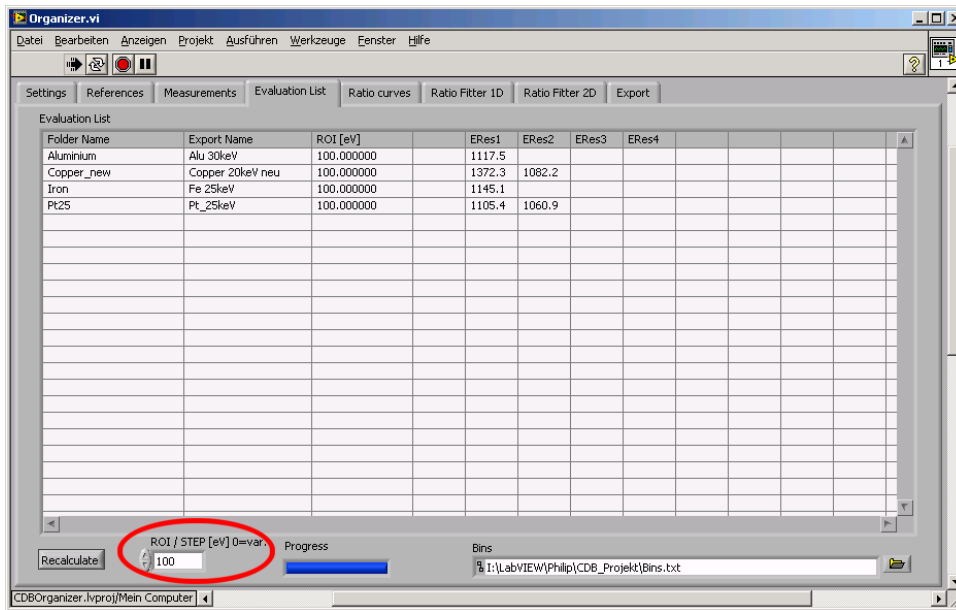
In the next window "Ratio curves" the chosen datasets are displayed as ratio curves as described in section 3.3.5. For correct calculation of the ratio curves an equivalent energy binning is necessary for all displayed measurements. The accordance of the active datasets is verified by the "Valid projections" indicator. The "Reference" selector defines the measurement which is normalized.
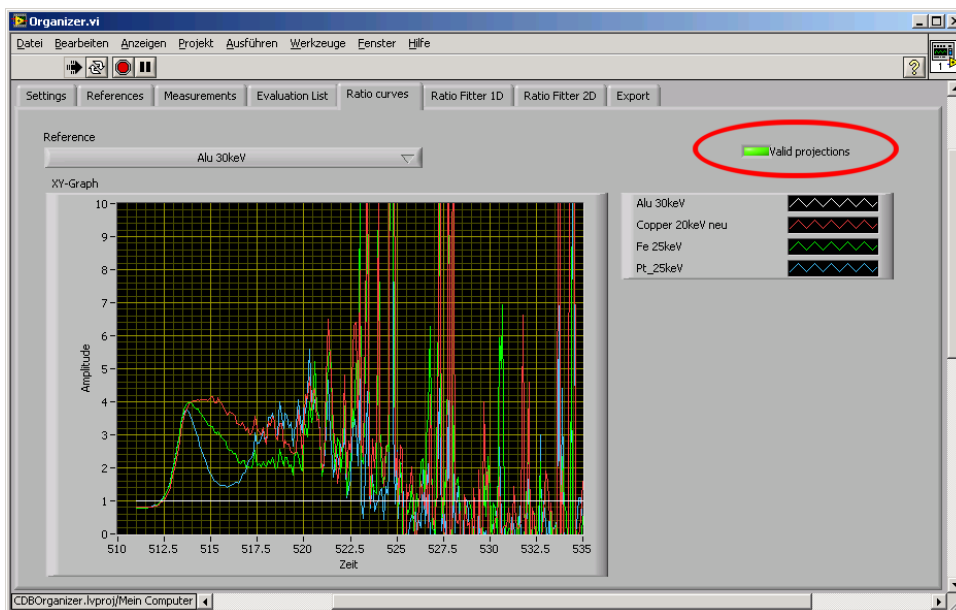
In the most applications, the ratio curves are the main result of the CDB spectroscopy. They can be exported in the "Export" window after specifying a filename and pressing the highlighted "Save Results" button.
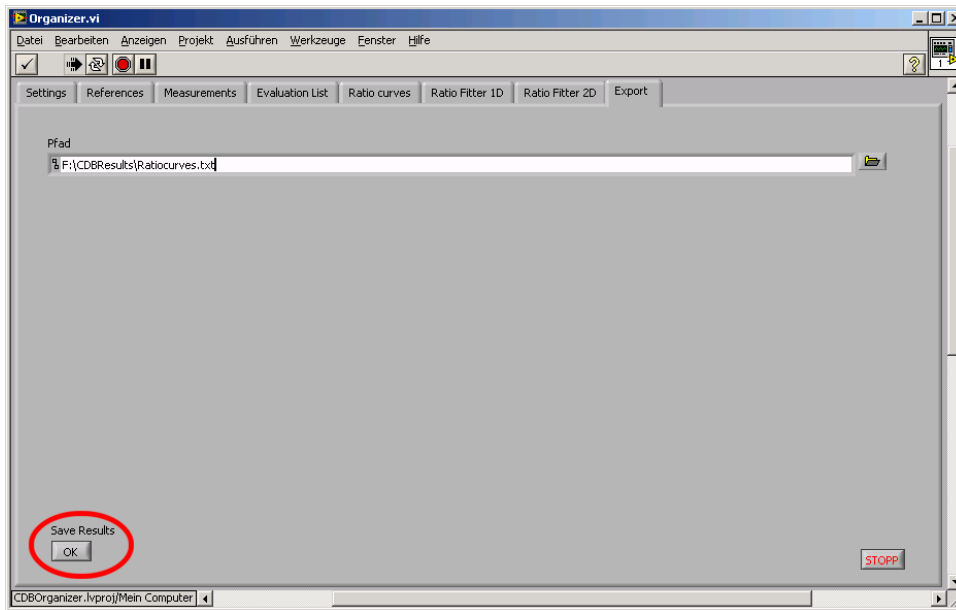
For further evaluation a ratio fitting procedure as described in section 3.3.6 can also be applied. For this purpose two references ("Reference A" and "Reference B") have to be defined. Then an energy range from "Start E" to "Stop E" is to be entered and the optimal linear combination of both references is fitted to all selected measurements. The fitting result is exported by pressing "Export Fits".
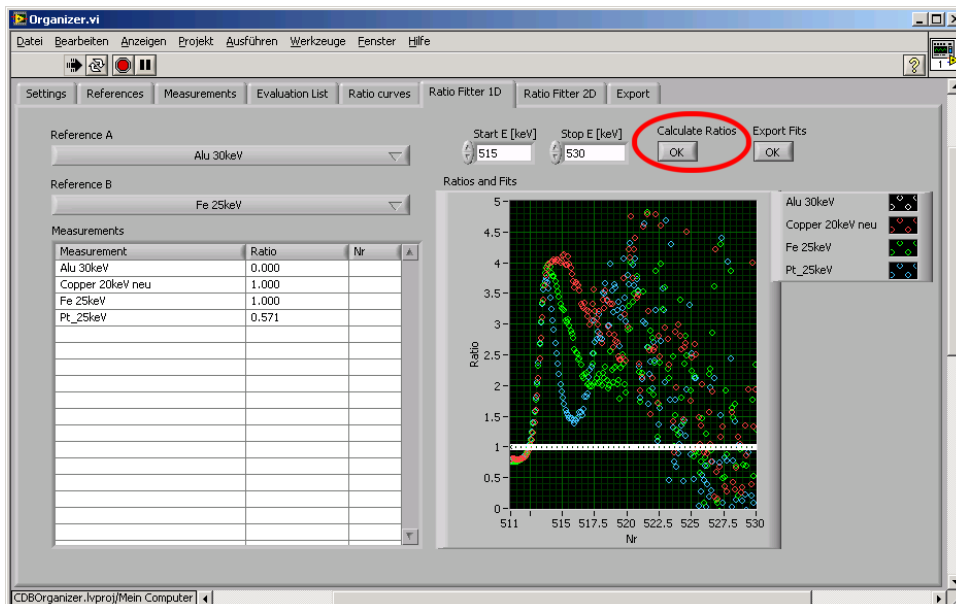
B.2.1. Database file structure

The main data evaluation software "CDBOrganizer" uses a standardized data structure for storage of measured spectra and processed projections. This enables an automatized and uniform processing of data from various timespans.

For the organization, a file and folder structure is used. The software user can choose two main folders for the storage of reference and measurement files. In these folders, the software creates subfolders with the samples name and with the content of table B.1.

File	Description
spectrum.mpa	The 2D-spectral data in the FAST .mpa format
calibration.cal	The energy calibration of this dataset
description.txt	A short description of this measurement, shown in the ratio curve result
projection.txt	The processed and projected, one-dimensional CDB spectrum
values.txt	Additional parameters gathered by the projection algorithm

Table B.1.: The file structure of the CDB Organizer

Bibliography

[1] R. N. West. Positron studies of condensed matter. *Adv. Phys.*, 22(3):263–383, 1973.

[2] S. Berko and J. C. Erskine. Angular distribution of annihilation radiation from plastically deformed aluminum. *Phys. Rev. Lett.*, 19(6):307–309, Aug 1967.

[3] G. Lang, S. DeBenedetti, and R. Smoluchowski. Measurement of electron momentum by positron annihilation. *Phys. Rev.*, 99(2):596–598, Jul 1955.

[4] K. G. Lynn, J. E. Dickman, W. L. Brown, M. F. Robbins, and E. Bonderup. Vacancies studied by positron annihilation with high-momentum core electrons. *Phys. Rev. B*, 20:3566–3572, 1979.

[5] P. Asoka-Kumar, M. Alatalo, V. J. Ghosh, A. C. Kruseman, B. Nielsen, and K. G. Lynn. Increased elemental specificity of positron annihilation spectra. *Phys. Rev. Lett.*, 77(10):2097–2100, Sep 1996.

[6] S. Szpala, P. Asoka-Kumar, B. Nielsen, J. P. Peng, S. Hayakawa, K. G. Lynn, and H.-J. Gossmann. Defect identification using the core-electron contribution in doppler-broadening spectroscopy of positron-annihilation radiation. *Phys. Rev. B*, 54(7):4722–4731, Aug 1996.

[7] P. E. Mijnarends, A. C. Kruseman, A. van Veen, H. Schut, and A. Bansil. Two-detector doppler broadening study of enhancement in al. *J. Phys.: Condens. Matter*, 10:10383–10390, 1998.

[8] M. Kostrzewa A. Baranowski, J. Beliczynski and M. Szuszkiewicz. A two-detector spectrometer for measurements of doppler broadened positron annihilation spectra. *Nucl. Instr. Meth. A*, 526:420–431, 2004.

[9] C. Hugenschmidt, P. Pikart, M. Stadlbauer, and K. Schreckenbach. High elemental selectivity to Sn submonolayers embedded in Al using positron annihilation spectroscopy. *Phys. Rev. B*, 77(9):092105, 2008.

[10] Y. Nagai, M. Hasegawa, Z. Tang, A. Hempel, K. Yubuta, T. Shimamura, Y. Kawazoe, A. Kawai, and F. Kano. Positron confinement in ultrafine embedded particles: Quantum-dot-like state in an Fe-Cu alloy. *Phys. Rev. B*, 61:6574, 2000.

[11] Y. Nagai, Z. Tang, M. Hassegawa, T. Kanai, and M. Saneyasu. Irradiation-induced Cu aggregations in Fe: An origin of embrittlement of reactor pressure vessel steels. *Phys. Rev. B*, 63(13):134110, Mar 2001.

[12] Y. Nagai, T. Toyama, Z. Tang, M. Hasegawa, S. Yanagita, T. Okhubo, and K. Hono. Embedded ultrafine clusters investigated by coincidence Doppler broadening spectroscopy. *Mat. Sci. For.*, 445-446:11, 2004.

[13] Philip Pikart, Christoph Hugenschmidt, Michael Horisberger, Yoshitaka Matsukawa, Masahiko Hatakeyama, Takeshi Toyama, and Yasuyoshi Nagai. Positron annihilation in cr, cu, and au layers embedded in al and quantum confinement of positrons in au clusters. *Phys. Rev. B*, 84:014106, Jul 2011.

[14] P.A.M. Dirac. A theory of electrons and protons. *Proc. Roy. Soc. A*, 126:360–365, 1930.

[15] Carl D. Anderson. The positive electron. *Phys. Rev.*, 43(6):491–494, Mar 1933.

[16] C. D. Anderson. The apparent existence of easily deflectable positives. *Science*, 76:238, 1932.

[17] Carl D. Anderson. Energies of cosmic-ray particles. *Phys. Rev.*, 41(4):405–421, Aug 1932.

[18] Thomas Beier, Hartmut Häffner, Nikolaus Hermanspahn, Savely G. Karshenboim, H.-Jürgen Kluge, Wolfgang Quint, Stefan Stahl, José Verdú, and Günther Werth. New determination of the electron's mass. *Phys. Rev. Lett.*, 88(1):011603, Dec 2001.

[19] H. Pilkuhn. *Properties and Production Spectra of Elementary Particles*, volume 6 of *Landolt-Barnstein - Group I Elementary Particles, Nuclei and Atoms*. Springer-Verlag, 1972.

[20] E. Bellotti, M. Corti, E. Fiorini, C. Liguori, A. Pullia, A. Sarracino, P. Sverzellati, and L. Zanotti. A new experimental limit on electron stability. *Physics Letters B*, 124:435, 1983.

[21] R. A. Ferrell. Theory of positron annihilation in solids. *Rev. Mod. Phys.*, 28(3):308, Jul 1956.

[22] Leon Madansky and Franco Rasetti. An attempt to detect thermal energy positrons. *Phys. Rev.*, 79(2):397, Jul 1950.

[23] John M. J. Madey. Evidence for the emission of slow positrons from polyethylene. *Phys. Rev. Lett.*, 22(15):784–787, Apr 1969.

[24] D. G. Costello, D. E. Groce, D. F. Herring, and J. W. McGowan. Evidence for the negative work function associated with positrons in gold. *Phys. Rev. B*, 5(4):1433–1436, Feb 1972.

[25] B. Y. Tong. Negative work function of thermal positrons in metals. *Phys. Rev. B*, 5(4):1436–1439, Feb 1972.

[26] Allen P. Mills, Jr. Efficient generation of low-energy positrons. *Appl. Phys. Lett.*, 35(5):427–429, 1979.

[27] M. J. Puska, P. Lanki, and R. M. Nieminen. Positron affinities for elemental metals. *J. Phys.: Condens. Matter*, 1:6081–6094, 1989.

[28] M.J. Puska and R.M. Nieminen. Theory of positrons in solids and on solid surfaces. *Rev. Mod. Phys.*, 66(3):841–897, Jul 1994.

[29] Thomas M. Hall, A. N. Goland, and C. L. Snead. Applications of positron-lifetime measurements to the study of defects in metals. *Phys. Rev. B*, 10(8):3062–3074, Oct 1974.

[30] E. Soininen, H. Huomo, P. A. Huttunen, J. Mäkinen, A. Vehanen, and P. Hautojärvi. Temperature dependence of positron diffusion in cubic metals. *Phys. Rev. B*, 41(10):6227–6233, Apr 1990.

[31] A. P. Mills, P. M. Platzman, and B. L. Brown. Slow-positron emission from metal surfaces. *Phys. Rev. Lett.*, 41(15):1076–1079, Oct 1978.

[32] G R Brandes, K F Canter, T N Horsky, P H Lippel, and A P Mills. Production and applications of positron microbeams. *J. Phys.: Condens. Matter*, 1(SA):SA135–SA143, 1989.

[33] C. Piochacz, G. Kögel, W. Egger, C. Hugenschmidt, J. Mayer, K. Schreckenbach, P. Sperr, M. Stadlbauer, and G. Dollinger. A positron remoderator for the high intensity positron source NEPOMUC. *Appl. Surf. Sci.*, 255(1):98 – 100, 2008.

[34] A. van Veen, H. Schut, J. de Roode, F. Labohm, C.V. Falub, S.W.H. Eijt, and P.E. Mijnarends. Performance of an intense nuclear-reactor based positron beam. *Mat. Sci. For.*, 363-365:415–419, 2001.

[35] C. Hugenschmidt, G. KÃűgel, R. Repper, K. Schreckenbach, P. Sperr, and W. TriftshÃďuser. First platinum moderated positron beam based on neutron capture. *Nucl. Instr. Meth. B*, 198:220–229, 2002.

[36] R. N. West, J. Mayers, and P. A. Walters. A high-efficiency two-dimensional angular correlation spectrometer for positron studies. *J. Phys. E: Sci. Instrum.*, 14:478–488, 1981.

[37] K. O. Jensen and A. Weiss. Theoretical study of the application of positron-induced Auger-electron spectroscopy. *Phys. Rev. B*, 41(7):3928–3936, Mar 1990.

[38] Martin Stadlbauer. *Investigation of the chemical vicinity of defects in Mg and AZ31 with positron coincident Doppler broadening spectroscopy*. PhD thesis, Lehrstuhl für Experimentalphysik E21, Technische Universität München, 2008.

[39] H. Stöcker. *Taschenbuch der Physik*. Harri Deutsch, 1998.

[40] Masanori Fujinami, Tsuguo Sawada, and Takashi Akahane. Coincidence doppler broadening positron annihilation spectroscopy in defects of silicon and iron. *Radiation Physics and Chemistry*, 68(3-4):631 – 634, 2003. Proceedings of the 7th International Conference on Positron and Positronium Chemistry.

[41] M. Stadlbauer, C. Hugenschmidt, K. Schreckenbach, and P. Böni. Investigation of the chemical vicinity of crystal defects in ion-irradiated Mg and a Mg-Al-Zn alloy with coincident Doppler broadening spectroscopy. *Phys. Rev. B*, 76(17):174104, 2007.

[42] Markus Reiner. Depth resolved doppler broadening spectroscopy of thin metallic films with a monoenergetic positron beam. Master's thesis, Technische Universität München, 2011.

[43] St. Mohorovicic. Möglichkeit neuer elemente und ihre bedeutung für die astrophysik. *Astronomische Nachrichten*, 253(4):93–108, 1934.

[44] Werner Brandt and Robert Paulin. Positronium diffusion in solids. *Phys. Rev. Lett.*, 21(4):193–195, Jul 1968.

[45] Hubert Ceeh, Christoph Hugenschmidt, Klaus Schreckenbach, Stefan A. Gärtner, Peter G. Thirolf, Frank Fleischer, and Dirk Schwalm. Precision measurement of the decay rate of the negative positronium ion ps-. *Phys. Rev. A*, 84:062508, Dec 2011.

[46] Savely G. Karschenboim. Precision study of positronium: Testing bound state qed theory. *International Journal of Modern Physics A (IJMPA)*, 23:3879–3896, 2004.

[47] A. Badertscher, P. Crivelli, W. Fetscher, U. Gendotti, S. N. Gninenko, V. Postoev, A. Rubbia, V. Samoylenko, and D. Sillou. Improved limit on invisible decays of positronium. *Phys. Rev. D*, 75:032004, Feb 2007.

[48] Chunqing He, Toshiyuki Ohdaira, Nagayasu Oshima, Makoto Muramatsu, Atsushi Kinomura, Ryoichi Suzuki, Toshitaka Oka, and Yoshinori Kobayashi. Evidence for pore surface dependent positronium thermalization in mesoporous silica/hybrid silica films. *Phys. Rev. B*, 75:195404, May 2007.

[49] Allen P. Mills. Positronium formation at surfaces. *Phys. Rev. Lett.*, 41(26):1828–1831, Dec 1978.

[50] G. Triftshäuser, G. Kögel, W. Triftshäuser, M. Springer, B. Strasser, and K. Schreckenbach. A high intense reactor based positron source. *Appl. Surf. Sci.*, 116:45 – 48, 1997.

[51] C. Hugenschmidt, B. Straßer, and K. Schreckenbach. Investigation of positron work function and moderation efficiency of Ni, Ta, Pt and W(100). *Appl. Surf. Sci.*, 194(1-4):283 – 286, 2002.

[52] C. Hugenschmidt, B. Löwe, J. Mayer, C. Piochacz, P. Pikart, R. Repper, M. Stadlbauer, and K. Schreckenbach. Unprecedented intensity of a low-energy positron beam. *Nucl. Instr. Meth. A*, 593(3):616–618, 2008.

[53] C. Hugenschmidt, K. Schreckenbach, M. Stadlbauer, and B. Straßer. Low-energy positrons of high intensity at the new positron beam facility NEPOMUC. *Nucl. Instr. Meth. A*, 554:384–391, 2005.

[54] L. D. Landau and E. M. Lifschitz. *Klassische Feldtheorie*, chapter III, page 64. Akademie-Verlag Berlin, 1973.

[55] G. F. Knoll. *Radiation Detection and Measurement.* John Wiley & Sons, Inc., 2000.

[56] M. Haaks, T. E. M. Staab, and K. Maier. Analyzing the high-momentum part of positron annihilation doppler spectra with a single germanium detector. *Nucl. Instr. Meth. A*, 569:829, 2006.

[57] Jack R. MacDonald, K.G. Lynn, R.A. Boie, and M.F. Robbins. A two-dimensional doppler broadened technique in positron annihilation. *Nuclear Instruments and Methods*, 153(1):189 – 194, 1978.

[58] I. Makkonen, M. Hakala, and M.J. Puska. First principles calculation of positron states and annihilation at defects in semiconductors. *Physica B: Condensed Matter, Proceedings of the 23rd International Conference on Defects in Simconductors*, 376-377:971–974, 2006.

[59] A. Calloni, A. Dupasquier, R. Ferragut, P. Folegati, M. M. Iglesias, I. Makkonen, and M. J. Puska. Positron localization effects on the doppler broadening of the annihilation line: Aluminum as a case study. *Phys. Rev. B*, 72(5):054112, Aug 2005.

[60] W. Wagner, A. Saul, and A. Pruss. International equations for the pressure along the melting and along the sublimation curve of ordinary water substance. *Journal of Physical and Chemical Reference Data*, 23:515–527, May 1994.

[61] C. Hugenschmidt, J. Mayer, and M. Stadlbauer. Investigation of the near surface region of chemically treated and Al-coated PMMA by Doppler-broadening spectroscopy. *Radiat. Phys. Chem.*, 76(2):217 – 219, 2007.

[62] P. Pikart, C. Hugenschmidt, J. Mayer, M. Stadlbauer, and K. Schreckenbach. Depth resolved Doppler broadening measurement of layered Al-Sn samples. *Appl. Surf. Sci.*, 255(1):245 – 247, 2008.

[63] Philip Pikart. Elementspezifische Analyse von Al-Sn-Al Schichtsystemen mit der Positronenannihilationsspektroskopie. Diploma thesis, Lehrstuhl für Experimentalphysik E21, Technische Universität München, 2007.

[64] P. Coleman. *Positron beams and their applications.* World Scientific, 2000.

[65] A. Vehanen, K. Saarinen, P. Hautojärvi, and H. Huomo. Profiling multilayer structures with monoenergetic positrons. *Phys. Rev. B*, 35(10):4606–4610, Apr 1987.

[66] H. Garbacz, P. Wiecioski, B. Adamczyk-Ciealak, J. Mizera, and K.J. Kurzydowski. Studies of aluminium coatings deposited by vacuum evaporation and magnetron sputtering. *Journal of Microscopy*, 237(3 PG: 475-480):475–480, 2010.

[67] Z Tang, T Toyama, Y Nagai, K Inoue, Z Q Zhu, and M Hasegawa. Size-dependent momentum smearing effect of positron annihilation radiation in embedded nano cu clusters. *Journal of Physics: Condensed Matter*, 20(44):445203, 2008.

[68] H. Mehrer. *Diffusion in Solids.* Springer, Series in Solid-State Sciences, Bd. 155, 2007.

[69] H. Okamoto. Al-au (aluminum-gold). *Journal of Phase Equilibria and Diffusion*, 26:391–393, 2005. 10.1007/s11669-005-0098-0.

[70] P. Pikart, C. Hugenschmidt, and K. Schreckenbach. Doppler-broadening (DB) measurement of ionic liquids using a monoenergetic positron beam. *phys. stat. sol. (c)*, 6(11):2487–2489, 2009.

[71] Gennady J. Kabo, Andrey V. Blokhin, Yauheni U. Paulechka, Andrey G. Kabo, Marina P. Shymanovich, and Joseph W. Magee. Thermodynamic properties of 1-butyl-3-methylimidazolium hexafluorophosphate in the condensed state. *Journal of Chemical & Engineering Data*, 49(3):453–461, 2004.

[72] Yoonnam Jeon, David Vaknin, Wei Bu, Jaeho Sung, Yukio Ouchi, Woongmo Sung, and Doseok Kim. Surface nanocrystallization of an ionic liquid. *Phys. Rev. Lett.*, 108:055502, Jan 2012.

[73] Alessandro Triolo, Olga Russina, Barbara Fazio, Roberto Triolo, and Emanuela Di Cola. Morphology of 1-alkyl-3-methylimidazolium hexafluorophosphate room temperature ionic liquids. *Chemical Physics Letters*, 457(4-6):362 – 365, 2008.

[74] Takatsugu Endo, Tatsuya Kato, Ken-ichi Tozaki, and Keiko Nishikawa. Phase behaviors of room temperature ionic liquid linked with cation conformational changes: 1-butyl-3-methylimidazolium hexafluorophosphate. *The Journal of Physical Chemistry B*, 114(1):407–411, 2010. PMID: 19950961.

[75] R.K.W. Marceau, G. Sha, R. Ferragut, A. Dupasquier, and S.P. Ringer. Solute clustering in al-cu-mg alloys during the early stages of elevated temperature ageing. *Acta Materialia*, 58(15):4923 – 4939, 2010.

[76] Bernd Oberdorfer, Eva-Maria Steyskal, Wolfgang Sprengel, Werner Puff, Philip Pikart, Christoph Hugenschmidt, Michael Zehetbauer, Reinhard Pippan, and Roland Würschum. *In Situ* probing of fast defect annealing in cu and ni with a high-intensity positron beam. *Phys. Rev. Lett.*, 105:146101, Sep 2010.

[77] D. J. Keeble, R. A. Mackie, W. Egger, B. Löwe, P. Pikart, C. Hugenschmidt, and T. J. Jackson. Identification of vacancy defects in a thin film perovskite oxide. *Phys. Rev. B*, 81(6):064102, Feb 2010.

[78] Ralph Gilles, Michael Hofmann, Francis Johnson, Yan Gao, Debashis Mukherji, Christoph Hugenschmidt, and Philip Pikart. Analysis of antiphase domain growth in ternary feco alloys after different cooling rates and annealing treatments using neutron diffraction and positron annihilation. *Journal of Alloys and Compounds*, 509(2):195 – 199, 2011.

List of publications

[1] PIKART, P. ; HUGENSCHMIDT, C. ; HORISBERGER, M. ; MATSUKAWA, Y. ; HATAKEYAMA, M. ; TOYAMA, T. ; NAGAI, Y.: Positron annihilation in Cr, Cu, and Au layers embedded in Al and quantum confinement of positrons in Au clusters. In: *Physical Review B: Condensed Matter and Materials Physics* 84 (2011), Nr. 1, S. 014106. `http://dx.doi.org/10.1103/PhysRevB.84.014106`. – DOI 10.1103/PhysRevB.84.014106

[2] PIKART, P. ; HUGENSCHMIDT, C. ; SCHRECKENBACH, K.: Doppler-broadening (DB) measurement of ionic liquids using a monoenergeticpositron beam. In: *phys. stat. sol. (c)* 6 (2009), Nr. 11, 2487-2489. `http://dx.doi.org/10.1002/pssc.200982085`. – DOI 10.1002/pssc.200982085

[3] PIKART, P. ; HUGENSCHMIDT, C. ; MAYER, J. ; STADLBAUER, M. ; SCHRECKENBACH, K.: Depth resolved Doppler broadening measurement of layered Al-Sn samples. In: *Appl. Surf. Sci.* 255 (2008), Nr. 1, 245 - 247. `http://dx.doi.org/10.1016/j.apsusc.2008.05.305`. – DOI 10.1016/j.apsusc.2008.05.305. – ISSN 0169–4332

[4] SCHRECKENBACH, K. ; HUGENSCHMIDT, C. ; LÖWE, B. ; MAIER, J. ; PIKART, P. ; PIOCHACZ, C. ; STADLBAUER, M.: Performance of the (n,γ)-Based Positron Beam Facility NEPOMUC. In: *AIP Conference Proceedings* 1090 (2009), Nr. 1, 549-553. `http://dx.doi.org/10.1063/1.3087083`. – DOI 10.1063/1.3087083

[5] HUGENSCHMIDT, C. ; DOLLINGER, G. ; EGGER, W. ; KÖGEL, G. ; LÖWE, B. ; MAYER, J. ; PIKART, P. ; PIOCHACZ, C. ; REPPER, R. ; SCHRECKENBACH, K. ; SPERR, P. ; STADLBAUER, M.: Surface and bulk investigations at the high intensity positron beamfacility NEPOMUC. In: *Appl. Surf. Sci.* 255 (2008), Nr. 1, 29 - 32. `http://dx.doi.org/10.1016/j.apsusc.2008.05.304`. – DOI 10.1016/j.apsusc.2008.05.304. – ISSN 0169–4332

[6] HUGENSCHMIDT, C. ; LÖWE, B. ; MAYER, J. ; PIOCHACZ, C. ; PIKART, P. ; REPPER, R. ; STADLBAUER, M. ; SCHRECKENBACH, K.: Unprecedented intensity of a low-energy positron beam. In: *Nucl. Instr. Meth. A* 593 (2008), Nr. 3, S. 616–618. `http://dx.doi.org/10.1016/j.nima.2008.05.038`. – DOI 10.1016/j.nima.2008.05.038

[7] HUGENSCHMIDT, C. ; PIKART, P. ; SCHRECKENBACH, K.: Coincident Doppler-broadening spectroscopy of Si, amorphous SiO2,and alpha-quartz using mono-energetic positrons. In: *phys. stat. sol. (c)* 6 (2009), Nr. 11, 2459-2461. `http://dx.doi.org/10.1002/pssc.200982100`. – DOI 10.1002/pssc.200982100

[8] HUGENSCHMIDT, C. ; PIKART, P. ; STADLBAUER, M. ; SCHRECKENBACH, K.: High elemental selectivity to Sn submonolayers embedded in Al usingpositron annihilation spectroscopy. In: *Phys. Rev. B* 77 (2008), Nr. 9, 092105. `http://dx.doi.org/10.1103/PhysRevB.77.092105`. – DOI 10.1103/PhysRevB.77.092105

[9] BRUSA, R.S. ; MARIAZZI, S. ; RAVELLI, L. ; MAZZOLDI, P. ; MATTEI, G. ; EGGER, W. ; HUGENSCHMIDT, C. ; LÖWE, B. ; PIKART, P. ; MACCHI, C. ; SOMOZA, A.: Study of defects in implanted silica glass by depth profiling Positron Annihilation Spectroscopy. In: *Nuclear Instruments & Methods in Physics Research, Section B: Beam Interactions with Materials and Atoms* 268 (2010), 10, Nr. 19, S. 3186–3190. `http://dx.doi.org/10.1016/j.nimb.2010.05.084`. – DOI 10.1016/j.nimb.2010.05.084

[10] GILLES, R. ; HOFMANN, M. ; JOHNSON, F. ; GAO, Y. ; MUKHERJI, D. ; HUGENSCHMIDT, C. ; PIKART, P.: Analysis of antiphase domain growth in ternary FeCo alloys after different cooling rates and annealing treatments using neutron diffraction and positron annihilation. In: *Journal of Alloys and Compounds* 509 (2011), Nr. 2, 195-199. `http://dx.doi.org/10.1016/j.jallcom.2010.09.075`. – DOI 10.1016/j.jallcom.2010.09.075. – ISSN 0925–8388

[11] HAIN, K. ; HUGENSCHMIDT, C. ; PIKART, P. ; BÖNI, P.: Spatially resolved positron annihilation spectroscopy on frictionstir weld induced defects. In: *Science and Technology of Advanced Materials* 11 (2010), Nr. 2, 025001. `http://dx.doi.org/10.1088/1468-6996/11/2/025001`. – DOI 10.1088/1468–6996/11/2/025001

[12] HENGSTLER-EGER, R.M. ; BALDO, P. ; BECK, L. ; DORNER, J. ; ERTL, K. ; HOFFMANN, P.B. ; HUGENSCHMIDT, C. ; KIRK, M.A. ; PETRY, W. ; PIKART, P. ; REMPEL, A.: Heavy ion irradiation induced dislocation loops in AREVA's M5 alloy. In: *Journal of Nuclear Materials* (2012)

[13] KEEBLE, D.J. ; MACKIE, R.A. ; EGGER, W. ; LÖWE, B. ; PIKART, P. ; HUGENSCHMIDT, C. ; JACKSON, T.J.: Identification of vacancy defects in a thin film perovskite oxide. In: *Physical Review B: Condensed Matter and Materials Physics* 81 (2010), 2, Nr. 6, S. 064102. `http://dx.doi.org/10.1103/PhysRevB.81.064102`. – DOI 10.1103/PhysRevB.81.064102

[14] OBERDORFER, B. ; STEYSKAL, E.-M. ; SPRENGEL, W. ; PUFF, W. ; PIKART, P. ; HUGENSCHMIDT, C. ; ZEHETBAUER, M. ; PIPPAN, R. ; WÜRSCHUM, R.: In Situ Probing of Fast Defect Annealing in Cu and Ni with a High-IntensityPositron Beam. In: *Physical Review Letters* 105 (2010), Nr. 14, S. 146101. `http://dx.doi.org/10.1103/PhysRevLett.105.146101`. – DOI 10.1103/PhysRevLett.105.146101

Acknowledgments